Distribution Agreement

In presenting this thesis or dissertation as a partial fulfillment of the requirements for an advanced degree from Emory University, I hereby grant to Emory University and its agents the non-exclusive license to archive, make accessible, and display my thesis or dissertation in whole or in part in all forms of media, now or hereafter known, including display on the world wide web. I understand that I may select some access restrictions as part of the online submission of this thesis or dissertation. I retain all ownership rights to the copyright of the thesis or dissertation. I also retain the right to use in future works (such as articles or books) all or part of this thesis or dissertation.

Signature:

_____ _____

Steven J. Ryan Date

Developmental Regulation of Membrane Potential Oscillations in the Basolateral Amygdala: Modulation by β-Adrenergic Receptor Activation

By

Steven J. Ryan
Doctor of Philosophy

Graduate Division of Biological and Biomedical Sciences
Neuroscience

_____
Donald G. Rainnie, Ph.D.
Advisor

_____
Shannon L. Gourley, Ph.D.
Committee Member

_____
Andrew Jenkins, Ph.D.
Committee Member

_____
Kerry J. Ressler, Ph.D.
Committee Member

_____
Peter Wenner, Ph.D.
Committee Member

Accepted:

_____
Lisa A. Tedesco, Ph.D.
Dean of the James T. Laney School of Graduate Studies

_____
Date

Developmental Regulation of Membrane Potential Oscillations in the Basolateral Amygdala: Modulation by β-Adrenergic Receptor Activation

By

Steven J. Ryan
B.S., Georgia Institute of Technology
Biomedical Engineering, 2007

Advisor: Donald G. Rainnie, Ph.D.

An abstract of
A dissertation submitted to the Faculty of the
James T. Laney School of Graduate Studies of Emory University
in partial fulfillment of the requirements for the degree of
Doctor of Philosophy

Graduate Division of Biological and Biomedical Sciences
Neuroscience

2015

Abstract

Developmental Regulation of Membrane Potential Oscillations in the Basolateral Amygdala: Modulation by β-Adrenergic Receptor Activation

By: Steven J. Ryan

The basolateral nucleus of the amygdala (BLA) is a brain region of fundamental importance in enabling emotional memory. A wealth of evidence also demonstrates the causative role that dysfunction of the BLA can play in many psychiatric disorders, which often emerge during juvenile and adolescent brain development. In order to effectively treat these disorders, interventions must be developed that are appropriate to the age of diagnosis. The existing literature demonstrates a large number of BLA-dependent behaviors mature during juvenile development, which suggests there must be massive concomitant changes to how the BLA processes information. Despite the apparent importance and dynamic nature of BLA development, however, almost nothing is known about the normative development of the juvenile BLA. In this dissertation, we begin to address this knowledge gap by performing an extensive characterization of the physiology and morphology of developing BLA principal neurons with the ultimate goal of identifying putative critical periods which may exhibit particular sensitivity to disruption or opportunity for intervention.

In adult rats, synchronized neural activity in the BLA and related regions is critical for emotional memory formation. Little was known, however, about the cellular mechanisms contributing to synchronization in the BLA, or if a similar process was utilized across development to regulate affective behavior. Toward this end, we first explore low-frequency membrane potential oscillations and synchronous synaptic activity in adult rats. We were able to evoke low-frequency MPOs in BLA principal neurons and provide evidence suggesting that these oscillations serve to synchronize the activity of large ensembles of neurons. We also show that these MPOs are subject to modulation by intracellular signaling cascade which is itself regulated by the activity of neuromodulators. These results motivated us to explore the development of this critical facet of BLA physiology. However, in order to effectively do so, we needed to characterize more fundamental aspects of the development of BLA principal neurons. Thus, we next characterized the intrinsic physiology and dendritic morphology of these neurons. These studies showed dramatic maturation of the BLA across the first postnatal month: neuronal input resistance drops by nearly 10-fold, intrinsic voltage-gated currents mature substantially, and aggregate dendritic length increases by nearly 4-fold. Many other dramatic changes unfold over this same period, which we discuss in detail below. Finally, catecholaminergic innervation of the BLA shows major changes over this same time period, and we further demonstrated a developmental progression in the ability of norepinephrine to enhance tuned, frequency-specific MPOs and to facilitate organized firing activity by synchronous synaptic activity. These studies will provide an important context for future work looking at the development of psychiatric disorders in the juvenile brain.

Developmental Regulation of Membrane Potential Oscillations in the Basolateral Amygdala: Modulation by β-Adrenergic Receptor Activation

By

Steven J. Ryan
B.S., Georgia Institute of Technology
Biomedical Engineering, 2007

Donald G. Rainnie, Ph.D.

A dissertation submitted to the Faculty of the
James T. Laney School of Graduate Studies of Emory University
in partial fulfillment of the requirements for the degree of
Doctor of Philosophy

Graduate Division of Biological and Biomedical Sciences
Neuroscience

2015

Acknowledgements

There are so many people in my life without whom this document, this body of work, would not have been possible. While I certainly can never name them all, or the unique ways in which they contributed, I'd like to take a moment to enumerate a few particularly influential individuals -

To my family and friends, for their unflinching support for going on thirty years; to my many mentors and teachers, but particularly Ned Granville and Phil Santangelo, without whose lessons in science, skepticism, and confidence I never would have made it this far; to every member of the Rainnie Lab over the years I worked here, including Teresa Madsen, Sarah Danels, Tom Hennessey, JiDong Guo, Joanna Dabrowska, Rimi Hazra, and ChenChen Li, for their hard work and patience through many years of training and experiments; to my thesis committee for their years of patience and guidance; to my advisor, Tig Rainnie, who refused to ever settle for anything less than my very best;
and, finally, to David Ehrlich, who has been a true partner on so many projects and adventures, and has always pushed me to be more creative, to think and write more clearly, and to choose my battles carefully.

To all of you, thank you for everything.

Table of Contents

List of Figures and Tables

Chapter 1

General Introduction

Psychiatric disorders are a large and rapidly growing public health concern in the modern age. Conservative models estimate the total cost to the United States in terms of direct healthcare costs and lost work exceeds $300 billion (Insel, 2008). Historically, these disorders have been treated as mostly afflicting the adult population, and early-onset disorders in juveniles were considered the rare exception to that rule. This view has been challenged by research conducted over the last 20 years which has made it clear that many psychiatric disorders diagnosed in adults are preceded by similar psychiatric conditions observable during adolescence (Pine 1998; Kim-Cohen 2003; Kessler et al., 2007a,b). Indeed, more than 30% of Americans will suffer from an anxiety disorder at some point in their life, and more than half of these conditions will begin before the age of 11 (Kessler et al., 2005). If psychiatric disorders are to be effectively treated, interventions must begin early in life, when the disorder manifests. Abundant research shows that postnatal brain development continues well into the late stages of adolescence (Paus, 2005; Cressman et al., 2010). Effective interventions cannot be developed, therefore, until we understand more fully the function and composition of the developing brain. Below I will briefly outline some of the existing literature which highlights important questions about the development of the basolateral amygdala, a limbic region crucially involved in the etiology of many psychiatric disorders, before describing in detail a series of studies aimed at addressing these questions.

The amygdala is an integrated, interconnected collection of cortically- and striatally-derived limbic nuclei which plays a critical role in affective processing (Davis et al., 2003; LeDoux, 2007; Olucha-Bordonau et al., 2014; Carlsen & Heimer, 1988; Swanson & Petrovich, 1998; Pape and Parè, 2010). The basolateral nucleus of the amygdala (BLA) is an important site of sensory input to the amygdala (McDonald 1998), and is particularly important in the learning of fearful associations (Campeau et al., 1992; Miserendino et al., 1990; Davis, 2000). Conditioned fear or aversion is

actually not expressed at birth, however; rat pups do not show aversion to a conditioned stimulus paired with an external noxious stimulus until postnatal day 10 (P10) (Haroutunian & Campbell, 1979; Thompson et al., 2008). Similarly, the amygdala is necessary for generating context-appropriate behavioral responses to innate threats (Blanchard & Takahashi, 1988; Takahashi et al., 2007), but neonatal rodents do not show fearful responses in the presence of a novel male intruder until P12. Along with the hippocampus, the BLA also plays a major role in enabling trace conditioning, a conditioning paradigm in which inserts a delay between the presentation of the conditioned stimulus (CS) and unconditioned stimulus (US). In adults, the strength of the conditioning is classically reduced by increasing the interval which separates the presentation of CS and US (Ferry et al., 1999; Moyer et al., 1990). In juvenile rodents, the ability to learn trace conditioning is not present before P15, and develops slowly over the course of the following two weeks until they can perform in a capacity similar to the adults by P28 (Moye & Rude, 1987; Barnet & Hunt, 2005).

Like the neocortical structures with which it shares its ontology, the BLA is composed of two broad populations of neurons - approximately 85% of the nucleus is composed of spiny pyramidal glutamatergic projection neurons (McDonald, 1985; McDonald *et al.*, 1989; Berdel *et al.*, 1997a; Rainnie et al., 1993), and the other 15% is composed of a heterogeneous population of GABAergic interneurons (McDonald, 1985; McDonald & Betette, 2001; Rainnie et al., 2006). BLA interneurons have been segregated into several overlapping subtypes based on their expression of calcium binding proteins (parvalbumin, calbindin, calretinin, etc) and other peptides (cholecystokinin, vasoactive intestinal peptide, somatostatin, etc). Approximately half of GABAergic BLA interneurons are parvalbumin-positive (PV+; McDonald and Mascagni 2001a), and can be further subdivided based on their physiological properties (Rainnie et al., 2006; Woodruff and Sah, 2007a,b). These neurons are of particular interest

because recent research shows that, as in the cortex, PV+ interneurons in the BLA form a syncytial network which allows the neurons to synchronize their activity with a high degree of precision (Muller 2005; Woodruff and Sah, 2007; Gibson 1999, 2005; Beierlein 2000; Deans et al., 2001). Parvalbumin, however, is not expressed in the BLA until around P14, and does not reach mature levels of expression until the end of the first postnatal month (Berdel & Morys, 2000; Dávila et al., 2008). Recent studies by Ogiwara and colleagues indicate that this exact developmental window is critical in the functional maturation of these interneurons (Ogiwara et al., 2013). These studies illustrate clearly that early postnatal development and adolescence are critical windows during which important amygdala functions mature and are established.

The dynamic nature of these developmental periods also confers a certain risk: perturbations during these windows can alter the course of brain development in serious and unpredictable ways, leading to far more serious consequences than for a similar perturbation presented to an mature adult (Hensch & Bilimoria, 2012). Recent research has shown important links between the amygdala and anxiety, depression, and autism (Adolphs *et al.*, 2002; Rainnie *et al.*, 2004; Shekhar *et al.*, 2005; Truitt *et al.*, 2007; Koob & Volkow, 2010). Each of these disorders can appear early in life (Pine *et al.*, 1998; Kim-Cohen *et al.*, 2003; McEwen, 2003; Steinberg, 2005) and early life experience can dramatically increase the likelihood of diagnosable psychiatric illness later in life.

Here we outline a series of studies aimed at addressing our current ignorance of the developmental trajectory of the basolateral amygdala. These studies will provide a foundation for future studies to examine the ways in which alterations to amygdala development, whether by exposure to environmental stress, teratogens, genetic predisposition, or an interaction of these forces, may precipitate the development of common psychopathologies.

Chapter 2

Spike-Timing Precision and Neuronal Synchrony are Enhanced by an Interaction between Synaptic Inhibition and Membrane Oscillations in the Amygdala

Content presented in **Chapter 2** previously published as:
Spike-timing precision and neuronal synchrony are enhanced by an interaction between synaptic inhibition and membrane oscillations in the amygdala. **Ryan SJ**, Ehrlich DE, Jasnow AM, Daftary S, Madsen TE, Rainnie DG. *PLoS One*. 2012;7(4)

Abstract

The basolateral complex of the amygdala (BLA) is a critical component of the neural circuit regulating fear learning. During fear learning and recall, the amygdala and other brain regions, including the hippocampus and prefrontal cortex, exhibit phase-locked oscillations in the high delta / low theta frequency band (~2-6 Hz) that have been shown to contribute to the learning process. Network oscillations are commonly generated by inhibitory synaptic input that coordinates action potentials in groups of neurons. In the rat BLA, principal neurons spontaneously receive synchronized, inhibitory input in the form of compound, rhythmic, inhibitory postsynaptic potentials (IPSPs), likely originating from burst-firing parvalbumin interneurons. Here we investigated the role of compound IPSPs in the rat and rhesus macaque BLA in regulating action potential synchrony and spike-timing precision. Furthermore, because principal neurons exhibit intrinsic oscillatory properties and resonance between 4 and 5 Hz, in the same frequency band observed during fear, we investigated whether compound IPSPs and intrinsic oscillations interact to promote rhythmic activity in the

BLA at this frequency. Using whole-cell patch clamp in brain slices, we demonstrate that compound IPSPs, which occur spontaneously and are synchronized across principal neurons in both the rat and non-human primate BLA, significantly improve spike-timing precision in BLA principal neurons for a window of ~300 ms following each IPSP. We also show that compound IPSPs coordinate the firing of pairs of BLA principal neurons, and significantly improve spike synchrony for a window of ~130 ms. Compound IPSPs enhance a 5 Hz calcium-dependent membrane potential oscillation (MPO) in these neurons, likely contributing to the improvement in spike-timing precision and synchronization of spiking. Activation of the cAMP-PKA signaling cascade enhanced the MPO, and inhibition of this cascade blocked the MPO. We discuss these results in the context of spike-timing dependent plasticity and modulation by neurotransmitters important for fear learning, such as dopamine.

Introduction

The basolateral complex of the amygdala (BLA) is a critical part of the neural circuit regulating fear learning (Campeau et al., 1992; Miserendino et al., 1990; Rodrigues et al., 2001; Davis 2000; LeDoux 2000), and recent evidence suggests that oscillatory activity of neurons in this region plays a key role in regulating affect in awake, behaving animals (for review, see Pape & Parè 2010). More specifically, it is now evident that the amygdala, hippocampus, and prefrontal cortex produce coordinated high delta / low theta (4-5 Hz) oscillations during acquisition (Madsen & Rainnie 2009) and retrieval (Sangha et al., 2009) of learned fear, which then diminish over the course of subsequent extinction learning. Significantly, phase-locked theta stimulation applied simultaneously to the amygdala and hippocampus disrupts fear extinction and prolongs the expression of learned fear (Lesting et al., 2011), further supporting a role of synchronized neural activity in the processes of fear learning and extinction. Moreover, synchronous theta oscillations during REM sleep in the period between fear acquisition and retrieval correlate with changes in fear expression, suggesting that theta oscillations are critical for successful consolidation of fear memory (Popa et al., 2010). Despite the importance of these low frequency oscillations to amygdala function and emotional learning, the mechanisms by which the BLA circuit generates rhythmic activity are largely unknown.

A common mechanism for generating network oscillations utilizes coordinated inhibitory input across multiple neurons to synchronize their action potential firing (Buzsáki 1997; Penttonen et al., 1998; Soltesz & Deschenes 1993; Person & Perkel 2005; Sohal et al., 2006; Szücs et al., 2009; Pouille & Scanziani 2011). The BLA is organized to exploit this phenomenon through the rhythmic interaction of excitatory principal neurons and inhibitory interneurons. BLA principal neurons exhibit compound, rhythmic, inhibitory postsynaptic potentials (IPSPs) that occur at a baseline frequency of

0.5-4 Hz that is sensitive to modulation by dopamine and serotonin (Rainnie 1999; Muly et al., 2009; Loretan et al., 2004). These rhythmic IPSPs are driven by action potentials in local, burst-firing interneurons, which we have previously shown to express parvalbumin (PV^+) (Rainnie et al., 2006). PV^+ interneurons have several characteristics that enable them to influence the activity of large networks of BLA principal neurons synchronously: first, these interneurons make up approximately 40% of the total interneuron population and are distributed throughout the BLA; second, each PV^+ interneuron can innervate the soma and axon hillock of approximately 150 principal neurons (McDonald et al., 2005); finally, these interneurons are coupled electrically by gap junctions to create a functional syncytium (Muller et al., 2005; Woodruff & Sah 2007a,b). Significantly, we and others have shown that, in paired recordings of rat BLA principal neurons, spontaneous IPSPs are highly synchronized (Rainnie 1999; Popescu & Paré 2011), suggesting that the output of PV^+ interneurons may coordinate the activity of large numbers of principal neurons.

Synchronous IPSPs in large groups of BLA principal neurons could also facilitate network oscillations by interacting with intrinsic oscillations in principal neurons to promote rhythmic firing. Intrinsic membrane potential oscillations (MPOs) have been shown to improve spike-timing precision (Schaefer et al., 2006), which is, in turn, important for spike-timing dependent plasticity (Dan & Poo, 2004) and signal processing in neural networks (Mainen & Sejnowski, 1995). BLA principal neurons display a highly consistent MPO (Paré & Gaudreau, 1996; Pape et al., 1998) and an intrinsic resonance (Pape & Driesang 1998), both in the same high delta / low theta frequency band as network oscillations observed during fear learning. If these MPOs were to occur synchronously in groups of BLA neurons, network activity should be promoted at this highly relevant frequency. Considering that groups of cells can have their firing activity entrained by synchronized IPSPs (Hasenstaub et al., 2005), we chose to investigate the

possibility that synchronized, rhythmic IPSPs entrain and phase-lock MPOs and coordinate firing activity in BLA principal neurons. Furthermore, we examine the underlying currents and intracellular signaling cascades regulating these phenomena and discuss potential links to synaptic plasticity and fear learning.

Materials and Methods

Animals and housing conditions

Whole cell patch clamp recordings were obtained from 76 neurons from 48 rodents, and 46 neurons from 13 non-human primates. Rodent experiments were conducted on tissue from male Sprague-Dawley rats at 5-7 weeks of age. All rats were group-housed 4 per cage in Plexiglas cages with corn cob (Bed-O-Cob) bedding. Rats had access to food and water ad libitum, and were maintained in a temperature controlled colony room on a 12:12 light:dark cycle. The non-human primate tissue for this study was obtained from juvenile (18-36 months) *Macaca mulatta* monkeys of both sexes. Non-human primates used in this study were born into the breeding colony housed at the Yerkes National Primate Research Center Field Station and raised in naturalistic social groups. They were provided with *ad libitum* access to food and water and monitored by the Yerkes Veterinary Staff. Animals used in this study were selected for euthanasia by the veterinary staff for failure to thrive and/or chronic diarrhea refractory to treatment as part of the animal care end-points approved for our monkey colony. Once identified, the animals were moved to the Yerkes Main Station and scheduled for euthanasia within the week.

Experiments for Figures 2.1 & 2.2 were performed in both rat and primate tissue, and the remainder of experiments were performed exclusively in rat tissue (see figure legends for details). The care of the animals and all anesthesia and euthanasia procedures in this study were performed according to the National Institutes for Health

Guide for the Care and Use of Laboratory Animals and were approved by the Institutional Animal Care and Use Committee of Emory University.

Electrophysiological procedures

Preparation of acute BLA slices. To obtain slices from the rat basolateral amygdala, animals were decapitated under isoflurane anesthesia (Abbott Laboratories, North Chicago, IL). The brains were rapidly removed and placed in ice-cold kynurenic acid-based artificial cerebrospinal fluid (KA-ACSF), which contained (in mM): NaCl (130), KCl (3.5), KH_2PO4 (1.1), $MgCl_2$ (6.0), $CaCl_2$ (1.0), $NaHCO_3$ (30), glucose (10), thiourea (0.8), sodium pyruvate (2), ascorbic acid (0.4), and kynurenic acid (2). The glutamatergic antagonist kynurenic acid was included in the KA-ACSF to suppress any excitotoxic effects of glutamate release that may occur due to tissue slicing. A block of tissue containing the BLA was then mounted in a Leica VTS-1000 vibrating microtome (Leica Microsystems, Bannockburn, IL), and 350 µm coronal slices were cut. Slices were hemisected and hand-trimmed to remove excess tissue dorsal to the amygdala. For the primate basolateral amygdala, the animals were euthanized with an overdose of pentobarbital (100 mg/kg) and hand-cut blocks of tissue from the medial temporal lobe were mounted in a vibratome and 400 µm coronal slices were cut as previously described (Muly et al., 2009). Slices from both species were transferred to a holding chamber containing KA-ACSF at 32°C and gassed with a 95%/5% O_2/CO_2 mixture for 40 min before being placed in oxygenated regular ACSF (ACSF) at room temperature containing (in mM): NaCl (130), KCl (3.5), KH_2PO_4 (1.1), $MgCl_2$ (1.3), $CaCl_2$ (2.5), $NaHCO_3$ (30), glucose (10), thiourea (0.8), sodium pyruvate (2), and ascorbic acid (0.4).

Recording procedures. For recording, slices were placed in a Warner Series 20 recording chamber (Warner Instruments, Hamden, CT) mounted on the fixed stage of a Leica DM-LFS microscope (Leica Microsystems, Bannockburn, IL). Slices were fully submerged and continuously perfused at a rate of 1-2 mL/min with heated (32°C) and

oxygenated ACSF. Neurons were selected for recording under IR-DIC illumination with a 40X water immersion objective. Images were captured with a Hamamatsu Orca ER CCD camera (Hamamatsu, Tokyo, Japan) controlled by SimplePCI software (Compix, Sewickley, PA). Whole cell patch-clamp recordings were conducted using thin-walled borosilicate glass-patch electrodes (WPI, Sarasota, FL) which were pulled on a P-97 Flaming / Brown micropipette puller (Sutter Instruments, Novato, CA). Patch electrodes had resistances ranging from 4-7 MΩ when filled with standard patch solution that contained (in mM): K-gluconate (138), KCl (2), $MgCl_2$ (3), phosphocreatine (5), K-ATP (2) NaGTP (0.2), HEPES (10), and biocytin (3 mg/mL). The patch solution was adjusted to a pH of 7.3 with KOH and had a final osmolarity of approximately 280 mOsm. Junction potentials were offset manually prior to patching neurons. Access resistances were monitored throughout recordings and neurons with more than a 15% change were discarded. In the case of paired recordings, two neurons were selected for patching within a single 40X visual field. Neuronal types were pre-selected based on somatic morphology, and type was verified based on electrophysiological profile, as described previously for rat (Rainnie et al., 1993) and non-human primate (Muly et al., 2009).

All recordings were performed in principal neurons of the basolateral nucleus of the amygdala, contained in the basolateral complex. Recordings were obtained using an Axopatch-700A amplifier (Molecular Devices, Sunnyvale, CA), a Digidata 1320A A/D interface, and pClamp 10 software (Molecular Devices). For all experiments, whole cell patch-clamp configuration was established, and cell responses were recorded in either current clamp or voltage clamp mode. Data were filtered at 5 kHz in current clamp and 2 kHz in voltage clamp, and sampled at a rate of 10 kHz. Neurons were excluded from analysis if their resting membrane potential (V_m) was more positive than -55 mV or if their action potentials did not surpass +5 mV.

Drug Application.

Drugs were applied by gravity perfusion at the required concentration in the circulating ACSF. Drugs used: cesium chloride (CsCl), 5 mM; nickel chloride ($NiCl_2$), 500 µM; 4-aminopyridine (4-AP), 100-500 µM; tetrodotoxin (TTX), 1 µM; tetraethylammonium chloride (TEA-Cl), 20 mM; forskolin, 10 µM; dideoxy-forskolin, 10 µM; 1,2-bis(o-aminophenoxy)ethane-N,N,N',N'-tetraacetic acid (BAPTA), 5 mM purchased from Sigma–Aldrich (St. Louis, MO); 6,7-dinitroquinoxaline-2,3-dione (DNQX), 20 µM; RS-CPP, 10 µM; CGP 52432, 2 µM; 4-(N-ethyl-N-phenylamino)-1,2-dimethyl-6-(methylamino) pyridinium chloride (ZD7228), 60 µM; (1R,4R,5S,6R)-4-amino-2-oxabicyclo[3.1.0]hexane-4,6-dicarboxylic acid (LY379268), 50 µM; 8-Br-cAMP, 5-10 µM; and (R)-adenosine, cyclic 3',5'-(hydrogenphosphorothioate) triethylammonium (cAMPs-RP), 25 µM purchased from Tocris (Ellisville, MO). All drugs were stored frozen as concentrated stock solutions in dH_2O except DNQX, which was made in 50% dimethyl sulfoxide and buffered to pH 7.3.

Spike-timing precision, resonance, and oscillations. To assess the effect of IPSPs on spike-timing precision, repetitive action potentials were evoked with a depolarizing, square-wave current step of amplitude set to evoke 4-8 Hz firing from a holding potential of -60 mV. The current injections were repeated five times with an inter-event interval of 10 seconds. To examine the effect of synaptic inhibition on spike-timing precision, the current in the depolarizing step was transiently removed for 15 ms and then ramped back over 100 ms to the command amplitude to mimic compound spontaneous IPSPs observed in BLA principal neurons. Alternatively, pharmacologically isolated, compound, synaptic IPSPs were evoked using electrical stimulation within the dorsal BLA, just medial to the external capsule. The two IPSPs in each sweep were applied 550 and 1415 ms into the depolarizing step, separated by 865 ms start-to-start (~1.2 Hz), to mimic the frequency of spontaneous IPSPs previously observed in our laboratory.

To examine the membrane potential oscillation of BLA principal neurons, cells were held at -60 mV and injected with the same transient (2.5 s) square-wave depolarizing current pulse as described above. TTX (1 μM) was included in all experiments investigating the membrane oscillation. The voltage response to the DC current pulse was recorded and characterized in regular ACSF and also in varying drug conditions. The amplitude of the current pulse was adjusted such that the steady state membrane potential achieved during current injection was similar before and during drug application (between -40 and -30 mV). Any drug-induced changes in resting membrane potential were compensated for by DC current injection before initiating the transient square-wave depolarizing current pulse to assess the effect on membrane potential oscillations. To assess resonance frequency, principal neurons were held at -60 mV with DC current injection and a sinusoidal frequency sweep of constant current amplitude was injected, increasing from 1-12 Hz over a period of 8 seconds, and the voltage response of the cell was recorded.

Data and statistical analysis

The correlation of spontaneous IPSPs and burst-firing from paired recordings of BLA neurons were analyzed by first identifying event times using pClamp software and then using a Pearson product-moment correlation. Spike-timing precision was assessed using a correlation-based metric adapted from Schreiber et al., 2003. The correlation statistic (R_{corr}) was calculated for windows of 200 ms every 66 ms, using the equation (**Equation 2.1**) as published. Briefly, spike times from N traces were convolved with a Gaussian filter of pre-determined width (σ) to create spike vectors (*s*). For experiments involving artificial and evoked IPSPs, σ = 6 ms, and to prevent a floor effect due to lower spike rates, for experiments with spontaneous IPSPs, σ = 20 ms. The degree of correlation between the vectors (s_i, s_j) was calculated using a dot-product normalized to the product of their magnitudes and the number of comparisons being made.

Equation 2.1 $$R_{corr} = \frac{2}{N(N-1)} \sum_{i=1}^{N} \sum_{j=i+1}^{N} \frac{\vec{s}_i \cdot \vec{s}_j}{\left|\vec{s}_i\right|\left|\vec{s}_j\right|}$$

When calculating spike-timing precision within cells, all 5 traces (N = 5) were compared using this algorithm; when calculating across cells, only the 2 traces (N = 2) which occurred simultaneously were compared, and 5 comparisons were made and averaged. Statistical analyses were performed using a two-way Analysis of Variance (ANOVA), with Bonferroni post-tests to compare across windows and conditions.

Oscillations of the membrane potential of BLA principal neurons were analyzed by means of multi-taper spectral analysis using a custom program that was modified from the Chronux toolbox (Mitra & Bokhil, 2008). The resonance frequency of BLA principal neurons was analyzed with fast Fourier transforms (FFT) in pClamp 10 (Molecular Devices) using a Hamming window. Power spectra (mV^2/Hz) were converted into standardized Z-scores and peak amplitudes were analyzed using a one-way ANOVA.

Results

Non-Human Primate BLA principal neurons receive spontaneous, synchronized, rhythmic IPSPs that coordinate action potential timing.

We have shown previously that approximately 80% of principal neurons in slice preparations of the rat BLA receive spontaneous, compound IPSPs that occur rhythmically at frequencies ranging from 0.5-2 Hz, with a mean of 1.2 Hz, in control ACSF (Rainnie 1999). These compound IPSPs were observed in principal neurons with varying intrinsic properties (mean ± SD: input resistance 85 ± 28MΩ, action potential threshold -43 ± 3.5mV, action potential half width 0.8 ± 0.1ms, data not shown). Here we show that compound IPSPs are also observed in 67% of primate BLA slices with a frequency of 0.76 ± 0.33 Hz, similar to the rat (n = 46, **Figure 2.1A, B**). As in the rat

BLA, compound IPSPs in the primate BLA were highly rhythmic, with a coefficient of variation of instantaneous frequency of 0.30 ± 0.09 (n = 12). Compound IPSPs occur synchronously across multiple neurons in the rat BLA (Rainnie 1999; Popescu & Paré, 2011), and new analysis reveals they have a near perfect correlation in time across pairs of principal neurons (Pearson product-moment correlation, R^2 = 0.999; n = 11, data not shown). We extend this observation to show that compound IPSPs are also highly synchronized across pairs of primate neurons (Figure 1A; Pearson product-moment correlation, R^2 = 1.0; n = 5, data not shown), suggesting this is an evolutionarily conserved phenomenon.

Using paired recordings from a burst-firing interneuron and a principal neuron, we extend previous observations in the rat BLA (Rainnie 1999; Popescu & Paré, 2011) to the primate. Here we show that compound IPSPs observed in BLA principal neurons (**Figure 2.1C**, upper trace) coincide with rhythmic bursts of action potentials occurring in burst-firing interneurons (lower trace, n = 2**;** Pearson product-moment correlation, R^2 = 0.999, data not shown), which we have previously shown in the rat BLA to express the calcium-binding protein PV^+ (Rainnie et al., 2006). **Figure 2.1C** illustrates a typical burst-IPSP pair at higher temporal resolution. Compound IPSPs with a similar waveform can also be observed in principal neurons if an interneuron is driven to fire bursts of action potentials by direct current injection (**Figure 2.1E**). Previously, we have shown that these compound IPSPs were abolished by application of either the $GABA_A$ receptor antagonist, bicuculline, or the AMPA receptor antagonist, CNQX, suggesting glutamatergic input drives burst-firing PV^+ interneurons to release GABA at multiple sites onto BLA principal neurons (Rainnie, 1999). Each parvalbumin interneuron can innervate more than 150 BLA principal neurons (Muller et al., 2006), further suggesting that spontaneous, compound IPSPs are highly synchronized across a larger population of principal neurons than the pairs we show here.

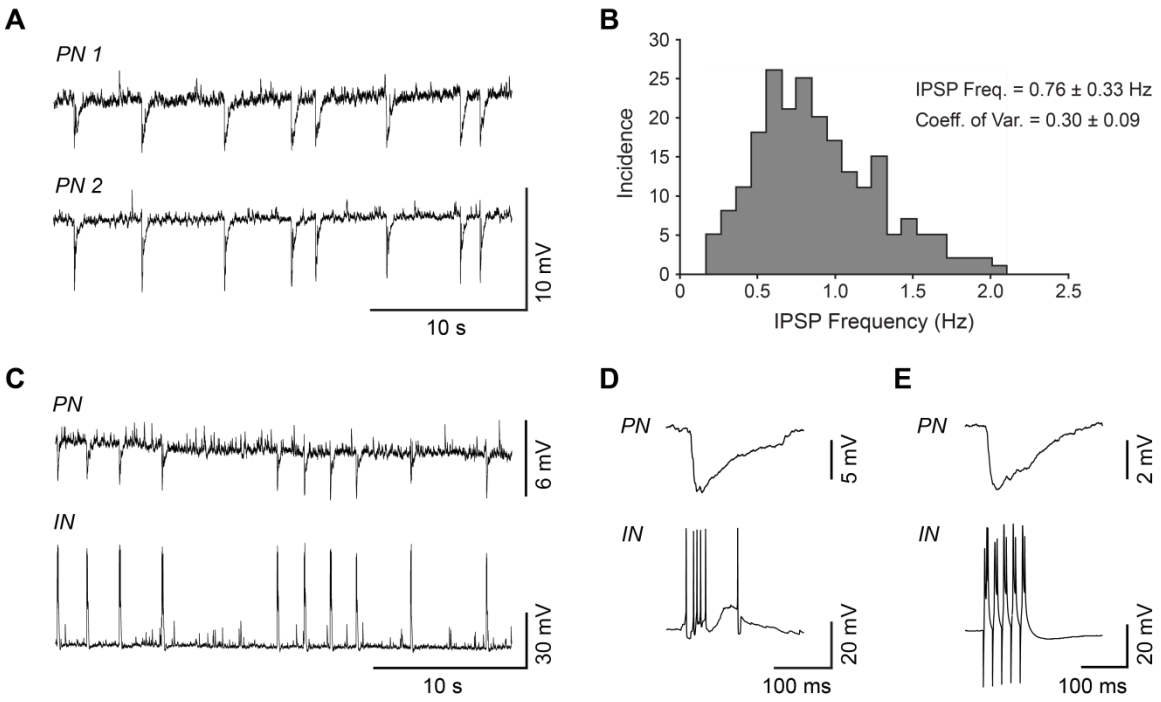

Figure 2.1: Spontaneous, compound IPSPs in the BLA were synchronized across principal neurons and with bursts in inhibitory interneurons. *(A) A representative pair of primate BLA principal neurons, held at -60 mV, showing compound IPSPs that are rhythmic and highly synchronized, observed during gap-free recordings. (B) A histogram plotting instantaneous frequency of compound IPSPs during 30-second recordings from 12 primate BLA principal neurons. (C) Paired recordings in the primate BLA of a principal neuron receiving compound IPSPs and a burst-firing parvalbumin interneuron, both held at -60 mV. (D) An example of a burst-IPSP pair shown at higher temporal resolution. (E) A compound IPSP can be induced in a BLA principal neuron by using current injection to drive bursting activity in the interneuron.*

Elsewhere in the brain, IPSPs have been shown to interact with subthreshold membrane potential oscillations (MPOs) to improve stimulus discrimination and action potential precision in neurons (Schaefer et al., 2006; Mainen & Sejnowski, 1995). We were therefore interested in the ability of synchronized, compound IPSPs to coordinate

firing activity within networks of BLA principal neurons. As illustrated in **Figure 2.2**, compound IPSPs are capable of coordinating activity in the BLA, improving the temporal coherence of spontaneous action potentials between pairs of primate BLA principal neurons. When neurons were depolarized to threshold for action potential generation, action potentials occurring upon rebound from an IPSP-induced membrane hyperpolarization were highly coincident across cells (**Figure 2.2A**, shaded regions). To identify periods with consistent spike-timing across cells, we used a correlation-based metric with a sliding window (see Methods Schreiber et al., 2003), where a value of 1 indicates identical spike-timing and a value of 0 indicates no timing correlation. Action potentials during a window directly following spontaneous, compound IPSPs had improved temporal coherence across pairs of neurons compared to those preceding IPSPs (**Figure 2.2B**). Interestingly, upon rebound from compound IPSPs, a subpopulation of primate BLA principal neurons (3/11 cells) exhibited an increased and more consistent firing rate (from 3.6 to 7.4 Hz, coefficient of variation from 0.56 to 0.28) (**Figure 2.2C**). Moreover, clusters of action potentials showing a consistent firing rate and high coherence following compound IPSPs were also observed in 2/6 paired recordings (**Figure 2.2D**). In the course of these experiments it was noted that compound IPSPs could elicit a damped oscillation on rebound, suggesting the observed effects on action potential patterning may be due to an interaction with an intrinsic MPO (**Figure 2.2E**).

Together these observations strongly suggest that compound IPSPs coordinate the firing activity of principal neurons in both the rat and primate BLA, and their prevalence and synchrony further suggest that this coordination extends across large groups of principal neurons. To better assess the interactions of compound IPSPs with intrinsic properties of BLA principal neurons, subsequent experiments examined the

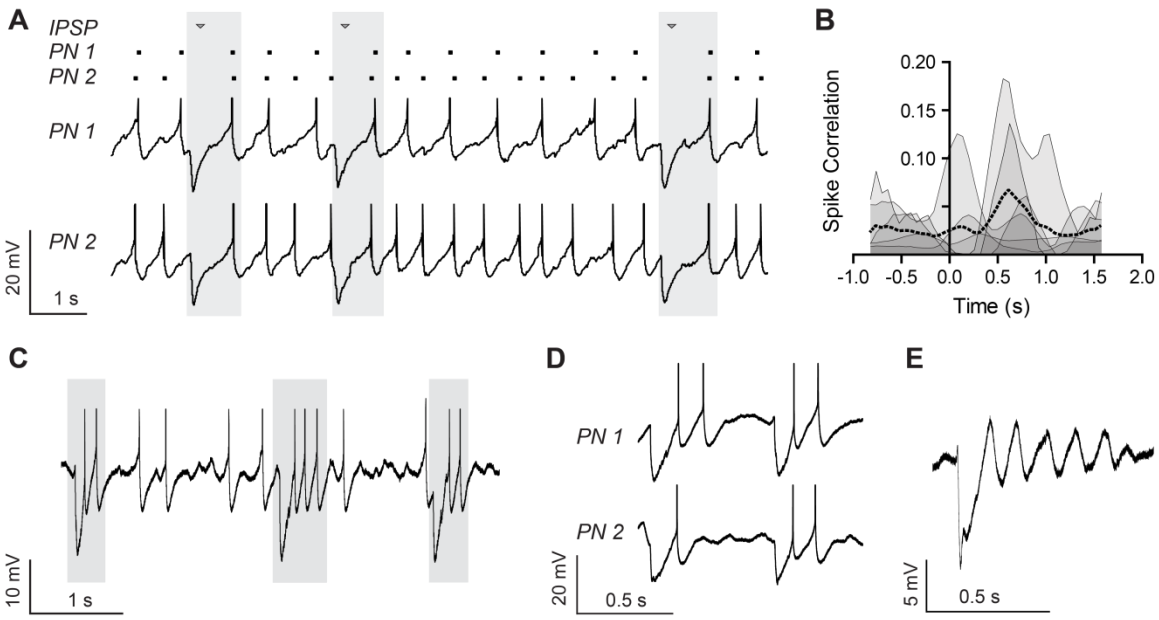

Figure 2.2: Spontaneous, compound IPSPs coordinated spike timing and promoted rhythmic firing in the primate BLA*. (A) Spontaneous, compound IPSPs exhibited by a representative pair of primate BLA projection neurons, depolarized to action potential threshold (-45 to -40 mV) using a DC current injection. A raster plot highlights the relative synchrony of spikes following the IPSPs, highlighted in gray boxes. Action potentials are cropped at -30 mV (n = 6). (B) A spike correlation metric (see Methods) is plotted for 6 pairs of primate BLA principal neurons exhibiting compound IPSPs and depolarized to threshold, as in A. Correlation is plotted for each pair as an individual, smoothed trace (thin black lines) representing the mean correlation surrounding every spontaneous, compound IPSP, with the peak of each IPSP aligned to time 0. The mean of all 6 pairs is superimposed as a dotted black line. (C-D) A representative single (C, n = 4) and pair of (D, n = 2) primate BLA principal neurons exhibiting rhythmic firing upon rebound from spontaneous, compound IPSPs. Neurons were depolarized to threshold, as in A. IPSPs and rebound firing are highlighted with gray boxes in C. Action potentials were cropped at -30mV. (E) A primate BLA principal neuron, depolarized as in A, exhibiting a damped membrane potential oscillation in response to a spontaneous, compound IPSP.*

effects of IPSPs on spike trains in the absence of synaptic noise. Moreover, given the scarcity of primate tissue, all experiments were performed in the rat.

Compound IPSPs enhance spike-timing precision in rat BLA principal neurons.

We first examined the effect of IPSPs on the precision of action potential timing in a neuron depolarized to action potential threshold with DC current injection. In order to better isolate the effects of intrinsic currents on spike timing, we blocked synaptic currents with a mixture of glutamate and GABA receptor antagonists (see Methods). As illustrated in **Figure 2.3A**, BLA principal neurons displayed a regular action potential firing pattern when held at -45 mV. When ten sweeps from the same neuron were aligned using an action potential as the trigger (**Figure 2.3B**), it was apparent that subtle variations in inter-spike interval accumulated over the course of the train, such that the timing of spikes at the end of the train was less consistent than at the beginning. Conversely, when two simulated IPSPs were injected during 10 sweeps captured randomly in time (**Figure 2.3C**), the phase of spiking was reset and spike times became much more consistent across sweeps.

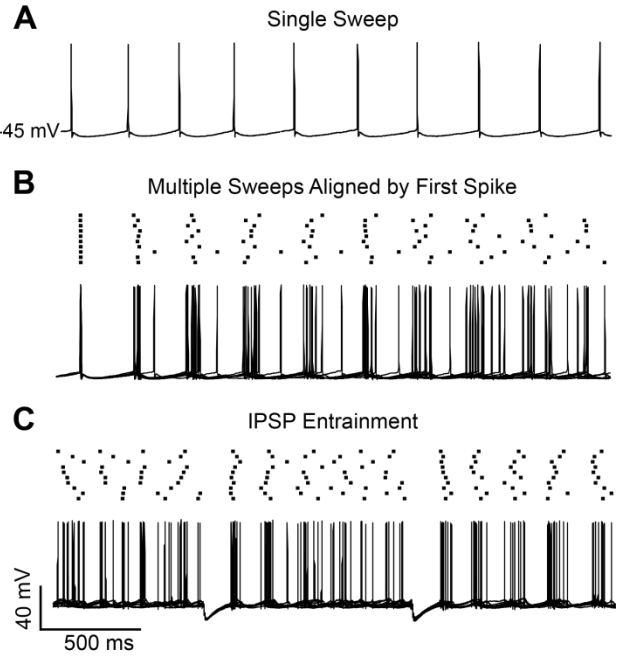

Figure 2.3: Spike-timing precision diminishes in spike trains and is reset by compound IPSPs. *(A) A single sweep recorded from a spiking BLA principal neuron, held at -45 mV by steady-state current injection, displaying a typical regular firing pattern. (B) Multiple sweeps like that in A overlaid and aligned by their first spikes. A raster plot illustrates decay of spike-timing reliability. (C) Injection of artificial IPSPs recovers spike-timing precision.*

Having established that artificial IPSPs can improve spike-timing precision in free-firing neurons, we next sought to quantify this effect. Specifically, we used transient (2.5 s) steps of injected current to elicit a spike train and determine the effect of IPSPs on spike-timing precision in individual principal neurons, and between pairs of principal neurons. Similar to when neurons are free-firing, the timing of the first few spikes in a train was extremely consistent across sweeps, but the timing of subsequent spikes became less consistent as the train progressed because small variations in the inter-spike interval accumulated (**Figure 2.4A**). Here we used the same correlation-based metric as described for **Figure 2.2B**, adapted to compare across five sweeps recorded in a single neuron (see Methods). This analysis revealed that, at the onset of the train, spike-timing was extremely precise with an initial correlation value of 0.75 ± 0.13 (mean ± SD), which then diminished to 0.26 ± 0.20 within 300 ms (**Figure 2.4D,** Control, n = 11).

We next evaluated spike-timing precision in the presence of stimulus-evoked IPSPs (**Figure 2.4B**). Electrical stimulation of the dorsolateral BLA in the presence of glutamate receptor antagonists elicited a monosynaptic IPSP in principal neurons that had a similar amplitude and duration to the spontaneous compound IPSPs. We also examined the effects of artificial IPSPs, elicited with hyperpolarizing current injection, on spike-timing precision (**Figure 2.4C**). Activation of either evoked or artificial IPSPs during the action potential train resulted in a significant improvement in spike-timing precision compared to the control condition (Two-way ANOVA with repeated measures, effect of group: $F_{2,800} = 136.3$, $p < 0.0001$). Both types of IPSPs significantly increased correlation values relative to the control condition for approximately 270 ms following each IPSP (effect of interaction: $F_{78,800} = 4.72$, $p < 0.0001$, Bonferroni post-tests). Evoked IPSPs improved correlation values from a baseline of 0.19 ± 0.11 to a peak of 0.47 ± 0.11 (n = 11) immediately following the IPSPs (**Figure 2.4D**). As illustrated in

Figure 2.4F, artificial IPSPs had a more pronounced effect on spike-timing precision than evoked IPSPs, with a peak correlation value of approximately 0.71 ± 0.21 (n = 11) following each IPSP. Only at the peak points of the correlation, however, was there any significant difference in how the two IPSP manipulations affected spike-timing precision.

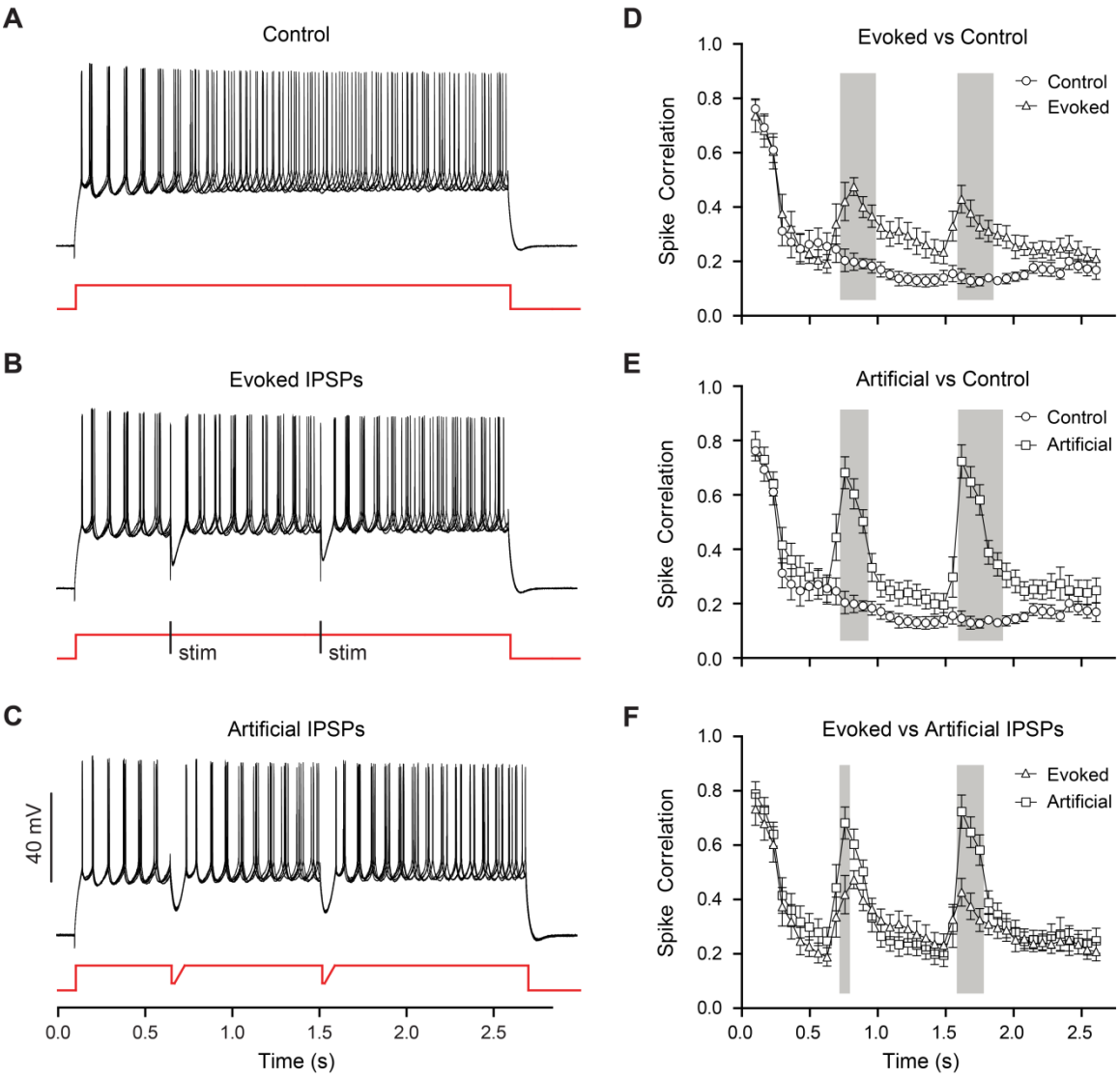

Figure 2.4: Artificial and evoked compound IPSPs improved spike-timing precision in individual BLA principal neurons. *(A) Five superimposed traces from a representative principal neuron, held at -60 mV, showing a train of action potentials in response to a depolarizing current step in the presence of DNQX (20 μM), RS-CPP (10*

μM) and CGP (2 μM); note the loss of spike-timing precision as the spike train progresses. (B, C) Similar traces to A with the injection of evoked (B) or artificial (C) compound IPSPs to demonstrate improvement of spike-timing precision following a compound IPSP. (D, E, F) Comparisons of spike-timing precision for neurons with no IPSPs (Control, n = 11), evoked IPSPs (n = 11), and artificial IPSPs (n = 11), assessed with a spike correlation metric (see Methods) and plotted as mean ± SEM. Comparisons were made using a two-way ANOVA (see Results), and windows of significant differences ($p < 0.05$) in spike correlation are denoted with grey boxes.

Compound IPSPs synchronize the firing activity of multiple BLA principal neurons.

We next quantified the ability of compound IPSPs to improve firing coherence across multiple BLA principal neurons, using a similar metric as above to measure the correlation of spike times in simultaneously recorded sweeps across the two neurons. In the absence of IPSPs, spike-timing across BLA neurons showed low coherence, such that the correlation-based metric reached an initial peak of only 0.27 ± 0.39 which then declined rapidly to 0.09 ± 0.07 (n = 6) within 300 ms (**Figure 2.5C**). The introduction of 2 evoked IPSPs was not able to significantly improve the coherence of spike times between neurons, likely due to the observed inconsistency in the amplitude and duration of the evoked IPSP waveform between neurons (data not shown). Because artificial IPSPs have a highly consistent waveform across pairs of neurons and therefore mimic the consistency of spontaneous, compound IPSPs better than do evoked IPSPs, we also tested the effect of 2 artificial IPSPs on spike-timing. Artificial IPSPs significantly increased the coherence of spike times between pairs of neurons in the period immediately following the IPSPs (Two-way ANOVA with repeated measures, effect of interaction: $F_{39,200} = 2.123$, $p < 0.001$, Bonferroni post-tests), with an improvement from a

baseline of 0.09 ± 0.12 to a peak of approximately 0.42 ± 0.27 (n = 6) in the correlation-based metric (Figure 5B, D). These data strongly suggest that synchronized IPSPs enhance spike-timing precision of BLA principal neurons and can serve to entrain the firing activity of multiple neurons, despite inherent differences in their intrinsic electrophysiological properties (e.g., membrane input resistance, time constants of membrane charging, and firing frequency).

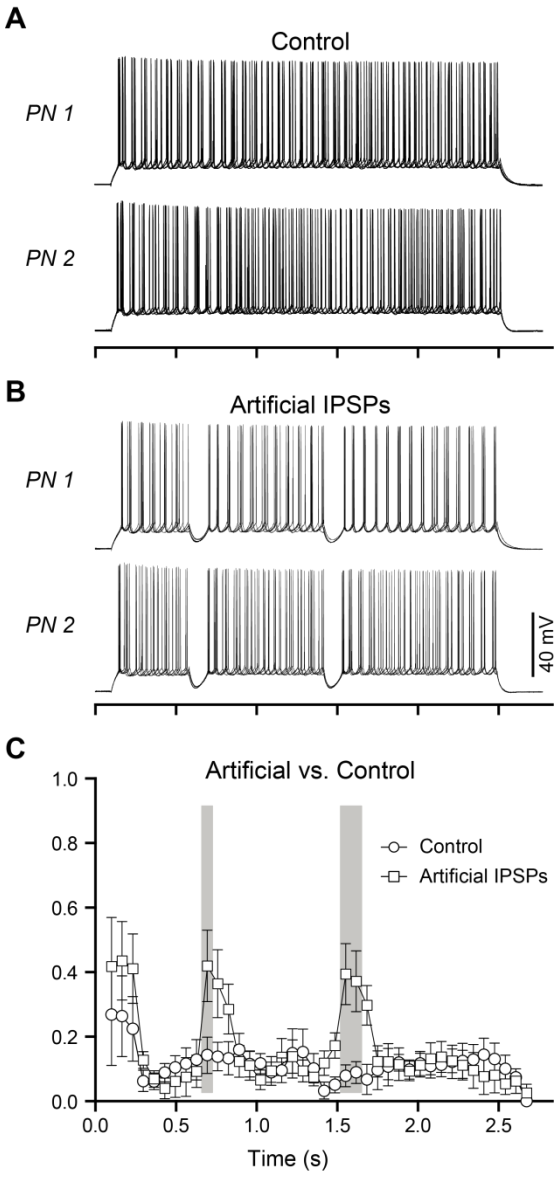

Figure 2.5: Artificial, compound IPSPs coordinated spike timing across pairs of BLA principal neurons. *(A) Five overlaid, consecutive traces of action potentials during paired recordings of BLA principal neurons, held at -60 mV, in response to a depolarizing current injection without IPSPs and (B) with two IPSPs. (C) Spike correlation metric calculated across pairs of neurons when artificial IPSPs are injected compared to the control condition (n = 6 pairs), plotted against time. Comparisons were made using a two-way ANOVA (see Results), and grey boxes denote windows of significant differences (p < 0.05) in spike correlation.*

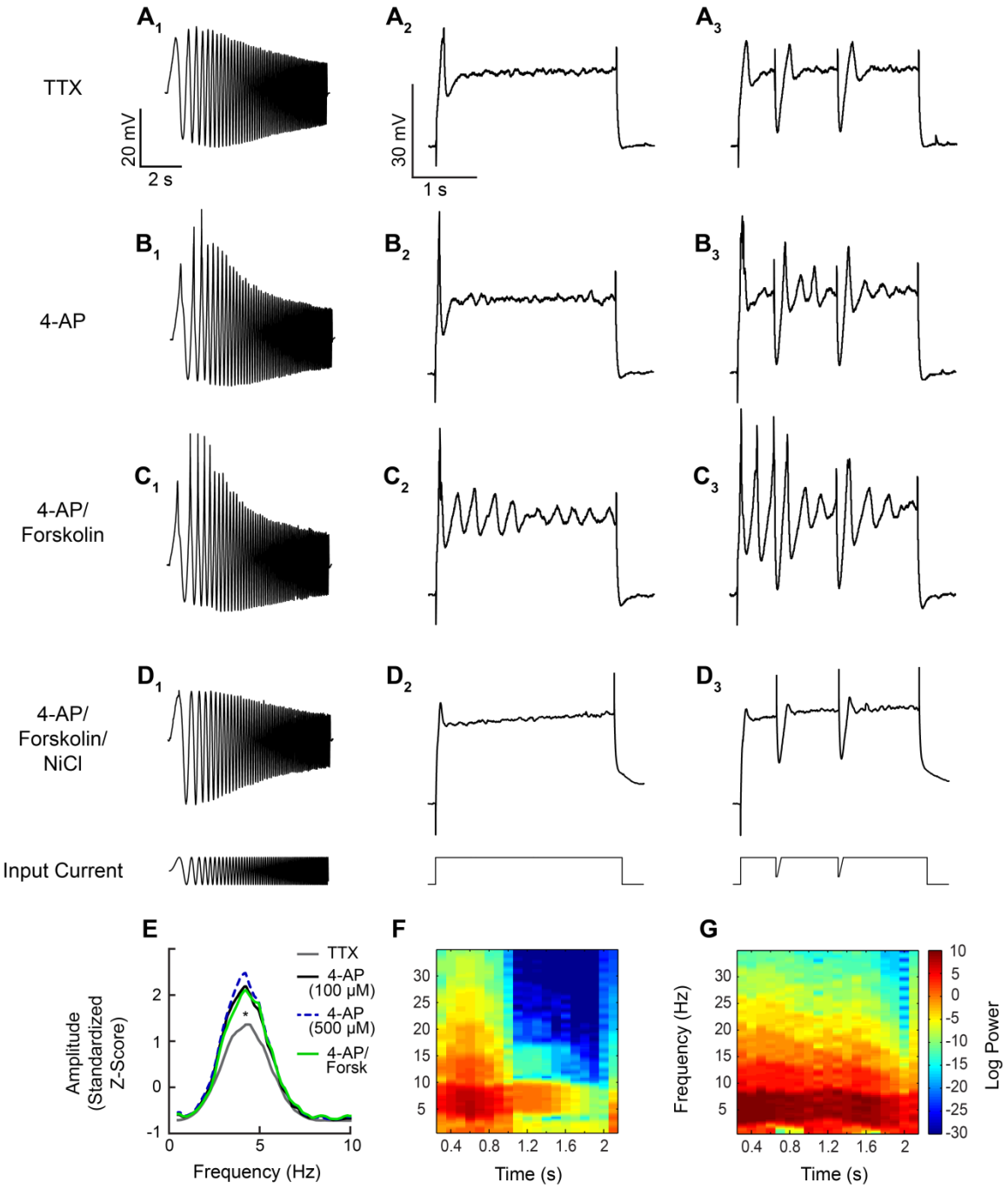

Figure 2.6: BLA principal neurons exhibited a modifiable intrinsic resonance and a membrane potential oscillation that was facilitated by compound IPSPs. *(A1-D1) Principal neuron membrane potential response to injection of a sinusoidal current with constant amplitude and linearly changing frequency (0-12 Hz) in the presence of various drug cocktails. All neurons were held at baseline of -60 mV. (A1) Typical voltage*

response to the sinusoidal current in TTX (1 μM). The resonance of BLA principal neurons can be enhanced by application of 4-AP (B1, 500 μM) and the adenylyl cyclase activator, forskolin (C1, 10 μM), and is abolished by application of NiCl (500 μM, D1). Analysis of power spectra (E) shows that the enhancement of resonance by 4-AP and forskolin is significantly different from baseline ($p < 0.05$). (A2-D3) Intrinsic membrane oscillations of BLA principal neurons, held at -60 mV, in response to a steady depolarizing current injection (A2-D2) and in response to the same current injection with superimposed IPSPs (A3-D3). Similar to resonant properties, membrane oscillations are enhanced by application of 4-AP and forskolin, and abolished in NiCl. Injection of artificial IPSPs in A3-D3 significantly enhanced the amplitude and duration of oscillations (F and G; spectrograms illustrate data from C2 and C3 respectively).

Based on our prior observation that spontaneous, compound IPSPs not only entrain action potential firing, but also promote rhythmic firing and unmask a damped membrane potential oscillation, we hypothesized that the ability of compound IPSPs to coordinate firing would be facilitated by an interaction with intrinsic oscillatory properties of principal neurons. Therefore, we next characterized the interaction of compound IPSPs with intrinsic oscillatory properties of BLA principal neurons.

Compound IPSPs facilitate an intrinsic membrane potential oscillation in BLA principal neurons.

Most central nervous system neurons exhibit a preferred resonance frequency that provides them with the ability to filter synaptic input based on frequency (Hutcheon et al., 1996a,b; Hutcheon & Yarom, 2000). Pape and colleagues have reported that principal neurons in the lateral amygdala of the cat have an intrinsic resonance frequency in the range of 1-3.5 Hz (Pape & Driesang, 1998). Here we extend these observations to show that BLA principal neurons of the rat also have an intrinsic

resonance (**Figure 2.6A$_1$-D$_1$**, n = 8), with a preferred frequency at 4.2 ± 0.1 Hz (**Figure 2.6E**).

Many of the membrane currents that contribute to the resonant properties of neurons have also been implicated in mediating long-lasting, sub-threshold MPOs in the BLA as well as other brain regions (Pape et al., 1998; Pape & Driesang, 1998; Hutcheon et al., 1996a,b; Hutcheon et al., 1994). To determine whether compound IPSPs interact with an intrinsic MPO in principal neurons, we next examined the effect of IPSPs on membrane voltage in neurons depolarized to threshold in the presence of TTX (1 µM; n = 6). As illustrated in **Figure 2.6A$_2$**, depolarizing current injection evoked a transient depolarizing voltage deflection at the onset of current injection but did not elicit an MPO in BLA principal neurons. Furthermore, injection of artificial IPSPs evoked a similar depolarizing voltage deflection on the rebound of each IPSP, but did not elicit an MPO (**Figure 2.6A$_3$**). We hypothesized that the basal state of the neurons in the slice preparation might not be conducive to the expression of an MPO, and that modulation of intrinsic currents might be necessary to reveal the presence of an MPO.

The membrane potential oscillation is sensitive to modulation of its component currents.

Work by Pape and colleagues has shown that MPOs in the BLA can be enhanced by modulating a select population of voltage-activated currents including, but not limited to, the hyperpolarization-activated cation current (I_H) and the low-threshold Ca^{2+} current (I_T) (Pape et al., 2005). Significantly, an interaction between I_H and I_T is also thought to be a key element in the regulation of intrinsic resonance (Hutcheon et al., 1996a,b; Hutcheon et al., 1994). The I_T current is often opposed by the transient K^+ current, I_A (Hammack et al., 2007; Anderson et al., 2010; Russier et al., 2003; Molineux et al., 2005), which has been shown to regulate firing activity in BLA principal neurons (Gean & Shinnick-Gallagher, 1989). Thus, we reasoned that blocking I_A channels could

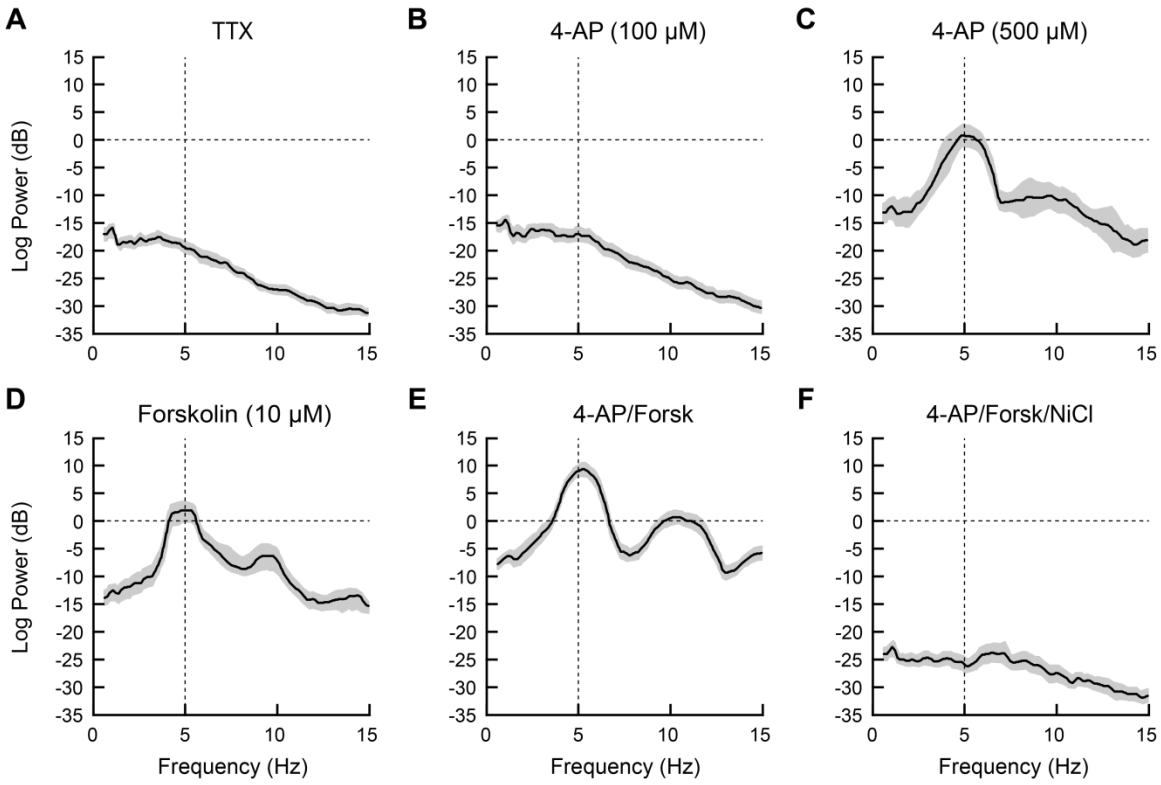

Figure 2.7: The peak power of the membrane potential oscillation was sensitive to modulation of I_A and I_T and activation of PKA. *Power spectra of MPOs in BLA PNs in response to a depolarizing step with artificial IPSPs, with mean (solid lines) and 95% confidence intervals (shaded region). Frequencies at which the 95% confidence intervals do not overlap indicate statistically significant differences among the plots. (A) In the presence of TTX, neurons exhibit a weak MPO. (B,C) MPOs were not enhanced by bath application of 100 µM 4-AP (B) but were significantly enhanced by 500 µM 4-AP, with peak power at 4.9 Hz (C). (D) Application of forksolin, an activator of the c-AMP cascade, at 10 µM also enhanced a MPO with peak power at 4.8 Hz. (E) The MPO was significantly enhanced by a combination of 500 µM 4-AP and 10 µM forskolin, with peak power greater than for either drug alone but occurring at a similar frequency. (F) The MPO observed in forskolin and 4-AP was completely abolished by co-application of NiCl (500 µM) to block low-threshold calcium channels.*

effectively enhance I_T and thus facilitate resonance behavior in BLA principal neurons and unmask an MPO. Bath application of the non-selective I_A channel blocker, 4-aminopyridine (4-AP), at 100µM (**Figure** 2.**6E**) and 500µM (**Figure 2.6B$_1$ & 2.6E**) both significantly enhanced the amplitude of the peak resonance (One-way ANOVA, Tukey post-tests, $F_{3,46}$ = 8.763, $p < 0.05$). Application of 500 µM 4-AP also enhanced the expression of the transient depolarizing voltage deflection and unmasked a small, transient MPO at the onset of the depolarizing step (**Figure 2.6B$_2$**). Furthermore, in the presence of 4-AP, the introduction of artificial IPSPs (**Figure 2.6B$_3$**) enhanced the amplitude of the MPO, which had peak power at approximately 5 Hz (**Figure 2.7A-C**, n = 6).

Importantly, I_T, I_H, and I_A channels are all substrates for phosphorylation by protein kinase-A (PKA), which decreases the conductance of I_A channels and increases the conductance of I_H and I_T channels (Kim et al., 2006; Kamp & Hell 2000; Ramadan et al., 2009; Gerhardstein et al., 1999; Vargas & Lucero 2002; Ingram & Williams, 1996; Hoffman & Johnston, 1998). Thus, we next examined the effects of the PKA activator, forskolin, on the resonance properties of BLA principal neurons. As illustrated in **Figure 2.6C$_1$**, bath application of forskolin (10 µM) in combination with 4-AP (500 µM) significantly increased the amplitude of the resonance peak compared to TTX controls (One-way ANOVA, Tukey post-test, $F_{3,46}$ = 8.763, $p < 0.05$). However, the peak power of the resonance in 4-AP and forskolin was not significantly different than that observed in the presence of 4-AP alone (**Figure 2.6E**). In the context of the depolarizing step, the addition of forskolin (10 µM) in combination with 4-AP (500 µM) enhanced both the amplitude and duration of the MPO in all neurons tested (**Figure 2.6C$_2$**). The MPO resembled a damped oscillation (Pape & Driesang, 1998) and, as can be seen in Figure 6F, the power of the MPO was greatest at the onset of the depolarizing current injection and declined over time. In the majority of neurons the MPO was seen to terminate

before the conclusion of the depolarizing current injection. The introduction of artificial IPSPs further enhanced the oscillation (**Figure 2.6C$_3$, G**) without changing the preferred frequency (**Figure** 2.**7E**, compared to 2.**7C** and 2.**7D**). Application of forskolin (10 μM) alone also unmasked an MPO, similar to the effects of 500 μM 4-AP, with a peak frequency at 4.8 Hz in all neurons tested (n = 4) (**Figure 2.7D**). Hence, activation of the cAMP-signaling cascade alone can facilitate the expression of the MPO in BLA principal neurons.

In other brain regions, MPOs are partially dependent on the activation of I_T channels, and as the transient depolarizing voltage deflections observed upon rebound from the IPSPs were reminiscent of low-threshold calcium spikes, we next determined whether blocking I_T channels with 500 μM NiCl (Lee et al., 1999) would inhibit the combined response to forskolin and 4-AP. Application of NiCl diminished the resonant properties of BLA principal neurons (**Figure 2.6D$_1$**) and completely blocked the forskolin- and 4-AP-induced MPO in all neurons tested (n = 6) (**Figure 2.6D$_{2-3}$, 2.7F**), suggesting that an interaction between I_T and voltage-gated K^+ channels, most likely I_A channels, play a critical role in MPO expression in BLA neurons.

Application of high-micromolar 4-AP, however, can also block other K^+ channels, including several that are also sensitive to micromolar concentrations of TEA. Hence, to determine if the effects of 4-AP on the MPOs resulted from a non-selective blockade of K^+ channels, we repeated the experiments above in the presence of TEA (500 μM). As illustrated in **Figure 2.8**, application of TEA failed to mimic the 4-AP effect in either the presence or absence of simulated IPSPs. Moreover, concurrent application of forskolin (10 μM) and TEA also failed to unmask a significant increase in MPO amplitude over TEA alone (**Figure 2.8C**, n = 5), suggesting that the forskolin effect may only be observed when I_A channel activity is reduced by 4-AP.

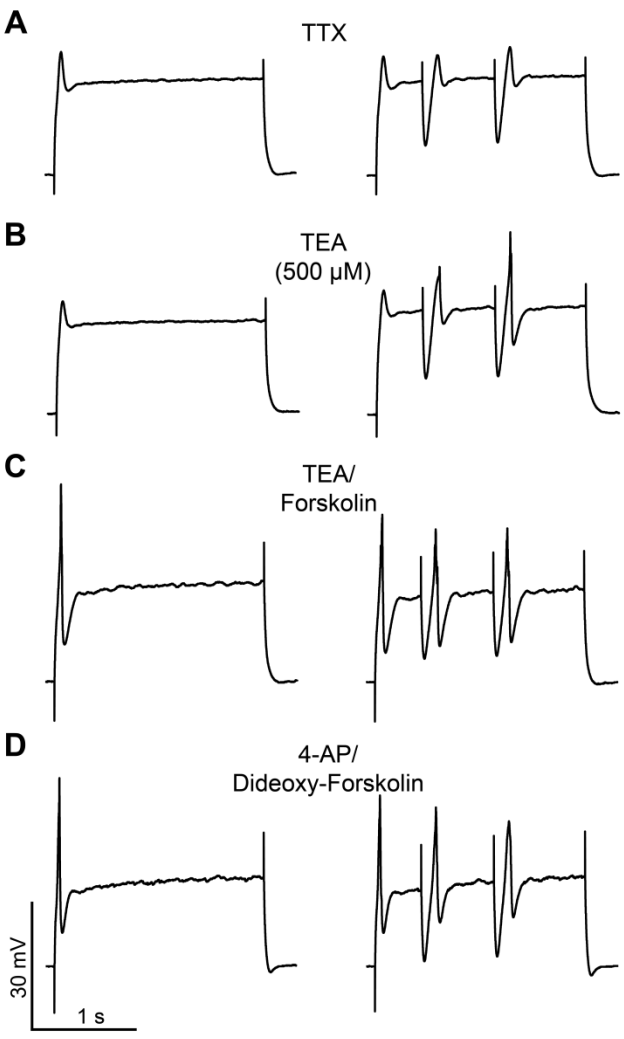

Figure 2.8: Forskolin and 4-AP modulation of the membrane potential oscillation were not mimicked by dideoxy-forskolin and TEA, respectively. *Intrinsic membrane oscillations of BLA principal neurons, held at -60 mV, in response to a steady depolarizing current injection with and without artificial IPSPs. (A) Shows typical small membrane oscillations in TTX during the depolarizing current injection. In the presence of 1 μM TTX, the introduction of IPSPs evoked a transient depolarizing deflection at the termination of each IPSP, but failed to unmask a MPO. (B) MPOs are not enhanced by application of TEA (500 μM). (C) The addition of 10 μM forskolin had a small enhancing effect on MPOs in the presence of TEA. (D) Application of the inactive isomer dideoxy-forskolin in the presence of 4-AP did not enhance the MPO as observed previously with forskolin*.

To verify that the effects of forskolin were mediated by direct activation of the adenylyl cyclase-cAMP signaling cascade, we then examined the membrane response to application of the inactive forskolin isomer, dideoxy-forskolin (10 μM), in the presence of 4-AP. Dideoxy-forskolin failed to mimic the forskolin effect on MPOs in either the presence or absence of artificial IPSPs, suggesting that activation of the adenylyl

cyclase-cAMP signaling cascade selectively facilitates IPSP-enhanced MPOs in principal neurons of the BLA (**Figure 2.8D**, n = 6).

Finally, we examined if modulation of intracellular Ca^{2+} levels also play a role in regulating the MPO. Here, inclusion of the Ca^{2+} chelator, BAPTA (5 mM), in the patch solution completely blocked the MPO induced by co-application of 4-AP (500µM) and forskolin (10µM) (**Figure 2.9A**, n = 6), suggesting that fluctuations in intracellular Ca^{2+} levels also play an important role in the expression of MPOs in BLA principal neurons. However, this result raised the possibility that the drug-induced MPO may be independent of activation of the cAMP-PKA signaling cascade. To address this question, we included the competitive antagonist of cAMP-induced PKA activation, cAMPs-RP, in the patch solution. Inclusion of cAMPs-RP (25 µM) completely blocked the MPO induced by forskolin (**Figure 2.9B**, n = 4). Conversely, inclusion of a non-hydrolysable cAMP analogue, 8-Br-cAMP (5-10 µM), in the patch pipette unmasked an MPO in the presence of TTX alone that was similar in magnitude to that induced by forskolin (**Figure 2.9C**, n = 6). Hence, Ca^{2+} influx through I_T channels, elevation of intracellular Ca^{2+}, and activation of the adenylyl cyclase-cAMP-PKA signaling cascade each play an important role in the expression of MPOs in BLA principal neurons.

The sensitivity of the MPO to modulation by intracellular Ca^{2+} and activation of the cAMP-PKA signaling cascade suggested that receptors coupled to $G_{\alpha s}$ would facilitate MPOs, whereas those coupled to $G_{\alpha i}$ would attenuate MPOs. To test this hypothesis, we examined the effect of prior application of the selective mGluR2/3 agonist, LY379268, on the 4-AP- and forskolin-induced MPOs. Principal neurons of the BLA express high levels of mGluR2/3 receptors (Rainni et al., 1994; Muly et al., 2007), which couple to $G_{i/o}$ proteins to inhibit adenylyl cyclase activity (Pin & Duvoisin, 1995), and we reasoned that activation of these receptors would attenuate drug-induced MPOs.

As illustrated in **Figure 2.9D** (n = 10), application of LY379268 (50 µM) completely blocked the MPOs.

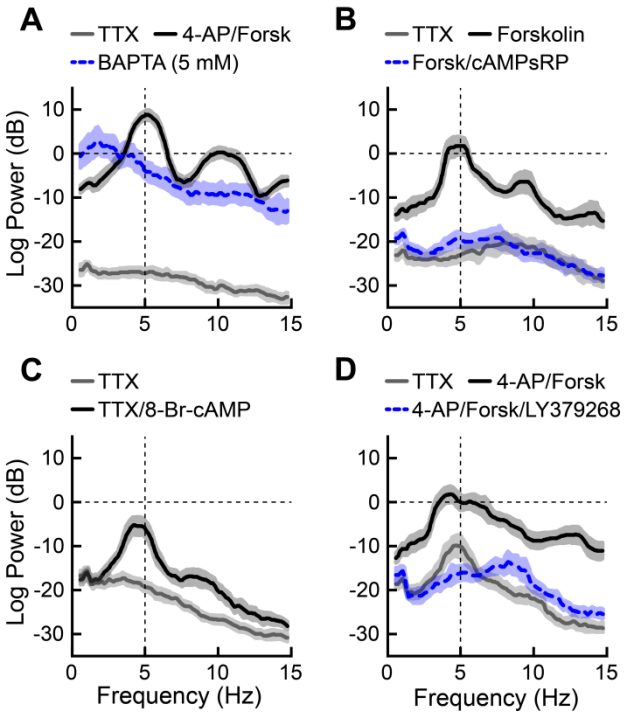

Figure 2.9: Membrane potential oscillations in the BLA were bi-directionally modulated by the adenylyl cyclase signaling cascade. *Cumulative power spectra of intrinsic theta frequency MPOs in BLA principal neurons. Responses are plotted as mean (solid lines) and 95% confidence intervals (shaded regions). Frequencies at which the 95% confidence intervals do not overlap indicate statistically significant differences among the plots. (A) BAPTA-containing patch solutions disorganized the frequency tuning of 4-AP- and forskolin-induced MPOs. (B) Inhibiting PKA activation completely abolishes forskolin-induced MPOs. (C) Activation of PKA with the cAMP analog 8Br-cAMP induces MPOs in TTX alone that are similar to those observed in response to forskolin. (D) Activation of mGluR II glutamate receptors with LY379268 completely blocked 4-AP and forskolin-induced theta MPOs.*

Discussion

In the present study, we demonstrate that spontaneous, compound IPSPs function to increase spike-timing precision both within and across BLA principal neurons. Previous studies have shown that these IPSPs are driven by local, burst-firing PV^+ neurons (Rainnie 1999), which have a high level of connectivity with BLA principal neurons. These data suggest that spontaneous, compound IPSPs would function to synchronize action potentials in a large population of principal neurons. We also show that compound IPSPs promote and entrain a high delta / low theta frequency membrane potential oscillation (MPO) that is uncovered by activation of the cAMP-PKA signaling cascade. The oscillatory nature of BLA principal neurons is also manifested as a modifiable inherent resonance frequency. We propose that the interaction of compound IPSPs with the oscillatory properties of BLA principal neurons is a viable mechanism for synchronizing firing activity in this cell population, promoting network oscillations within the BLA, and enhancing coherent oscillations between the BLA and other brain regions involved in fear.

Synchronized inhibition drives coordinated activity of BLA principal neurons

Recent evidence suggests a wide variety of behaviors require synchronized neural activity and network oscillations, both of which are promoted by synaptic inhibition (Soltesz & Deschenes, 1993; Person & Perkel, 2005; Sohal et al., 2006; Szücs et al., 2009; Pouille & Scanziani, 2001). Here, we demonstrate that BLA principal neurons receive highly synchronized, rhythmic inhibition which, in turn, synchronizes firing activity among groups of BLA principal neurons. Importantly, spontaneous activity of interneurons in the prefrontal cortex at theta frequency entrains the firing of principal neurons to an ongoing network theta oscillation (Benchenane et al., 2010). This example from the prefrontal cortex suggests the coordination of principal neuron firing by inhibition is critical for salient output of some neural circuits. Through coordinating the

firing of large groups of BLA principal neurons, compound IPSPs should improve salience by promoting summation of output and leading to spike-timing dependent plasticity in both the BLA and its targets.

In order to study the effect of compound IPSPs on spike-timing precision, we used two proxies: artificial IPSPs generated by direct current injection at the soma, and compound IPSPs evoked by direct stimulation of interneurons in the BLA under glutamatergic blockade. We showed that spike-timing precision within single neurons is improved by spontaneous IPSPs, artificial IPSPs, and stimulation-evoked IPSPs, with artificial IPSPs being significantly more effective than evoked IPSPs. Furthermore, artificial IPSPs were able to significantly coordinate firing across neurons, but evoked IPSPs were not, due to the observed variability in the waveform. Spontaneous, compound IPSPs observed across pairs had a highly consistent waveform (evident in a representative pair in **Figure 2.1A**), likely because they are generated by burst-firing PV^+ interneurons, which innervate BLA principal neurons perisomatically and have their activity coordinated through a syncytium. In contrast, stimulation of the BLA to evoke IPSPs probably recruited multiple subtypes of GABAergic interneurons targeting multiple compartments of the principal neurons (Mascagni & McDonald 2003; McDonald & Mascagni, 2002; McDonald & Betette, 2001) and hence introduced variability across cells in the IPSP waveform. While PV^+ interneurons seem uniquely positioned to generate synaptic inhibition that is ideal for interacting with an MPO and coordinating activity of BLA principal neurons, the possibility is not excluded that other inhibitory input, for instance feed-forward inhibition from cortical or thalamic sources (Rainnie et al., 1991a; Szinyei et al., 2000), could exert a similar coordinating influence.

The fact that artificial IPSPs were able to mimic the effects of evoked and spontaneous IPSPs on spike-timing precision without directly influencing the membrane conductance suggests they act primarily via membrane hyperpolarization. This

hyperpolarization likely causes activation of I_H and de-inactivation of voltage-gated currents including I_T, which would contribute to calcium spikes upon rebound (Hutcheon et al,. 1994). Because I_T is typically inactive near resting membrane potential, the observed effect of compound IPSPs on spike timing is probably more applicable when BLA principal neurons are depolarized from rest. It is also important to consider that compound IPSPs occur amidst ongoing synaptic activity, not in the absence of synaptic input as when tested here. In the *in vivo* system, compound IPSPs may not produce spikes in the absence of excitatory transmission, but rather interact with ongoing synaptic activity to influence the timing of spikes.

The ability of compound IPSPs to coordinate spiking activity most likely occurs across large groups of BLA principal neurons due to the broad connectivity of PV^+ interneurons (Muller et al., 2006), the synchronization of PV^+ interneuron firing activity through a syncytium (Muller et al., 2005; Woodruff & Sah 2007a,b), and, as shown here, the robustness of IPSP coordination of spike timing across principal neurons despite varying intrinsic properties. Although synchronizing large networks of principal neurons will improve potency of efferent signaling, it could also limit the specificity of signaling. Cortical inputs to the BLA are organized topographically (McDonald et al., 1999), and synchrony throughout the nucleus could weaken the specificity afforded by this topography. A loss of specificity in this circuit through excessive synchronization within the amygdala may lead to generalization of fear learning, which has been implicated in affective disorders such as post-traumatic stress disorder (Rainnie & Ressler, 2009). Furthermore, less than a quarter of BLA neurons appear to be incorporated into the engram for any specific fear memory (Han et al., 2007; Han et al., 2009). If encoding and recall of fear memories depend on network oscillations, there must be a mechanism to preferentially incorporate some neurons while excluding others. Some potential mechanisms include regulation of the extent of the syncytium or of projections from the

PV^+ interneurons onto principal neurons, or, more interestingly, interactions between variability in the frequency of the network oscillation with variations in preferred resonance frequency of the principal cells.

Considering the prominent role inhibition appears to play in coordinating the activity of BLA principal neurons, it is likely that stimuli altering the frequency of IPSPs *in vivo* could drastically change the output activity of the BLA. For instance, activation of serotonin 2A or cholecystokinin B receptors, both of which are implicated in emotional learning (Chhatwal et al., 2009), increase the frequency of rhythmic IPSPs in BLA principal neurons through indirect excitation of interneurons (Rainnie, 1999; Chung & Moore, 2007). A similar effect is observed in the BLA in response to local release of dopamine in mice (Loretan et al., 2004) and non-human primates (Muly et al., 2009). Moreover, the BLA receives dopaminergic input from the ventral tegmental area, which also exhibits a network oscillation at 2-5 Hz during working memory tasks (Fujisawa & Buzsáki, 2011), raising important questions about the nature of the interaction of phasic dopamine release with a BLA circuit that itself generates rhythmic activity.

Resonance frequency and intrinsic membrane oscillations in BLA principal neurons

In the present study we have shown that BLA principal neurons in the rat have an intrinsic resonance that was extremely consistent, with nearly all neurons displaying a peak resonance between 4.2 and 4.4 Hz. This intrinsic resonance was insensitive to application of TTX (1 µM), whereas a previous study in guinea pigs reported neurons in the lateral and basolateral nuclei of the amygdala express a TTX-sensitive inherent resonance frequency at 2.5 Hz (Pape & Driesang, 1998). The difference in reported resonance frequencies is likely due to the different model species, as we have also seen differences in peak resonance frequency of principal neurons between rat and primate (unpublished observation). The difference in TTX sensitivity, however, is likely explained

by the concentrations of TTX employed. In the study by Pape and colleagues the resonance frequency was abolished by 20 µM TTX, compared to the 1 µM TTX used here. High concentrations of TTX are known to block the persistent Na^+ current, and future studies should investigate whether it contributes to resonance in BLA principal neurons, as it does in LA neurons (Pape et al., 1998). Similar to our observations, hippocampal principal neurons also display resonance that is insensitive to 1 µM TTX with a peak at 4.1 Hz (Pike et al., 2000).

In addition to selectively filtering synaptic input in high delta / low theta bands, BLA principal neurons also express high- and low-threshold MPOs in this frequency range, as described by Pape and colleagues (Pape et al., 1998). Here we show the presence of an MPO that occurs at the peak resonance frequency of these neurons (~4-5 Hz) and seems to share some mechanisms with both previously described oscillations. Although Pape and colleagues found no effect of specific Ca^{2+} channel blockers on the high threshold membrane oscillations (Pape & Driesang, 1998), recordings with a BAPTA-containing electrode completely abolished the oscillation. In our hands, bath application of NiCl completely abolished the MPO, suggesting a strong influence of T-type Ca^{2+} channels. The Pape study also reported that high-threshold membrane oscillations were insensitive to 10 mM 4-AP, suggesting that voltage-gated K^+ channels were not involved in that membrane oscillation (Pape & Driesang, 1998). We observed, however, that application of 100-500 µM 4-AP significantly enhanced the membrane oscillations, suggesting I_A may actively suppress the MPO, acting in opposition to I_T. This could also be related to changes in input resistance, but the lack of effect of 500 µM TEA suggests a specific role of I_A. A similar relationship between I_T and I_A has been shown in other systems (Molineux et al., 2005; Pape et al., 2004), and factors that either enhance I_T or reduce I_A could then unmask the expression of the intrinsic membrane oscillations. In agreement with Pape and colleagues, we did not find an effect on

intrinsic membrane oscillations of blocking I_H with ZD7228 (60 μM, data not shown). While this is not an exhaustive pharmacological characterization, we believe we have identified the major currents involved in mediating this MPO. Other currents, including the persistent sodium current and calcium-activated potassium currents may also be involved (Pape & Driesang, 1998), and future study to illuminate their roles in this phenomenon would be valuable.

It is notable that the currents mentioned above (I_T, I_A, and I_H) are all sensitive to membrane hyperpolarization, particularly in the voltage range between rest and action potential threshold (Robinson & Siegelbaum, 2003; Perez-Reyes 2003; Rudy 1998). Specifically, I_T channels are de-inactivated by hyperpolarization in this range and I_H channels are activated, while I_A channels are activated by depolarization in this range. We have shown that compound IPSPs facilitate the MPO in the absence of spiking, and this is likely due to hyperpolarization-mediated de-inactivation of I_T and activation of I_H. While we did not find an effect of I_H blockade on the MPO, it is possible this is an artifact of the degree to which we depolarize the membrane to enhance the MPO. The MPO is likely also active in a more subtle form at membrane potentials only slightly depolarized from rest, where I_T and I_A are active and I_H would enhance the rebound from an IPSP and may contribute directly to the MPO.

In addition, the conductances of these currents, and therefore the magnitude of the MPO itself, are not fixed but sensitive to modulation. Importantly, the channels mediating I_T and I_H increase their activity in response to PKA phosphorylation (Kim et al., 2006; Kamp & Hell, 2000; Ramadan et al., 2009; Gerhardstein et al., 1999; Vargas & Lucero, 2002; Ingram & Williams, 1996). Conversely, activity of K^+ channels mediating I_A is decreased by PKA phosphorylation (Hoffman & Johnston, 1998). Together, these would enable neurotransmitter systems which modulate PKA activity to have synergistic effects to bi-directionally modulate the MPO.

The frequency of rhythmic, compound IPSPs is also sensitive to modulation. We have previously shown that dopamine acts to increase IPSP frequency into a range of 2-6 Hz (Rainnie 1999; Muly et al., 2009; Loretan et al., 2004). This would bring the IPSP frequency closer to the peak resonance frequency of BLA principal neurons, ensuring principal neurons respond to incoming rhythmic IPSPs with maximal voltage deflections and also serve to enhance the interaction with the MPO. In our hands, the oscillation does not occur spontaneously but is initiated by the IPSP and is naturally damped, quickly decaying from its initial amplitude. More frequent synchronized IPSPs would better reset drift in the phase relationship between cells and better maintain the amplitude of the oscillation.

It is interesting to note that the intracellular cascades activated by many of the neuromodulators that promote the MPO (e.g., G_s-coupled activation of cAMP and PKA) are also critical for synaptic plasticity. Through this mechanism, cells primed by neuromodulators to exhibit an MPO may be more likely to contribute to a fear memory engram.

Implications for learning and memory

Recent studies by several groups have emphasized the importance of amygdala network oscillations and synchronized oscillations across multiple brain regions in regulating long-term fear memory (Pape et al., 2005; Quirk et al., 1995; Collins et al., 2001; Paré et al., 2002; Seidenbecher et al., 2003; Pelletier & Paré, 2004; Bauer et al., 1997; Paz et al., 2008). Importantly, phase-locked stimulation of the amygdala and hippocampus at theta frequency during extinction training prolongs fear expression, suggesting synchronized network oscillations between these regions are an essential neurological component of fear memory (Lesting et al., 2011). The high delta / low theta oscillations in the LFPs of the BLA, hippocampus, and prefrontal cortex during fear acquisition and expression (Madsen & Rainnie, 2009; Sanga et al., 2009) match the

frequency of the MPO and the peak resonance in BLA neurons, suggesting the intrinsic properties of BLA neurons contribute to the network oscillation. As we have argued, a candidate mechanism to promote these network oscillations is the interaction of synchronized IPSPs with MPOs in BLA principal neurons. MPOs could contribute to fear learning by promoting network oscillations, and by improving spike-timing precision they could support fear memory formation through enhanced spike-timing dependent plasticity (Dan & Poo, 2004; Jutras & Buffalo, 2010).

The sub-cellular mechanism of the intrinsic MPO is well-suited to facilitate plasticity in the BLA and thereby promote fear learning. The MPO requires activation of voltage-gated calcium currents (Pape & Driesang, 1998), causing calcium influx and subsequent activation of cAMP and PKA (Zaccolo & Pozzan, 2003). This can, in turn, reinforce the oscillation through phosphorylation of ion channels. In fact, the oscillation is weak or nonexistent under our baseline experimental conditions, but must be uncovered by application of the PKA activator, forksolin. The close relationship of the MPO with the adenylyl cyclase-cAMP signaling cascade is particularly important because its downstream targets have been implicated in fear learning and memory (Schafe et al., 1999), and in regulating theta oscillations in the amygdala *in vivo* (Pape et al., 2005; Josselyn et al., 2001; Kida et al., 2002; Josselyn et al., 2004; Josselyn & Nguyen, 2005). It is also noteworthy that downstream targets of this signaling cascade, particularly the cAMP response element binding protein (CREB), have been used to identify those neurons activated specifically during fear memory formation (Han et al., 2007; Han et al., 2009).

One neurotransmitter receptor known to modulate the cAMP-PKA pathway, the dopamine D1 receptor, is also implicated in fear learning. Release of dopamine and subsequent activation of D1 receptors in the BLA are critically involved in the acquisition and consolidation of fear memory (Lamont & Kokkinidis, 2001; Greba et al., 2001).

Additionally, we have recently shown that D1-receptor activation is necessary for long-term potentiation of sensory afferents to the BLA (Li et al., 2011). Aside from direct effects on synaptic plasticity, D1 receptor activation may promote fear learning by facilitating an MPO. Considering that the MPO must be uncovered by activation of PKA *in vitro*, D1-receptor activation could provide the requisite PKA activation to initiate a self-reinforcing high delta / low theta oscillation *in vivo*. Importantly, in the prefrontal cortex, application of dopamine mimics the effect of a working memory task to entrain firing of principal neurons to an ongoing theta oscillation (Benchenane et al., 2010). One possible explanation, which parallels our observations in the BLA *in vitro*, is that interneurons maintain a network oscillation by providing a background of rhythmic activity to which principal neurons are, at baseline, minimally sensitive. In this model, the principal neurons become more sensitive to rhythmic inhibitory input from the interneurons by activation of PKA, either directly (as in our hands, with forskolin) or with the introduction of dopamine (either artificially or endogenously through a behavioral task) (Benchenane et al., 2010; Young, 2011). Interestingly, activation of D1 receptors has also been shown to enhance spike-timing dependent plasticity, potentially compounding with the effects of D1 activation on spike-timing precision via the MPO (Zhang et al., 2009).

We have shown that inhibition of adenylyl cyclase and cAMP production by activation of group II metabotropic glutamate receptors completely abolished the high amplitude MPO induced by forskolin and 4-AP. Activation of these receptors has been associated with reductions in fear learning, as well as de-potentation of synapses and long-term depression (Pin & Duvoisin, 1995; Lin et al., 2000; Lin et al., 2005), providing further support for a role for MPOs in BLA-dependent fear learning. Interestingly, the G_i-coupled type 1 cannabinoid receptor has been shown to reduce neural synchrony and dampen theta and gamma oscillations in the hippocampus (Robbe et al., 2006), further

suggesting changes in cAMP levels can bi-directionally modulate the propensity of a network to oscillate.

While network oscillations contribute to normal brain functions, including fear learning, aberrant oscillations have been implicated in the pathophysiology of psychiatric disorders. For example, it is well established that diminished synchrony between pyramidal neurons, and consequently aberrant network oscillations in the gamma band, are involved in the pathophysiology of schizophrenia (Lewis et al., 2005). Interestingly, the changes in oscillations observed in schizophrenia have been specifically linked to diminished function in the PV^+ subpopulation of interneurons in the cortex (Lewis et al., 2005; Powell et al., 2005). It is worth noting that theta oscillations are thought to modulate the gain of gamma oscillations, and both are produced through the action of PV^+ interneurons (Jensen & Colgin, 2007; Canolty et al., 2006; Bartos et al., 2007). Gamma-frequency oscillations are observed in the BLA both *in vivo* and *in vitro* (Sinfield & Collins, 2006; Tandall et al., 2011), and may be generated by similar mechanisms in the BLA as in the cortex due to their similar composition and architecture (Carlsen & Heimer, 1988). Considering the importance of neural oscillations and that compound IPSPs may influence gamma oscillations through their effects on high delta / low theta oscillations, future studies should address changes in oscillations and PV^+ interneurons in the amygdala in various psychiatric disorders, particularly post-traumatic stress disorder and others linked to fear learning (Rainnie & Ressler, 2009).

Furthermore, as discussed briefly in Chapter 1, many psychiatric disorders are increasingly understood to be developmental in origin. Considering the important functional role of membrane potential oscillations, as shown and discussed here, it is prudent to determine their developmental trajectory in order to identify critical periods in the development of oscillatory behavior and possible periods of susceptibility to perturbation. Currently, virtually nothing is known about the developmental trajectory of

oscillatory behavior in the BLA; in fact, very little is known about the development of any aspect of BLA physiology. In the following two chapters, we will map out the development of the physiology and morphology BLA principal neurons over the course of the first postnatal month. These studies will provide context for a final study exploring the development of spike timing precision and membrane potential oscillations in BLA principal neurons.

Chapter 3

Postnatal Development of Electrophysiological Properties of Principal Neurons in the Rat Basolateral Amygdala

Content presented in **Chapter 3** previously published as:
Postnatal development of electrophysiological properties of principal neurons in the rat basolateral amygdala. Ehrlich DE, **Ryan SJ**, Rainnie DG. *J Physiol*. 2012 Oct 1;590(Pt 19):4819-3

Abstract

The basolateral amygdala (BLA) is critically involved in the pathophysiology of psychiatric disorders, which often emerge during brain development. Several studies have characterized postnatal changes to the morphology and biochemistry of BLA neurons, and many more have identified sensitive periods of emotional maturation. However, it is impossible to determine how BLA development contributes to emotional development or the etiology of psychiatric disorders because no study has characterized the physiological maturation of BLA neurons. We addressed this critical knowledge gap for the first time using whole-cell patch clamp recording in rat BLA principal neurons to measure electrophysiological properties at postnatal day 7 (P7), P10, P14, P21, P28, and after P35. We show that intrinsic properties of these neurons undergo significant transitions before P21 and reach maturity around P28. Specifically, we observed significant reductions in input resistance and membrane time-constant of nearly ten- and four-fold, respectively, from P7 to P28. The frequency selectivity of these neurons to input also changed significantly, with peak resonance frequency increasing from 1.0 Hz at P7 to 5.7 Hz at P28. In the same period, maximal firing frequency significantly

increased and doublets and triplets of action potentials emerged. Concomitantly, individual action potentials became significantly faster, firing threshold hyperpolarized 6.7 mV, the medium AHP became faster and shallower, and a fast AHP emerged. These results demonstrate neurons of the BLA undergo vast change throughout postnatal development, and studies of emotional development and treatments for juvenile psychiatric disorders should consider the dynamic physiology of the immature BLA.

Introduction

The basolateral nucleus of the amygdala (BLA) is a major site of sensory input into the amygdala (McDonald, 1998), and activity in this region plays a critical role in regulating emotional behavior (Davis *et al.*, 2003; LeDoux, 2007; Pape & Pare, 2010). A growing body of evidence from basic and clinical research suggests that aberrant activity of the BLA also plays a major role in the etiology of several psychiatric and neurological disorders, including anxiety, depression, autism, and addiction (Adolphs *et al.*, 2002; Rainnie *et al.*, 2004; Shekhar *et al.*, 2005; Truitt *et al.*, 2007; Koob & Volkow, 2010). These disorders are commonly expressed early in life (Pine *et al.*, 1998; Kim-Cohen *et al.*, 2003; McEwen, 2003; Steinberg, 2005), and a wealth of evidence implicates adverse early-life experience as a predisposing factor for psychiatric illness and associated amygdala dysfunction later in life (Heim & Nemeroff, 2002; Zhang *et al.*, 2004; Kraszpulski *et al.*, 2006; Seidel *et al.*, 2008; Hicks *et al.*, 2009; Sadler *et al.*, 2011). The mechanisms by which early-life experiences impact the developing amygdala remain largely unknown because our understanding of amygdala physiology is based almost exclusively on research conducted in adult animals. Consequently, to better understand how early-life events can impact affective behavior later in life, a critical first step is to chart the normative developmental trajectory of the amygdala. Here we provide the first evidence for electrophysiological changes in the developing amygdala.

The few studies that have addressed other aspects of amygdala development reveal a highly dynamic neuronal environment in juvenile rodents, which does not begin to stabilize until at least postnatal day 28 (P28) (Morys *et al.*, 1998; Berdel & Morys, 2000; Brummelte *et al.*, 2007; Davila *et al.*, 2008). For example, the neuronal composition of the BLA is highly dynamic during the first postnatal month. Numerous in the BLA from birth, principal neurons account for about 85% of all neurons in the adult BLA (McDonald, 1985; McDonald *et al.*, 1989; Berdel *et al.*, 1997a). In contrast, interneurons expressing parvalbumin and/or calbindin, which comprise the majority of interneurons, first appear in the BLA around P14 and do not reach mature levels until about P25-30 (Berdel & Morys, 2000). In parallel with these changes, the number of synaptic contacts in the BLA nearly triples, while cell soma size doubles, and neuronal density halves between P7 and P14 (Berdel *et al.*, 1997a; Morys *et al.*, 1998). These changes are, in turn, mirrored by changes in thalamic and cortical inputs, which only emerge at P7 and are continually refined until P26 (Bouwmeester *et al*., 2002). Finally, the protein expression of key ion channels in BLA neurons changes on a similar time scale (Vacher *et al*., 2006).

We and others have shown that the normal function of the adult BLA is tightly regulated by a reciprocal interaction between principal neurons and GABAergic interneurons (Rainnie *et al.*, 1991a, b; Ehrlich *et al.*, 2009; Ryan *et al.*, 2012). Given the studies outlined above, the neural circuitry of the BLA, and hence its function, would be predicted to change dramatically across development. Consistent with this premise, at P7, rats approach an aversively-conditioned stimulus, only expressing the mature avoidance behavior after P10 (Sullivan *et al*., 2000). Similarly, adult-like expression of fear-potentiated startle does not emerge until P23 (Hunt *et al.*, 1994; Richardson *et al.*, 2000). Other aspects of conditioned fear, including the emergence of trace conditioning

and reinstatement, change on a similar time-scale (Campbell & Ampuero, 1985; Moye & Rudy, 1987; Kim & Richardson, 2007).

Despite the compelling evidence of early-life transitions in BLA function, no study to date has examined how changes in the physiological properties of individual BLA neurons contribute to these critical periods of development. This information is essential if we are to understand how the adult BLA becomes organized, how it comes to communicate with other brain regions, and how early-life perturbations could influence mature BLA function. We have begun to address this knowledge gap using whole-cell patch clamp recording to characterize the physiological development of BLA principal neurons during the first postnatal month. We show that these neurons undergo significant transitions in intrinsic properties which define their sensitivity to input and characteristic activity, including passive and oscillatory membrane properties, action potential waveform, and spike-train characteristics.

Methods

Ethical approval

All experimental protocols strictly conform to National Institutes of Health guidelines for the Care and Use of Laboratory Animals, and were approved by the Institutional Animal Care and Use Committee of Emory University.

Animals

Rats born in-house to time-mated Sprague-Dawley female rats (embryonic day 14 on arrival, Charles River, Wilmington, MA) were used in all experiments. Pups were housed with the dam prior to weaning on postnatal day 22 (P22) or P23 (considering P1 as day of birth). After weaning, rats were isolated by sex and housed 3-4 per cage with access to food and water *ad libitum*. Animals attributed to each recording day (P7, P10,

P14, P21, and P28) were recorded on that day or the following day (P7-8, P10-11, P14-15, P21-22, and P28-29, respectively).

Slice preparation

Slices containing the BLA were obtained as previously described (Rainnie, 1999). Briefly, animals were decapitated under isoflurane anesthesia (Fisher Scientific, Hanoverpark, IL, USA) if older than 11 days, and the brains rapidly removed and immersed in ice cold, 95/5% oxygen/carbon dioxide-perfused "cutting solution" with the following composition (in mM): NaCl (130), $NaHCO_3$ (30), KCl (3.50), KH_2PO4 (1.10), $MgCl_2$ (6.0), $CaCl_2$ (1.0), glucose (10), ascorbate (0.4), thiourea (0.8), sodium pyruvate (2.0), and kynurenic acid (2.0). Coronal slices containing the BLA were cut at a thickness of 300-350 μM using a Leica VTS-1000 vibratome (Leica Microsystems Inc., Bannockburn, IL, USA). Slices were kept in oxygenated cutting solution at 32 °C for 1 h before transferring to regular artificial cerebrospinal fluid (ACSF) containing (in mM): NaCl (130), $NaHCO_3$ (30), KCl (3.50), KH_2PO_4 (1.10), $MgCl_2$ (1.30), $CaCl_2$ (2.50), glucose (10), ascorbate (0.4), thiourea (0.8), sodium pyruvate (2.0).

Patch clamp recording

Individual slices were transferred to a recording chamber mounted on the fixed stage of a Leica DMLFS microscope (Leica Microsystems Inc., Bannockburn, IL, USA) and maintained fully submerged and continuously perfused with oxygenated 32 °C ACSF at a flow rate of 1–2 mL/min. The BLA was identified under 10x magnification. Individual BLA neurons were identified at 40x using differential interference contrast (DIC) optics and infrared (IR) illumination with an IR sensitive CCD camera (Orca ER, Hamamatsu, Tokyo Japan). A subset of neurons was filled using patch solution with added biocytin (0.3%) to confirm localization within the BLA. After some recordings, cytosol was recovered and screened using single-cell reverse-transcriptase PCR (as we described previously in Hazra *et al*., 2011) to confirm the presence of the glutamate

transporter, VGluT, which was seen in 58/60 neurons tested across all ages. Patch pipettes were pulled from borosilicate glass and had a resistance of 4–6 MΩ. Patch electrode solution had the following composition (in mM): K-gluconate (130), KCl (2), HEPES (10), $MgCl_2$ (3), K-ATP (2), Na-GTP (0.2), and phosphocreatine (5), titrated to pH 7.3 with KOH, and 290 mOsm. Data acquisition was performed using either a MultiClamp 700A or an Axopatch 1D amplifier in conjunction with pClamp 10.2 software and a DigiData 1322A AD/DA interface (Molecular Devices, Burlingame, CA, USA). Whole-cell patch clamp recordings were obtained and filtered at 2 kHz and digitized at 10 kHz. The membrane potential was held at −60 mV for all neurons if not specified. Cells were excluded if they did not meet the following criteria: a stable resting membrane potential more negative than −55 mV; access resistance lower than 30 MΩ; stable access resistance throughout recording, changing less than 15%; action potentials crossing 0 mV. Where indicated, Cs^+ (5 mM, Sigma Aldrich, St. Louis, MO) was administered through bath application.

Data Analysis

Data were analyzed by importing the raw voltage and current traces into Matlab (Mathworks, Natick, MA, USA) using scripts provided with sigTOOL (http://sigtool.sourceforge.net/, developed at King's College, London) and processed with customized scripts (available upon request). To characterize neurons in current clamp, first, a series of ten hyperpolarizing and depolarizing, 1 second long, square-wave current steps were injected. They were scaled so that, for each cell, the peak voltage deflections were to approximately -80 mV and -40 mV (amplitude of negative current injections ranged from a minimum of -20 pA at P7 to a maximum of -1000 pA at P28, and positive current injections from +16 pA at P7 to +800 pA at P28). Second, linear ramps of depolarizing current were injected, lasting 250 ms and scaled to

depolarize the neuron to -35 mV and elicit an action potential within the final 50 ms (peak current ranged from a minimum of +85 pA at P7 to a maximum of 555 pA at P28).

Membrane Properties and Intrinsic Currents

Input resistance and time constant were calculated using the deflection (approx. 5 mV) in response to the smallest, hyperpolarizing current step (minimum of -4 pA at P7, maximum of -200 pA at P28). Time constant was defined as the time necessary for the cell to reach 63.2% of its maximal deflection; input resistance was calculated as the ratio of peak voltage deflection to the current injected. To measure the hyperpolarization-activated, non-specific cation current, I_h, neurons were voltage clamped at a holding potential of -60 mV and stepped to -100 mV for 600 ms in the presence of 1 µM TTX. The waveform of the I_h current was generated by subtracting a current trace measured in the presence of bath-applied, 5mM Cs^+, known to block I_h, from that measured in its absence. This subtraction current was used to measure amplitude and activation time constants of I_h. A two-term exponential fit (eq. 3.1, k = 1) was used to extract fast and slow time constants of I_h activation, except at P7, where two terms over-parameterized the fit and a one-term exponential (eq. 1, k = 2) was used instead.

Equation 3.1 $$f(t) = \sum_{i=1}^{k} A_i \times e^{-t/\tau_i} + C$$

Action Potentials and Spike Trains

Action potentials were detected using a heuristic to locate peaks in the second derivative of the membrane potential waveform. The time of the peak was assigned to be the time of spike initiation and the voltage assigned as action potential threshold, which correlated well with visual inspection of the data. Since the smapling rate used here was not fast compared to the frequency of the action potential waveform (10 kHz compared to ~1kHz), linear interpolation between data points was used to enhance the temporal resolution of measurements of 10-90% rise time, 90-10% decay time, and half-

maximal width. Data on spike trains were collected from responses to the depolarizing, 1 second-long, square-wave current injections described above. Spike trains were included in the analysis if the mean of their inter-spike membrane potential fell within one standard deviation of the spike threshold measured for each age. Inter-spike intervals (ISIs) were calculated using the times for spike initiation in these traces, and the instantaneous firing frequency of the spike train was calculated as the reciprocal of these ISIs.

Resonance and Oscillations

Resonance was assessed by injecting neurons with a ZAP current, a sinusoidal current of fixed amplitude that sweeps logarithmically from 0.1 to 12 Hz over 30 seconds. The amplitude of the current was adjusted to elicit a 20 mV maximal depolarization from a baseline potential of -70 mV. Impedance was calculated as a function of input frequency for each neuron by deriving a power spectrum for the voltage response to the ZAP current, using fast Fourier transforms in the Chronux toolbox for Matlab (Bokil *et al.,* 2010), and normalizing it to the power spectrum of the injected current. In order to extract peak values from noisy power spectra and generate averages, the raw impedance traces were fit with a 6^{th} order polynomial. Prominence was calculated using power spectra as the proportion of total power in the entire range considered (1-10Hz) found in a given frequency band (1-2, 2-4, 4-6, 6-8, or 8-10 Hz). The change in prominence due to Cs^+ application was calculated as a ratio of the power in a given frequency band in Cs^+ and TTX to that in TTX alone. Correlation analysis of the relationship between membrane time constant (τ_{memb}) and peak resonance frequency was performed using GraphPad Prism 4 (GraphPad Software Inc., La Jolla, CA, USA). The presence of membrane potential oscillations (MPOs) in recordings of neurons gradually depolarized to action potential threshold was assessed by an observer blinded to age group. Spike-triggered averages of these depolarized traces were generated

using Matlab to observe phase relationships between action potentials and putative MPOs.

Statistics

Data points greater than 2 standard deviations from the mean were deemed outliers and removed from statistical analysis. All data sets were tested for normality using the Shapiro-Wilk test ($\alpha = 0.05$) and for homoscedasticity using Levene's test ($\alpha = 0.0001$), implemented in Matlab. Data sets for mAHP and fAHP amplitude, maximal firing rate, peak resonance frequency, and Ih amplitude passed the Shapiro-Wilk and Levene's tests, so one-way ANOVA with Tukey's post-hoc tests ($\alpha = 0.05$) were used to assess significance. To account for age-dependent changes in variance, values of Rin, тmemb, and action potential rise- and decay-times were log-transformed before statistical analysis. Because the data sets for 6 of 7 basic electrophysiological parameters (Rin, тmemb, action potential half-width, rise-time, decay-time, and first inter-spike interval, but not action potential threshold) failed either the Shapiro-Wilk or Levene's test, all of these data sets were analyzed using the Kruskal-Wallis test for overall effect of age on each parameter ($\alpha = 0.05$). The Kruskal-Wallis test was also used for mAHP and fAHP times-to-peak. When a main effect was found, pair-wise comparisons were made for each age group with two nearest older and younger groups (i.e. P21 vs. P10, 14, 28, and >35) using Wilcoxon rank sum tests (Matlab) with a Bonferroni correction for the resulting 9 comparisons ($\alpha = 0.0056$). Significant changes in prominence were assessed using a two-way, repeated measures ANOVA with Bonferroni post-hoc tests, with frequency band as a within-subjects factor and age as a between-subjects factor. Peak resonance frequency was exponentially correlated with τ_{memb} using a least-squares method with eq. 1 ($k = 1$) in GraphPad for all data from P14, P21, and P28.

An analysis of the effects of sex on physiological maturation was performed using a two-way ANOVA with factors of sex and age for the following parameters using GraphPad: R_{in}, τ_{memb}, action potential threshold, half-width, rise-time, decay-time, and first inter-spike interval. Significance was assessed for a main effect of sex in each parameter ($\alpha = 0.05$). This analysis included 16 male and female neurons from 5 male and 3 female rats at P14, 12 male and female neurons from 3 male and 2 female rats at P21, and 12 male and 8 female neurons from 4 male and 2 female rats at P28. No neurons were included from P7 or P10 due to difficulty assessing sex in the young rats. A posthoc power analysis for the effect of sex was conducted using *G*Power* (Erdfelder *et al*., 1996) with $\alpha = 0.05$.

Results

Data were collected from a total of 499 BLA neurons from 93 rats on postnatal day 7 (P7), P10, P14, P21, and P28. Also included were data from 53 neurons from 26 older animals (P>35) for comparison with the preadolescent data. To make gross comparisons of neural properties across development, we first examined the voltage response of patch clamped principal neurons to transient (1s) hyperpolarizing and depolarizing current injections at P7, P14, P21, and P28. As illustrated in **Figure 3.1,** BLA principal neurons at each developmental time-point had distinct voltage responses to DC current injection. The most obvious changes were to input resistance (R_{in}), membrane time-constant (τ_{memb}), the depolarizing voltage sag upon membrane potential hyperpolarization likely caused by I_h, and the pattern of action potentials. Below we quantify these and many other physiological changes to BLA principal neurons across the first postnatal month.

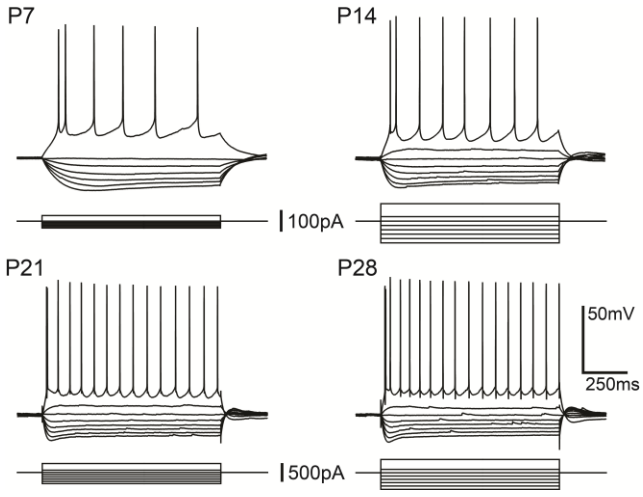

***Figure 3.1**: **Maturation of physiological properties of BLA principal neurons across the first postnatal month.** Illustrated are representative voltage responses to a series of transient (1 s) hyperpolarizing and depolarizing current steps, depicting age-dependent changes in the active and passive membrane properties of BLA principal neurons. All neurons were held at -60 mV with direct current injection. The amplitudes of current injection were adjusted for each neuron to normalize the voltage deflections. Note the difference in scale for the current injections of the neurons depicted in the top panel (postnatal day 7 (P7, left) and 14 (right)) and those depicted in the bottom panel (P21 (left) and 28 (right)).*

Postnatal Maturation of Passive Membrane Properties

We measured the passive electrical properties of principal neurons at all time-points when manually held at -60 mV with DC current injection. Here, R_{in} and τ_{memb} were estimated from small, <5 mV hyperpolarizing voltage deflections elicited by transient current injection. We observed a significant reduction in R_{in} of nearly ten-fold across the first postnatal month (**Figure 3.2A;** $p < 0.001$, Kruskal-Wallis, $\chi^2_5 = 241.8$), with the greatest changes occurring before P21. There was a more than two-fold reduction in R_{in} from P7 to P14, and a nearly three-fold reduction from P14 to P21. Specifically, R_{in} decreased significantly from a median value of 523.7 MΩ at P7 (n = 45) to 374.8 MΩ at P10 (n = 37), 238.4 MΩ at P14 (n = 54), 88.0 MΩ at P21 (n = 43), and 55.9 MΩ at P28 (n = 58; Wilcoxon rank sum post-hoc tests). By P28, R_{in} had achieved its mature value

and was not significantly different ($p > 0.05$) from neurons aged >P35 (52.67 MΩ, n = 56). Membrane time-constant followed a similar developmental trajectory to R_{in} (**Figure 3.2B, C**), with a nearly four-fold reduction from P7 to P28. Overall there was a significant effect of age (Kruskal-Wallis, $\chi^2_5 = 221.4$), with a nearly two-fold reduction from P7 to P14 and another two-fold decrease from P14 to P28. Whereas the change from P7 to P10 was not significant ($p > 0.05$, Wilcoxon rank sum post-hoc tests; median = 59.1 ms at P7, n = 45; 50.5 ms at P10, n = 39), there was a significant ($p < 0.001$) decrease from P10 to P14 (32.0 ms, n = 53), P14 to P21 (18.0 ms, n = 45), and P21 to P28 (15.1 ms, n = 56). Similar to R_{in}, τ_{memb} reached its mature value by P28 and did not change significantly between P28 and >P35 (15.1 ms, n = 54; $p > 0.05$). Having observed significant age-dependent changes in the passive membrane properties of BLA principal neurons, we next examined concomitant changes in active properties, beginning with the voltage-gated current, I_h.

Postnatal Maturation of Intrinsic Currents

Development of the Voltage-Gated Current, I_h

One current which classically contributes to passive membrane properties like R_{in} and τ_{memb} is the hyperpolarization-activated cation current, I_h. This current mediates a depolarizing voltage sag observed in response to hyperpolarization from rest that is readily apparent at all ages (**Figure 3.1**). When neurons were manually held at -60 mV and the amplitude of the transient hyperpolarizing current steps adjusted to elicit peak voltage deflections to -80 mV, the depolarizing sags observed in the voltage response had a similar amplitude at all time-points (**Figure 3.3A**); however, the rate of onset of the sag increased with age. Significantly, the voltage sag was abolished at all ages by bath application of 5 mM Cs^+, suggesting it is likely mediated by activation of I_h. An example of the Cs^+ blockade of the depolarizing sag at P28 is illustrated in **Figure 3.3A**, upper

trace. Considering the differences in R_{in} across ages and the visible differences in the kinetics of the voltage sag, we next quantified the maturation of I_h in voltage clamp.

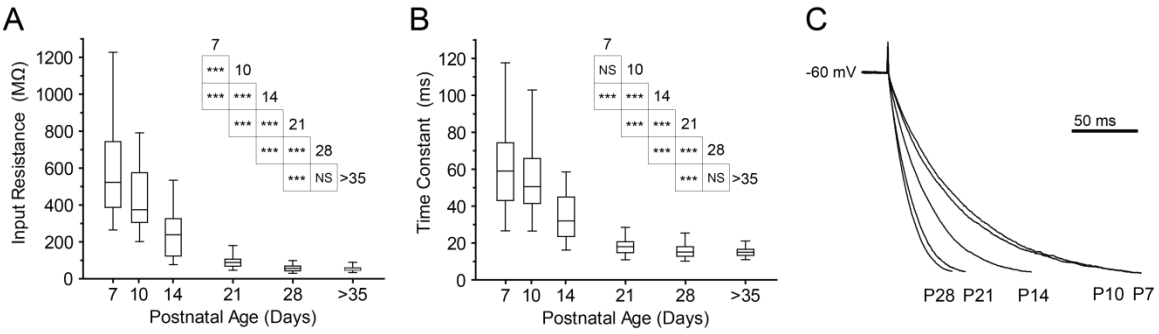

Figure 3.2**: **Input resistance and membrane time constant decrease with age.** (A, B) Box and whisker plots show input resistance (A) and membrane time-constant (B) of BLA principal neurons across the first postnatal month and in adulthood (n = 45 (P7), 37-39 (P10), 53-54 (P14), 43-45 (P21), 56-58 (P28), and 54-56 (P>35)). Significance was assessed using a Wilcoxon rank-sum test and pairwise comparisons were made for each age group with up to four neighboring time-points (see inset tables for results) using a Bonferroni correction for the resulting 9 comparisons (, $p < 0.001$; NS: not significant, $p > 0.05$). (C) Maturation of membrane time-constant is illustrated with the average, normalized membrane charging in response to a small, hyperpolarizing current step (approximately 5 mV deflection) for each developmental time point (n = 48 (P7), 28 (P10), 56 (P14), 45 (P21), and 58 (P28)).*

To quantify the amplitude and kinetics of I_h activation, the membrane potential was stepped from -60 to -100 mV, both before and after application of 5 mM Cs^+, and the resulting currents were then subtracted to isolate I_h. The mean isolated I_h for each time-point is illustrated in **Figure 3.3B**. Analysis of the peak amplitude revealed a steady increase of I_h amplitude across the entire first postnatal month (**Figure 3.3C**), such that the mean I_h amplitude was 91.5 ± 28.1 pA at P7 (n = 10), 359.8 ± 82.3 pA at

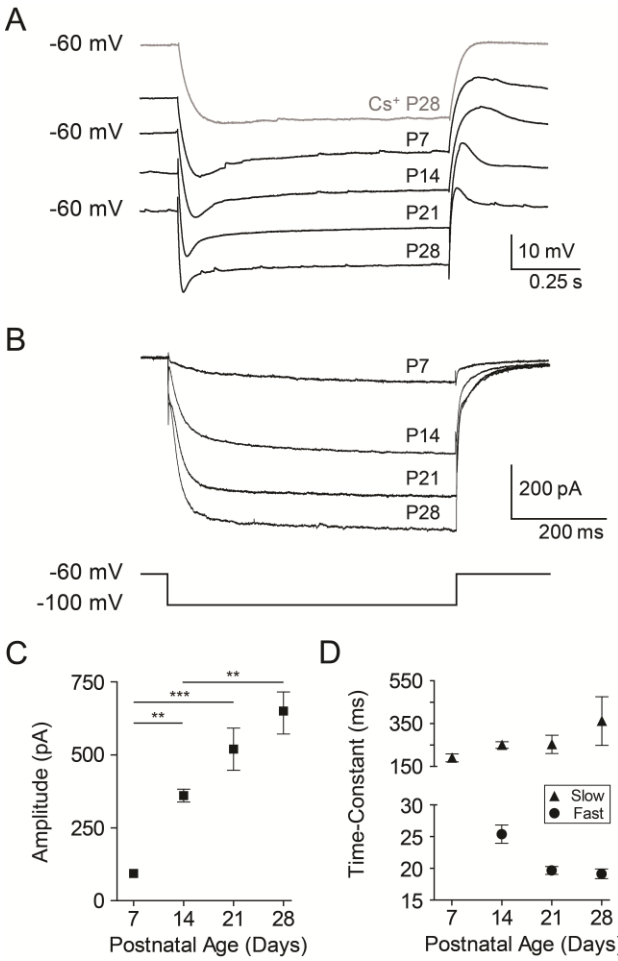

***Figure 3.3*: Developmental increase in Ih amplitude and kinetics in BLA principal neurons.** *(A) Representative voltage responses of neurons to a hyperpolarizing, square step of magnitude adjusted to elicit a 20 mV peak deflection. Neurons were recorded in the presence of 1 μM TTX at each time point, and blockade of Ih by 5 mM cesium (Cs+) is depicted for a neuron at P28. Neurons had baseline membrane potential adjusted to -60 mV with direct current. (B) Voltage-clamp recordings following cesium application (5 mM) subtracted from those prior to cesium application depict the maturation of a Cs+-sensitive current. Neurons were held at -60 mV and stepped to -100 mV, and all recordings were performed in the presence of 1 μM TTX (n = 10 (P7), 14 (P14), 11 (P21), 11 (P28)). (C) Peak amplitudes of subtraction currents from B are plotted as mean ± SEM for each time point. Significance was assessed using a one-way ANOVA with Bonferonni's post-tests, and pairwise comparisons were made for each age group with up to three neighboring time-points (see inset table for results; ***, $p < 0.001$; **, $p < 0.01$; NS: not significant, $p > 0.05$). (D) Plotted as mean ± SEM for each age, the time constant of Ih activation was measured from a double exponential fit to the subtraction currents in B at all ages except P7, which was sufficiently fit with a single exponential.*

P14 (n = 14), 518.1 ± 239.2 pA at P21 (n = 11), and 641.9 ± 239.8 pA at P28 (n = 11). Notably, significant transitions occurred from P7 to P14 and from P14 to P28 ($p < 0.01$, One-way ANOVA with Tukey's post-hoc, $F_{3,42} = 19.93$). The activation kinetics of I_h were estimated by fitting its charging curve with a two-term exponential equation, except at P7, when the curve was sufficiently parameterized with a one-term exponential. The fast time constant decreased from 25.4 ± 6.3 ms at P14 (n = 19) to 19.6 ± 2.4 ms at P21 (n = 15), but remained steady between P21 and P28 (19.1 ± 2.7 ms, n = 13; **Figure 3.3D**, black squares). The single time constant at P7 was 188.5 ± 61.1ms (n = 11), which was similar to the slow time constant of activation for the other ages (253.5 ± 65.2 at P14, 252.9 ± 127.7 at P21, and 361.7 ± 340 at P28; **Figure 3.3D**, black triangles).

Development of Intrinsic Resonance

Membrane properties like τ_{memb} and active currents like I_h help shape intrinsic resonance, which acts as a band-pass filter to enhance responsiveness to synaptic input at particular frequencies. BLA principal neurons in the adult rat, guinea pig, and non-human primate exhibit a preferred resonance frequency between 2.5 and 6 Hz (Pape & Driesang, 1998; Ryan *et al.*, 2012). Resonance properties of neurons likely contribute to the production of network oscillations (Lampl & Yarom, 1997; Desmaisons *et al.*, 1999; Richardson *et al.*, 2003; Tohidi & Nadim, 2009), and recent evidence suggests that network oscillations in the BLA at the frequency of principal neuron resonance are intimately related to fear memory formation and expression (Popa *et al.*, 2010; Lesting *et al.*, 2011). Considering the potential contribution of BLA principal neuron resonance to the generation of fear expression and learning, we next examined the ontogeny of resonance properties in these neurons.

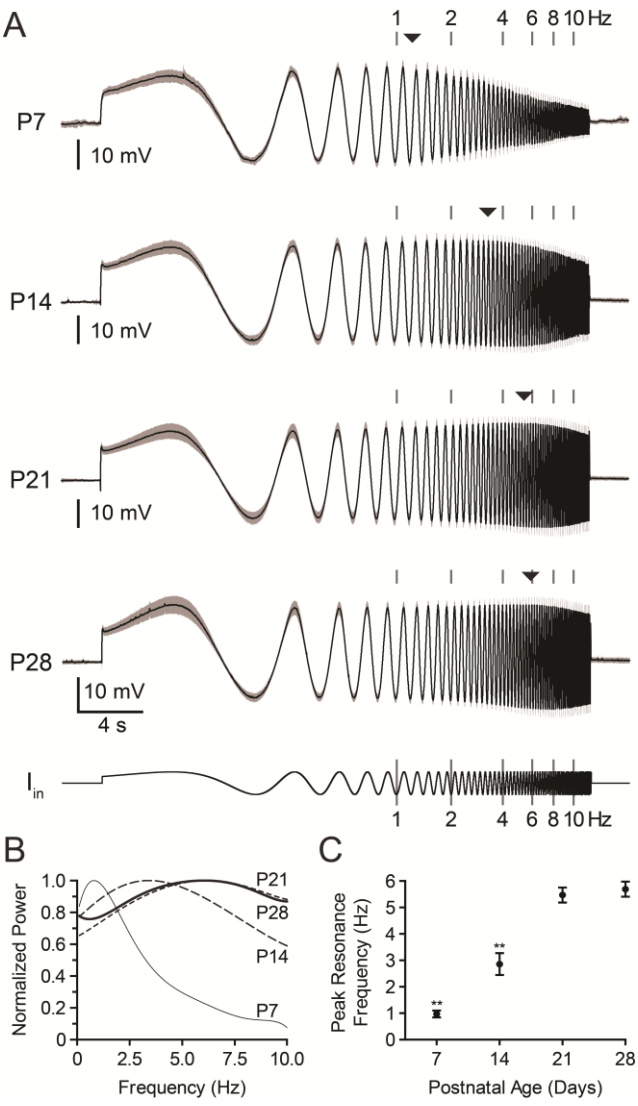

***Figure 3.4*: Maturation of intrinsic resonance towards higher frequencies.** *(A) Membrane potential response, shown as mean (black line) and standard deviation (grey band), to a ZAP current (Iin, fixed amplitude and logarithmically increasing frequency, shown at bottom) is depicted for each age (n = 22 (P7), 24 (P14), 22 (P21), and 32 (P28)). Neurons were first hyperpolarized to -70 mV with direct current, and ZAP current amplitude was adjusted for each neuron to elicit a 20 mV depolarizing deflection. Instantaneous frequency of the injected current is highlighted with gray bars above each trace, and the mean, peak resonance frequency for each age is depicted amid the gray bars with a black triangle. (B) Relative impedance for input from 0.1-10 Hz, calculated by normalizing the power spectra of the voltage responses in A to the power spectra of injected current, were fit with polynomials and plotted as the mean (n consistent with A). (C) Peak resonance frequency is plotted as mean ± SEM, measured at the maximum of each neuron's individual power spectrum (n = 21 at P7, 24 at P14, 21 at P21, and 29 at P28). Statistical significance was assessed with a one-way ANOVA using Bonferroni's post-tests to compare all data sets (** denotes p < 0.001 versus all other groups).*

By injecting a sinusoidal ZAP current of increasing frequency (see Methods) we were able to determine the peak resonance frequency, the input frequency that elicits the greatest membrane deflection, of BLA principal neurons across development. As illustrated in **Figure 3.4A,** the population responses to ZAP currents at P7, P14, P21, and P28 clearly showed a shift in the resonance frequency of principal neurons, with more mature neurons showing higher resonance frequencies. By taking the ratio of power spectra for output voltage and ZAP input current, we generated functions of impedance vs. input frequency (**Figure 3.4B**). Here, the peak resonance frequency increased sharply and significantly until P21 ($p < 0.001$, One-Way ANOVA with Tukey's post-tests, $F_{3,91} = 74.31$), with values (mean ± SD) of 0.97 ± 0.33 Hz at P7 (n = 21), 2.63 ± 1.48 Hz at P14 (n = 24), 5.47 ± 1.30 Hz at P21 (n = 21), and 5.69 ± 1.49 Hz at P28 (n = 29; **Figure 3.4C**).

To determine how developmental changes in I_h may contribute to the maturation of resonance, we blocked I_h using Cs^+ and measured changes in the responses to ZAP currents across the first postnatal month (**Figure 3.5A**). At all ages, Cs^+ application reduced the peak resonance frequency to below 1 Hz (0.60 ± 0.09 Hz at P7 (n = 8), 0.67 ± 0.22 Hz at P14 (n = 9), 0.85 ± 0.29 Hz at P21 (n = 8), and 0.94 ± 0.49 Hz at P28 (n = 11)). However, the effect of Cs^+ blockade on resonance involves more than a change in peak frequency; therefore, to highlight differences in the contribution of I_h to resonance across ages, we quantified the effect of Cs^+ on prominence, the proportion of total power between 1 and 10 Hz found in a given frequency band (1-2, 2-4, 4-6, 6-8, or 8-10 Hz) (Burton *et al*., 2008).

As shown in **Figure 3.5B**, the change in prominence due to Cs^+ application varied by age as an inverted 'U' with Cs^+ having relatively little impact at P7 and causing robust changes at P14, then having a progressively weaker effect at later time-points. There were significant main effects on change in prominence of frequency band ($F_{4,272} =$

518.1, p < 0.0001, Two-way ANOVA with repeated measures) and age ($F_{3,272}$ = 28.9, p < 0.0001), as well as a significant

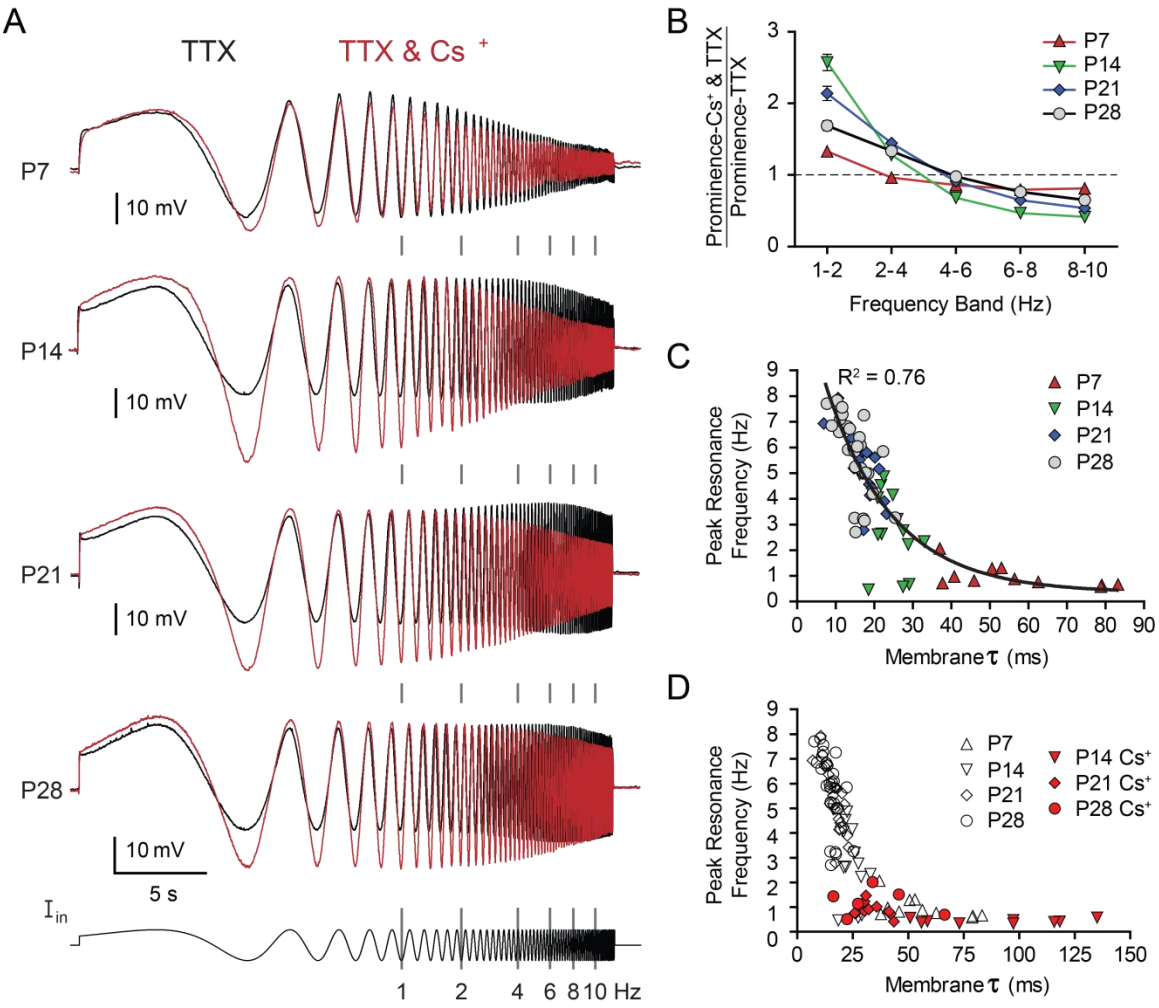

***Figure 3.5**: **Contribution of Ih to intrinsic resonance of BLA principal neurons changes with age**. (A) Mean membrane potential response to a ZAP current (Iin, fixed amplitude and logarithmically increasing frequency, shown at bottom) in 1 μM TTX alone (black line, taken from Figure 3.6) or with 5 mM Cs+ (red line) is depicted for each age (in Cs+, n = 19 at P7, 21 at P14, 20 at P21, and 17 at P28). Neurons were first hyperpolarized to -70 mV with direct current, and ZAP current amplitude was adjusted for each neuron and condition to elicit a 20 mV, maximal depolarizing deflection.*

Instantaneous frequency of the injected current is highlighted with gray bars between traces. (B) Effect of Cs+ application on prominence, calculated as ratio of the prominence before and after Cs+ application, plotted as mean & SEM at P7, P14, P21, and P28. (C, D) Peak resonance frequency is plotted against membrane time constant (τ) for neurons at each time point, recorded in TTX alone (C, D) or following application of 5 mM Cs+ (D). A black line depicts the results of an exponential regression (R2 = 0.76) of the data shown in C.

interaction effect ($F_{12,272}$ = 40.9, $p < 0.0001$). Specifically, at P7 Cs^+ increased prominence (mean ± SD) at 1-2 Hz by 32.9 ± 20.1% and reduced prominence in the higher bands by between 1 and 3% each (n = 18). Compared to at P7, Cs^+ application at P14 caused a significantly greater increase in prominence in the 1-2 and 2-4 Hz bands (+157.3 ± 49.4% and +28.2 ± 12.6 % respectively; $p < 0.001$, Bonferroni post-hoc tests), and a significantly greater reduction in the 4-6, 6-8, and 8-10 Hz bands (-31.8 ± 7.5%, -53.0 ± 9.0%, and -58.3 ± 7.6%, respectively; n = 19; $p < 0.01$). The effect of Cs^+ at P21 was significantly weaker than at P14 ($p < 0.001$) in the 1-2, 4-6, and 6-8 Hz bands and significantly greater ($p < 0.01$) in the 2-4 Hz band (+113.9 ± 43.1% at 1-2 Hz, +44.6 ± 16.3% at 2-4 Hz, -9.5 ± 6.7% at 4-6 Hz, -35.0 ± 9.3% at 6-8 Hz, and -46.5 ± 11.5% at 8-10 Hz; n = 19). The trend continued at P28, with Cs^+ having a weaker effect than at P21. Specifically, Cs^+ caused a significantly smaller increase in prominence in the 1-2 Hz band ($p < 0.001$; +68.9 ± 27.4%) but effects in the remaining bands were not significantly different than at P21 (+33.4 ± 13.5% at 2-4 Hz, -2.2 ± 4.3% at 4-6 Hz, -23.7 ± 8.9% at 6-8 Hz, and -34.8 ± 11.8% at 8-10 Hz; n = 16).

The effects of Cs^+ on resonance were largely attributable to a direct effect on τ_{memb}. In control conditions, peak resonance frequency was correlated with τ_{memb} using a standard exponential equation (see Methods), yielding a R^2 value of 0.76 with A_1 =

12.42, τ_1 = 17.24, and C = 0.28 (**Figure 3.5C**). Application of Cs^+ increased τ_{memb} at P14, P21, and P28 by an average of 67.0, 19.0, and 24.5 ms, respectively, causing a corresponding reduction in peak resonance frequency at each age (**Figure 3.5D**). Based on these observed changes to oscillatory properties of BLA principal neurons, we next characterized the maturation of spontaneous expression of membrane oscillations.

Development of Spontaneous Membrane Potential Oscillations

The oscillatory properties of adult BLA principal neurons manifest not only as resonance, but also as spontaneous membrane potential oscillations (MPO; (Pape *et al.*, 1998; Ryan *et al.*, 2012)). These MPOs can influence spike-timing and interact with resonance to filter synaptic input based on frequency (Desmaisons *et al.*, 1999; Izhikevich, 2002; Sancristobal *et al.*, 2010). Furthermore, we have recently shown that phase-locked MPOs and coordinated spiking in adult BLA principal neurons are promoted by spontaneous, synchronous inhibitory postsynaptic potentials, highlighting a mechanism by which MPOs could contribute to network oscillations in the BLA (Ryan *et al*., 2012). We were therefore interested in the ontogeny of network oscillations in the BLA, and next examined the expression of MPOs in neurons at P7, 14, 21, and 28. Here, principal neurons were depolarized to action potential threshold with DC current injection. As illustrated in **Figure 3.6A**, neurons at P7 were more likely to fire action potentials in bursts, whereas P28 neurons had a more stable membrane potential and fired sporadically (**Figure 3.6A**). When depolarized to threshold, neurons also became more likely to exhibit spontaneous MPOs across the first postnatal month (**Figure 3.6B, C**). A blinded, qualitative analysis of current-clamp recordings near threshold revealed that only 5% of BLA principal neurons exhibited spontaneous MPOs at P7 (n = 20) and P10 (n = 19), but MPOs were present in 23% of neurons at P14 (n = 26), 64% at P21 (n = 25), and 60% at P28 (n = 48). Moreover, when we measured the frequency of spontaneous MPOs for neurons with a discernible peak in the power spectrum of their

activity during a low-spiking period at threshold, we observed that it increased with development (3.8 ± 1.0 Hz at P14, n = 3; 3.7 ± 1.9 Hz at P21, n = 12; 4.4 ± 1.9 Hz at P28, n = 22). In other brain regions, MPOs are capable of organizing action potential timing (Llinas *et al.*, 1991; Gutfreund *et al.*, 1995; Desmaisons *et al.*, 1999), and the same appears to be true in the BLA. An example of this is illustrated in **Figure 3.6D,** which shows a spike-triggered average from a P28 neuron.

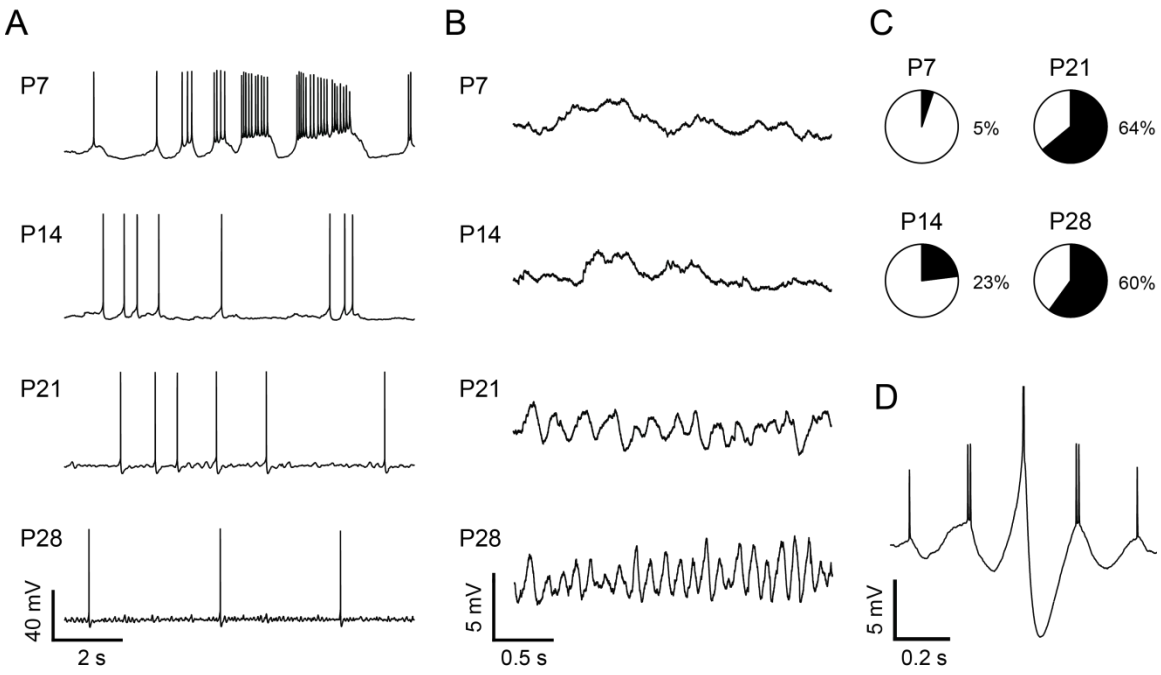

***Figure 3.6**: **Spontaneous membrane potential oscillations emerge as BLA principal neurons develop.** (A, B) Representative current-clamp recordings, shown at two scales, of neurons depolarized to action potential threshold with direct current, highlighting maturation of spiking pattern (A) and spontaneous membrane potential oscillations (B). (C) Pie charts depict the proportion of neurons expressing spontaneous membrane potential oscillations at each time-point (n = 20 (P7), 26 (P14), 25 (P21), and 48 (P28)). (D) Representative spike-triggered average from a 30 s recording of a P28*

neuron held near threshold, displaying entrainment of spiking to a spontaneous membrane potential oscillation.

Postnatal Maturation of Spiking

Development of Spike Trains

Having observed significant developmental changes in the sensitivity of BLA principal neurons to input as well as gross changes in action potential output (see **Figures 1** and **6A**), we next quantified the maturation of action potential trains across the first postnatal month. Here, spike trains were elicited with a transient, 1s, square-wave depolarizing current injection to action potential threshold. As illustrated in **Figure 3.7** (inset), there was a gradual emergence across the first postnatal month of doublet and triplet firing at the onsets of the spike trains. Moreover, analysis of the instantaneous firing rates based on the first 6 inter-spike-intervals (ISIs) for principal neurons at P7, 14, 21, and 28 revealed that at P7 the firing rate was relatively consistent across the entire train, starting at 29.7 ± 13.3 Hz and stabilizing at 16.8 ± 8.1 Hz by the third interval (**Figure 3.7A**). By P14, doublets became more apparent with an initial firing rate of 62.2 ± 52.1 Hz that dropped to 17.3 ± 12.5 Hz by the second interval. At P21, the doublet became faster and a triplet emerged in some neurons, with firing rates of 138.8 ± 77.9 and 45.0 ± 44.5 Hz for the first and second intervals, respectively, which stabilized around 20 Hz for the remainder of the train. Firing at P28 was very similar to that at P21, with slightly faster rates for the first pair of spikes (166.9 ± 95.3 Hz). We quantified the emergence of doublets using the first ISI, which significantly decreased from P14 to 21 and from P21 to 28 (**Figure 3.7B**; $p < 0.001$, Kruskal-Wallis with Wilcoxon rank sum post-hoc tests, $\chi^2_5 = 194.0$). Every transition between neighboring pairs of time-points was significant as well ($p < 0.001$).

We next measured the input-output relationship for action potential generation at P7, 14, 21, and 28 (n = 7, all groups), using 1 s, square-wave current injections applied from a resting membrane potential of -60 mV. As illustrated in **Figure 3.7C**, as neurons matured they required more current to generate the same output frequency.

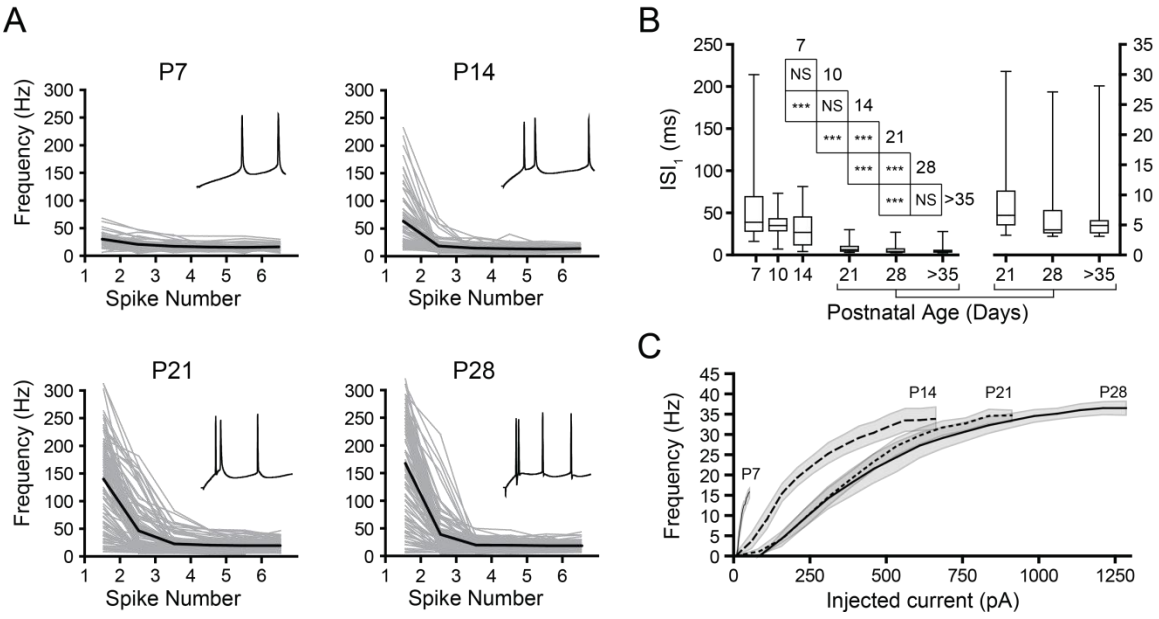

Figure 3.7**: **Maturation of spike trains in BLA principal neurons.** (A) Instantaneous action potential frequency is plotted for individual neurons (grey lines) and group mean (black lines) at each time point. Neurons were depolarized such that the mean inter-spike membrane potential was near spike threshold (see Methods for details). The start of a representative spike train is inset in each plot to highlight differences in initial spike rate (n = 39 (P7), 75 (P14), 97 (P21), and 103 (P28) trains). (B) First interspike-interval for the spike trains in A is depicted in a box and whisker plot, with the later time-points shown on both y-axes (n = 45 (P7), 37 (P10), 53 (P14), 43 (P21), 54 (P28), and 59 (P>35)). Significance was assessed using a Wilcoxon rank-sum test and pairwise comparisons were made for each age group with up to four neighboring time-points (see inset table for results) using a Bonferroni correction for the resulting 9 comparisons (,*

p < 0.001; NS: not significant, p > 0.05). (C) Input-output curves for neurons at each time point are depicted as mean (line) and standard deviation (grey band) of average firing frequency in response to a 1 s square current step from holding potential at -60 mV (n = 7 for all time points).

Interestingly, although the maximal firing frequency (mean ± SD) significantly increased ($p < 0.001$, One-way ANOVA with Tukey's post-hoc tests, $F_{3,23} = 25.96$) from P7 (15.9 ± 3.3 Hz) to P14 (33.9 ± 7.3 Hz), the transitions ($p > 0.05$) from P14 to P21 (34.7 ± 3.7 Hz) and from P21 to P28 (36.5 ± 4.2 Hz) were not significant.

Development of the Action Potential Waveform

We reasoned that the observed changes in spike trains were likely due, in part, to maturation of the waveform of individual action potentials. Consequently, to quantify changes in action potential waveform, neurons were probed with a depolarizing current ramp lasting 250 ms, whose amplitude was adjusted to elicit a single action potential. **Figure 3.8A** illustrates the mean action potential waveforms from each age group. As can be seen, action potential threshold exhibited a significant, negative shift of approximately 7 mV from P7 to P28 (Kruskal-Wallis, $\chi^2_5 = 164.5$, **Figure 3.8B**). The median threshold was -33.5 mV at P7 (n = 51), -34.7 mV at P10 (n = 35), -37.0 mV at P14 (n = 52), -40.9 mV at P21 (n = 43), -40.3 mV at P28 (n = 56), and -41.3 mV at >P35 (n = 55). Statistically significant transitions occurred from P10 to P14 and P14 to P21 ($p < 0.001$, Wilcoxon rank sum post-hoc tests). In addition, action potentials became much faster; the action potential half-width decreased between P7 and P28 (**Figure 3.8C)**, with the value at each time-point being significantly faster than at the previous ($p < 0.01$, Kruskal-Wallis with Wilcoxon rank sum post-hoc tests, $\chi^2_5 = 217.8$). The median half-width was 1.39 ms at P7 (n = 49), 1.23 ms at P10 (n = 35), 1.11 ms at P14 (n = 52), 0.90 ms at P21 (n = 44), 0.76 ms at P28 (n = 56), and 0.83 ms at P>35 (n = 57). Action

potential 10-90% rise-time also decreased over this window, but the change was more gradual (**Figure 3.8D**). Here, the median rise-time was 0.56 ms at P7 (n = 51), 0.47 ms at P10 (n = 37), 0.42 ms at P14 (n = 55), 0.37 ms at P21 (n = 45), 0.30 ms at P28 (n = 57), and 0.32 ms at P>35 (n = 55). The only significant neighboring comparison in rise-time was between P21 and P28 ($p < 0.001$, Kruskal-Wallis with Wilcoxon rank sum post-

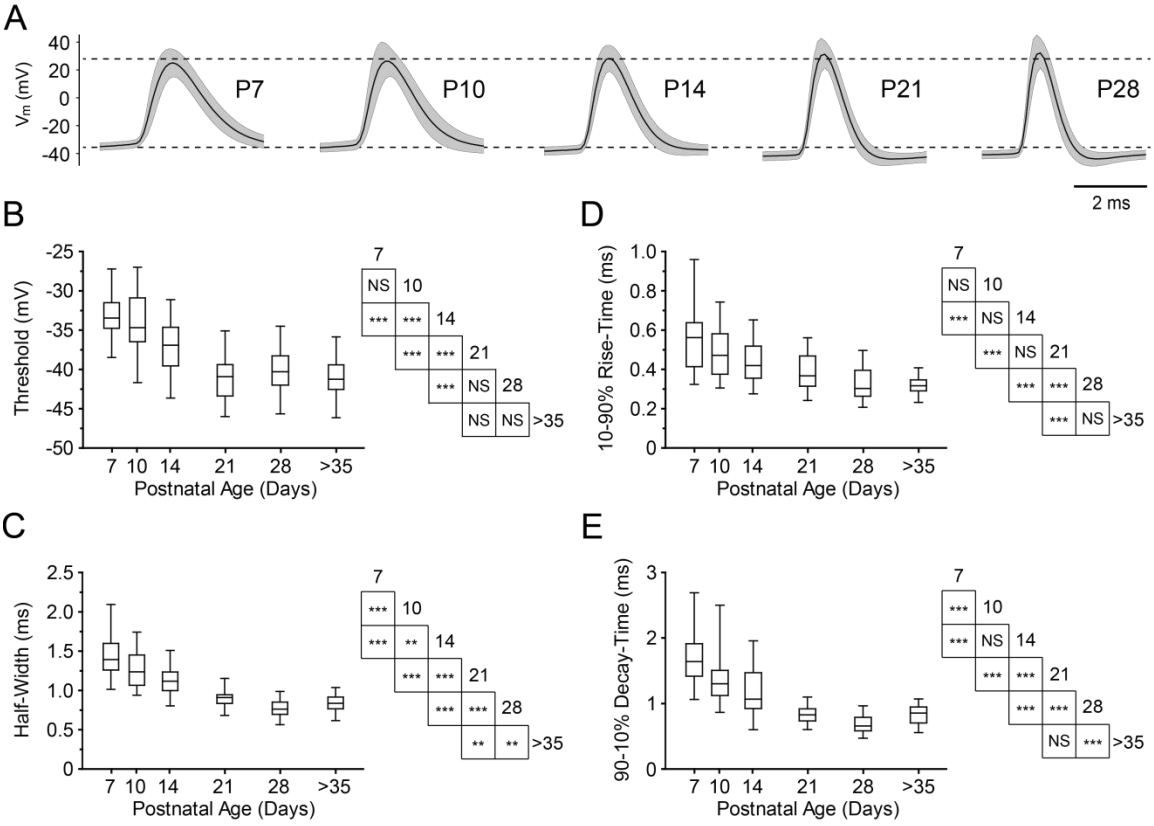

***Figure 3.8**: **Action potentials of BLA principal neurons develop a more hyperpolarized threshold and become faster with age**. (A) Action potential waveform, depicted as mean (black line) and standard deviation (grey band), for neurons across postnatal development (n = 48 (P7), 34 (P10), 46 (P14), 40 (P21), 54 (P28)). (B-E) Box and whisker plots depict action potential threshold (B), half-width (C), 10-90% rise-time (D), and 90-10% decay time (E) for neurons at each time point (n = 49-51 (P7), n = 35-37 (P10), n = 52-55 (P14), n = 43-45 (P21), n = 56-57 (P28), and n = 55-*

*57 (P>35)). Significance was assessed using a Wilcoxon rank-sum test and pairwise comparisons were made for each age group with up to four neighboring time-points (see inset tables for results) using a Bonferroni correction for the resulting 9 comparisons (***, p < 0.001; **, p < 0.01; NS: not significant, p > 0.05).*

hoc tests, χ^2_5 = 134.7), but every transition across two time-points was significant (p < 0.001). Finally, the 90-10% decay-time also decreased more than two-fold from P7 to P28 (**Figure 3.8E**) and decreased significantly between every neighboring pair of time-points aside from P10 to 14 (p < 0.001, Kruskal-Wallis with Wilcoxon rank sum post-hoc tests, χ^2_5 = 201.6). Here, the median decay-time was 1.64 ms at P7 (n =50), 1.30 ms at P10 (n = 36), 1.07 ms at P14 (n = 53), 0.83 ms at P21 (n = 43), 0.66 ms at P28 (n = 56), and 0.86 ms at P>35 (n = 56).

Development of Afterhyperpolarization

The maturation of action potential duration strongly suggested that calcium influx due to individual spikes would also change significantly. Hence, we next examined the developmental expression of post-spike afterhyperpolarizations (AHPs), which have been shown to have some calcium-dependency in amygdala principal neurons (Faber & Sah, 2002) and could further contribute to the observed changes in spike trains. As expected, AHP expression also matured across the first postnatal month, with clear changes in both the fast and medium AHP (fAHP and mAHP, respectively). **Figure 3.9A** illustrates representative AHPs of BLA principal neurons at P7, 14, 21, and 28. As can be seen, the mAHP is already present at P7, whereas a distinct fAHP does not appear until P21. As shown in **Figure 3.9B**, the mAHP became faster and more shallow from P7 to P28, with times-to-peak of 91.4 ± 11.8 ms at P7 (n = 8), 69.0 ± 5.8 ms at P14 (n = 15), 59.8 ± 3.8 ms at P21 (n = 22), and 57.2 ± 3.6 ms at P28 (n = 42). The amplitude of the mAHP was -14.9 ± 2.4 mV at P7, -13.2 ± 1.9 mV at P14, -12.4 ± 2.6 mV at P21, and

-11.1 ± 1.9 mV at P28. There was a significant effect of age on mAHP amplitude ($p < 0.001$, One-way ANOVA, $F_{3,83} = 8.95$) and duration ($p < 0.01$, Kruskal-Wallis, $\chi^2_3 = 11.45$). The fAHP emerged at P14 (**Figure 3.9C**), with 33% of neurons exhibiting a fAHP. The proportion increased to 68% by P21 and to 74% by P28. The fAHP became faster across this period, with times-to-peak (mean ± SEM) of 2.8 ± 0.1 ms at P14 (n = 5

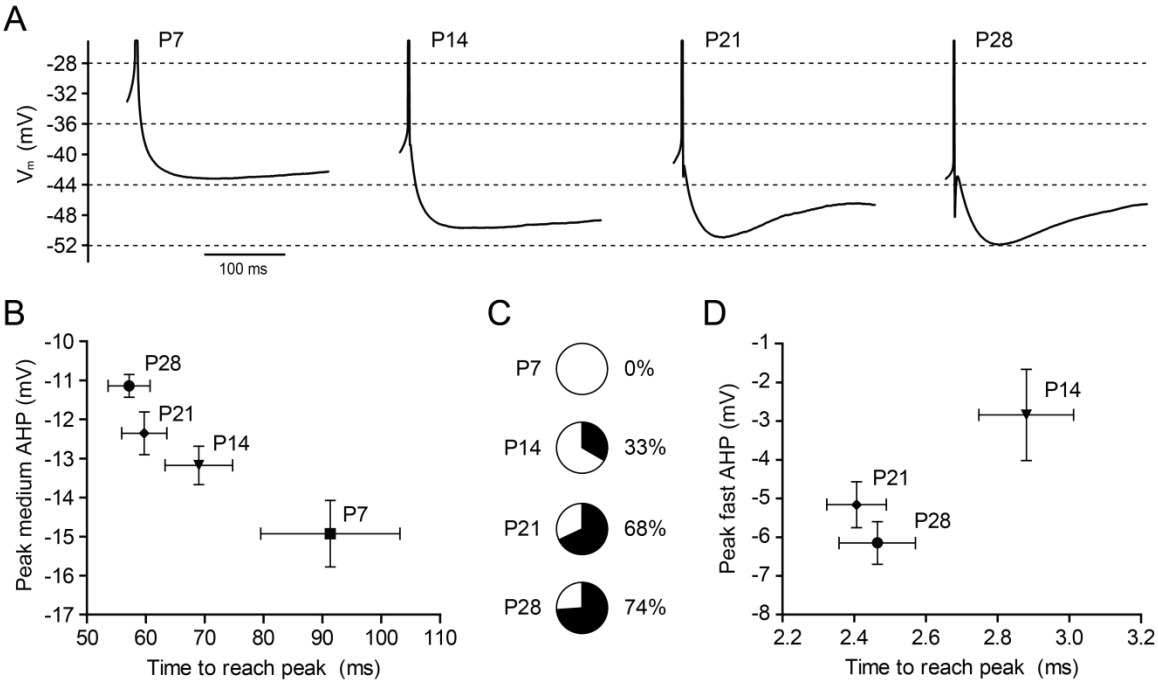

***Figure 3.9**: **Action potential medium AHP matures and a fast AHP emerges with age.** (A) Changes in afterhyperpolarization (AHP) waveform are illustrated by spike-triggered averages (from at least 8 action potentials) of one free-firing, representative neuron for each time point. (B, D) Derived from spike-triggered averages, the voltage difference between a neuron's action potential threshold and its medium (B) or fast (D) AHP peak (mean ± SEM) is plotted versus time elapsed from spike initiation to AHP peak (mean ± SEM) for each time point (n = 8 (P7), 15 (P14), 22 (P21), and 31 (P28)).*

There was a significant effect of age on mAHP amplitude ($p < 0.001$, One-way ANOVA) and duration ($p < 0.01$, Kruskal-Wallis). Only neurons with a discernible fast AHP were included in analysis for D, and the proportions of neurons expressing a fast AHP at each time point are depicted as pie charts (C).

of 15), 2.4 ± 0.1 ms at P21 (n = 15 of 22), and 2.4 ± 0.1 ms at P28 (n = 31 of 42). The fAHP also became deeper, with amplitudes (mean ± SD) of -2.8 ± 2.6 mV at P14, -5.2 ± 2.3 mV at P21, and -6.1 ± 3.1 mV at P28. The effect of age was not significant for fAHP amplitude ($p = 0.052$, One-way ANOVA, $F_{2,48} = 3.147$) and duration ($p = 0.061$, Kruskal-Wallis, $\chi^2_2 = 5.61$).

No Effect of Sex on Postnatal Changes in Physiological Properties

Due to differences in emotional processing and development of emotional behaviors across sexes, there is great interest in sex differences in amygdala maturation. Therefore, we performed a statistical analysis to assess sex differences in many of the physiological properties discussed above. Using a two-way ANOVA with factors of age and sex, we compared groups of between 8 and 16 neurons per sex at P14, 21, and 28. We found no main effect of sex ($p > 0.05$) in any of the parameters tested (R_{in}, τ_{memb}, action potential threshold, half-width, 10-90% rise-time, 90-10% decay-time, and first ISI). We conducted a post-hoc power analysis using *G*Power* (Erdfelder *et al.*, 1996) to assess whether we had sufficient power to detect an effect of sex. The power to detect a large effect size ($f = 0.40$, Cohen, 1977) was 0.94, but the power to detect a medium-sized effect ($f = 0.25$) was 0.59. Therefore, we cannot rule out the possibility of an effect of sex on these parameters in development, but expect such an effect would not be large. It is important to note that all measures were taken before sexual maturity, and large effects of sex may emerge by adulthood.

Discussion

In this study, we have provided the first evidence that physiological properties of principal neurons in the rat BLA undergo significant change during the first postnatal month. Characterizing how neurons of the amygdala develop is fundamental to understanding normative emotional development and, in turn, how risk factors and genetic predispositions are translated into developmental emotional disorders like anxiety, depression, autism spectrum disorders, and schizophrenia (Pine, 2002; Kim-Cohen *et al.*, 2003; Kessler *et al.*, 2005; Monk, 2008). Emotional processing, in particular fear learning, is critically dependent on the BLA (Davis, 2000; LeDoux, 2000), and the rapid and robust changes to fear learning observed during the first postnatal month in rats suggest the BLA develops profoundly during this period (Campbell & Ampuero, 1985; Moye & Rudy, 1987; Hunt *et al.*, 1994; Sullivan *et al.*, 2000; Kim & Richardson, 2007). To facilitate comparisons of the timing of our observations to milestones in other species, consider that an infant rat first opens its eyes and reaches comparable cortical maturity to a newborn human at around two weeks after birth, is weaned around three, and reaches sexual maturity between six and eight (Quinn, 2005). In our hands, BLA principal neurons exhibited the greatest physiological changes between P7 and P21. Furthermore, neuronal physiology at P28 very closely resembled that of neurons recorded after P35, as well as previous reports of adult BLA principal neurons. These findings suggest that the electrophysiological properties of neurons in the human amygdala may undergo the largest transitions before one year of age and continue to develop into early adolescence. All of these changes support the notion that the BLA and its contribution to emotional processing are in flux well into postnatal life, marking a period of vulnerability for the circuit and long-term emotional outcomes (Spear, 2009).

Maturation of passive membrane properties

The most fundamental aspect of physiology in which we observed changes was passive membrane properties. For both input resistance (R_{in}) and membrane time constant (τ_{memb}), a great proportion of maturation took place by P21. In fact, R_{in} decreased 6-fold and τ_{memb} more than 3-fold between P7 and P21. The values we report for R_{in} and τ_{memb} at P28 and >P35 match those reported previously for adult BLA principal neurons (Rainnie *et al*., 1993), suggesting these neurons are physiologically mature by P28. These trajectories are also comparable to those seen in sensorimotor (McCormick & Prince, 1987) and prefrontal cortex (Zhang, 2004) as well as thalamus (Ramoa & McCormick, 1994). The decreases in R_{in} and τ_{memb} are consistent with the observed increase in cross-sectional area of BLA neurons (Berdel *et al*., 1997a) and likely involve insertion of ion channels into the membrane. The developmental reduction of R_{in} would, in isolation, reduce responsiveness to synaptic input, and may serve as a homeostatic mechanism to compensate for increasing synaptic strength, as seen elsewhere (Zhang, 2004). The larger τ_{memb} in younger neurons means their voltage responses to synaptic input would be slower, promoting temporal summation of inputs. However, this would also reduce temporal precision of action potentials, meaning preadolescent amygdala neurons may be less able to coordinate action potentials and take advantage of temporal coding and spike-timing dependent plasticity.

Maturation of membrane potential oscillations and resonance

Passive membrane properties like τ_{memb} also help shape oscillatory properties of neurons, which influence the sensitivity of neurons to input and production of action potentials based on frequency. Over the first postnatal month, the proportion of BLA principal neurons expressing spontaneous membrane potential oscillations (MPOs) increased substantially and the frequency of those MPOs increased. Spontaneous

MPOs are expressed in adult BLA principal neurons in the guinea pig at a proportion comparable to that seen here at P21 and P28 (Pape *et al*., 1998). The change in frequency with development was not significant, although similar trends have been observed in entorhinal cortex (Boehlen *et al*., 2010) and midbrain (Wu *et al*., 2001). Interestingly, the MPO was abolished by application of 1 µM tetrodotoxin (unpublished observation), suggesting the oscillation is promoted by synaptic activity.

Maturation of intrinsic oscillatory activity in BLA principal neurons also manifests as a change in the preferred resonance frequency. Intrinsic resonance has a similar time-course of development to the MPO, expressing a mature phenotype in the BLA at P21. Resonance and MPOs also exhibit coordinated development in neurons of the entorhinal cortex (Burton *et al.*, 2008; Boehlen *et al.*, 2010). These two phenomena are mediated by a similar set of voltage-gated currents and have similar frequency preference (Lampl & Yarom, 1997; Hutcheon & Yarom, 2000; Erchova *et al.*, 2004). The mean peak resonance frequency we report here for BLA principal neurons at P28, 5.69 Hz, differs substantially from those reported previously for the guinea pig, 2.5 Hz (Pape & Driesang, 1998), and the adult rat, 4.2 Hz (Ryan *et al*., 2012). While these differences could be due to continued maturation of oscillatory properties after P28, we believe it is more likely due to differences in species or recording voltage, which is known to impact resonance (Pape & Driesang, 1998; Tseng & Nadim, 2010).

Spontaneous MPOs can directly influence spike timing (Desmaisons *et al.*, 1999; Richardson *et al.*, 2003), and in our hands, action potentials were phase-locked with the peak of the spontaneous MPO in some neurons at P28. Oscillatory properties of individual neurons contribute to the production of network oscillations (Lampl & Yarom, 1997; Tohidi & Nadim, 2009), which are an important component of communication between distant brain regions (Engel *et al.*, 2001; Singer, 2009; Canolty & Knight, 2010; Fujisawa & Buzsaki, 2011). Coherent oscillations are expressed by the amygdala and

downstream target regions, including the hippocampus and prefrontal cortex, during fear acquisition and expression (Madsen & Rainnie, 2009; Sangha *et al.*, 2009; Pape & Pare, 2010). Importantly, the frequency of these coherent oscillations overlaps with the frequency of peak resonance and spontaneous MPOs in BLA principal neurons at P28, suggesting the emergence of these properties contributes to the mature expression of fear. Theta oscillations in local field potentials from the hippocampus increase in frequency throughout the third and fourth postnatal weeks, corresponding with emergence of mature network properties (Wills *et al*., 2010). This finding further supports a role for development of the oscillatory properties of individual neurons in network function and mature behavior.

Considering the importance of oscillatory properties of individual neurons for the generation of network oscillations (Lampl & Yarom, 1997; Desmaisons *et al.*, 1999; Richardson *et al.*, 2003; Tohidi & Nadim, 2009), their emergence in the BLA should correspond with that of principal neuron resonance. Based on electroencephalograms of the developing rat brain, no discernible network oscillations are observed in the BLA from birth through P14. Prominent oscillations emerge by this age in other regions including cortex, hippocampus and thalamus (Snead & Stephens, 1983), suggesting network oscillations in the BLA develop relatively late. We have recently argued that network oscillations in the amygdala are promoted by organization of principal neuron MPOs by synaptic input from parvalbumin-expressing interneurons (Ryan *et al*., 2012). Interestingly, these interneurons emerge in the BLA at P14 and reach mature expression by P21 (Berdel & Morys, 2000), when mature oscillatory properties would render BLA principal neurons more susceptible to organization by parvalbumin interneurons.

Maturation of I_h and its contribution to resonance

The observed changes to resonance, as well as to passive membrane properties, were likely influenced by maturation of the voltage-sensitive current, I_h. This

current is critically involved in the expression of resonance properties (Hutcheon *et al.*, 1996; Hu *et al.*, 2002; Marcelin *et al.*, 2012) and contributes to input resistance at rest (Surges *et al*., 2004). Here we have shown an increase in amplitude and a decrease in activation time constant of I_h across the first postnatal month, as shown previously in other brain regions (Vasilyev & Barish, 2002; Khurana *et al.*, 2012). The interaction of a 7-fold increase in I_h current amplitude across this window with a nearly 10-fold reduction of R_{in} explains the fairly consistent amplitude of voltage sag at all ages. A consistent sag amplitude across the first postnatal month was also observed in entorhinal cortex despite increasing I_h conductance (Burton *et al*., 2008). The amplitude of I_h may be regulated throughout the first postnatal month to homeostatically maintain a consistent resting membrane potential. There are, however, visible changes in the voltage waveform of I_h because of faster I_h activation and τ_{memb}. We have preliminary evidence suggesting the changes in I_h are due to transitions in the expression of subtypes of HCN, the channel mediating I_h, in BLA principal neurons (Ehrlich, 2010), similar to in thalamic and hippocampal neurons (Bender *et al.*, 2001; Kanyshkova *et al.*, 2009). I_h activation kinetics were assessed by fitting the Cs^+ subtraction current with a two-term exponential equation at P14, P21, and P28, since I_h has previously been shown to have two distinct activation time constants (Pena *et al*., 2006). It is not clear why I_h at P7 appeared to have only a single activation time constant. While Cs^+ is not selective for HCN channels, we believe the subtraction currents are largely comprised of I_h. The hyperpolarization-activated current we observed likely involved activation of voltage-gated K^+ channels, which can also be sensitive to Cs^+. However, for Cs^+ to affect those channels, it must enter the cell, which is unlikely at the voltages used for this protocol.Assessed by blockade with Cs^+, I_h makes a substantial contribution to resonance as early as P14. From P14 to P28, Cs^+ shifted the peak resonance toward lower frequencies, but at P7, there was little impact. Interestingly, the greatest effects on resonance of I_h blockade

were seen at P14, when the resonance in Cs^+ resembled that seen at P7 in control conditions. This suggests I_h emerges as a major contributor to resonance between P7 and P14. Starting at P21, Cs^+ did not functionally abolish resonance by enhancing power preferentially in the lowest frequencies, as it did at P14. Cs^+ application had a diminishing effect on resonance with age following P14, suggesting other currents begin to play a greater role in shaping resonance. Considering the unique role I_h plays in shaping resonance at P14, at that age we expect profound sensitivity of resonance to neuromodulators that influence cAMP, a classic modulator of I_h. Developmental changes in neuromodulators contribute to maturation of I_h around P14 in the medial superior olive, further suggesting neuromodulation is relevant for neuronal function at that age (Khurana *et al*., 2012). Interestingly, I_h conductance in BLA principal neurons is reduced by the anxiolytic neurotransmitter neuropeptide Y and enhanced by the anxiogenic neurotransmitter corticotrophin-releasing factor (Giesbrecht *et al*., 2010).

Changes to resonance due to blockade of I_h are indirect and largely attributable to effects on τ_{memb}. There is a close relationship between τ_{memb} and peak resonance frequency (Hutcheon & Yarom, 2000), and the magnitude of resonance is linearly correlated with I_h amplitude (Marcelin *et al*., 2012). We showed that blockade of I_h directly impacts τ_{memb} but does not maintain the fitted relationship between τ_{memb} and peak resonance frequency, suggesting that, aside from passively contributing to resonance through τ_{memb}, I_h contributes actively through its voltage-dependence and activation kinetics. In hippocampal pyramidal neurons, the amplitude of I_h is tightly correlated with the magnitude of the resonance peak (Marcelin *et al*., 2012).

Maturation of trains of action potentials

As expected, trains of action potentials elicited by direct current injection changed qualitatively across the first postnatal month. At P7, neurons exhibited a

consistent action potential frequency throughout trains; as the animals aged, the frequency of the first two to three spikes increased dramatically, such that mature cells exhibited doublets or triplets at the onset of firing. Spike doublets have been documented in adult neurons of the basolateral (Rainnie *et al*., 1993) and lateral (Driesang & Pape, 2000) nuclei of the amygdala, and are thought to improve the fidelity of synaptic transmission (Lisman, 1997). Furthermore, doublets have been suggested to promote network oscillations and bridge the temporal gap between inputs to the amygdala representing conditioned and unconditioned stimuli during fear conditioning (Driesang & Pape, 2000). Interestingly, changes in dendritic morphology can directly affect spiking properties, including doublet firing (Mainen & Sejnowski, 1996), and experiments are underway to characterize morphological changes in these neurons during development.

In this study, maximal firing rate reached maturity in P14 cells, while in cortical pyramidal neurons, maximal firing rates have been reported to reach mature values as early as P2 (McCormick & Prince, 1987). This disparity is consistent with the late development of emotional processing relative to sensorimotor processing. The consistency of firing rates after P14 may be afforded by strengthening of I_A through insertion of Kv4 channels into the membrane (Vacher *et al*., 2006) to compensate for reduced medium afterhyperpolarizations (mAHPs).

It is important to note that, while spike trains elicited with square current pulses were relatively consistent across the first postnatal month, there were profound changes in the spontaneous activity of neurons depolarized to near threshold with direct current. Specifically, neurons at P7 exhibited highly erratic membrane potentials characterized by waves of depolarization, likely involving activation of low-threshold calcium currents, which resulted in bursts of action potentials and periods of quiescence. Throughout the first postnatal month, membrane potentials became more stable near threshold. It is

possible that the erratic membrane potentials in immature neurons were due to instability of the seal or physical qualities of the membrane. This is likely not the case based on the high R_{in} and repetitive firing exhibited at P7, properties indicative of a healthy membrane and seal. Furthermore, the membrane potential at P7 was stabilized by application of TTX (unpublished observation), suggesting the volatility was introduced by synaptic or intrinsic currents.

Maturation of action potentials and AHPs

There were also many developmental changes to properties of individual action potentials, including threshold, kinetics, and AHPs. Action potential threshold hyperpolarized until P21, potentially counteracting the effects of reduced R_{in} on neuronal excitability and acting to maintain consistent firing activity. The value we report for mature threshold (-41 mV) differed from the threshold values previously reported for mature BLA principal neurons (mean of -52 mV, (Rainnie *et al*., 1993), but this difference may be due to methods of recording (whole-cell patch vs. sharp) or analysis. Action potentials rise-time, decay-time and half-width were halved from P7 to P28, with the majority of change occurring by P21. Thalamic neurons also achieve mature action potential durations around P21 (Ramoa & McCormick, 1994), while neocortical projection neurons do so somewhat earlier, at approximately P14 (McCormick & Prince, 1987). Faster action potentials would allow for faster firing rates and may also impact calcium influx due to spiking, which could impact AHPs of action potentials.

Across the first postnatal month, AHPs matured in two ways: mAHPs became significantly faster and shallower while fast AHPs (fAHPs) became faster and deeper. Fast AHPs were not present at P7 but were present in two thirds of neurons by P21, when they exhibited adult-like waveforms. The emergence of fAHPs corresponds with faster action potential repolarization, and these phenomena are likely both due to maturation of fast voltage-gated potassium currents. A reduction in mAHP duration

across the first postnatal month has also been observed in entorhinal cortex (Burton *et al*., 2008). Medium AHPs can normalize inter-spike intervals and promote regular firing, hindering temporal coding mechanisms in favor of rate coding (Prescott & Sejnowski, 2008); smaller mAHPs in adult principal neurons are therefore another factor, along with smaller τ_{memb} and more prominent oscillations, that could promote temporal coding in mature emotional processing. Both fAHPs and mAHPs have been reported in adult BLA principal neurons (Rainnie *et al*., 1993), and the reported values suggest the trends we observed in AHP amplitude and duration continue past P28. A subset of adult BLA principal neurons has been shown to also express a slow AHP (Rainnie *et al*., 1993; Faber & Sah, 2002). Unfortunately, we were unable to assess the presence of a sAHP in immature BLA principal neurons with our data set. Future studies should address whether the presence of a sAHP emerges during postnatal development, as this could shed light on the developmental differentiation of principal neuron subtypes.

The trajectory of fAHP maturation corresponds with a reduction of the first inter-spike interval, such that almost all neurons at P28 have a fAHP and fire doublets. Interestingly, reduction of fAHP amplitude in the lateral amygdala through modulation of BK channels has been shown following stress and linked to anxiety (Guo *et al*., 2012), suggesting doublets are relevant for amygdala function. While the emergence of a fAHP likely involves changes in currents like BK, we cannot make any direct claims regarding the quantity or quality of underlying currents because we measured voltage deflections. Furthermore, because these voltage deflections are measured relative to action potential threshold, which is itself changing across development, the interaction of AHPs with currents regulating inter-spike interval may vary with age.

Maturation of amygdala morphology and connectivity

Although this is the first study characterizing the maturation of amygdala physiology, several studies have addressed other aspects of amygdala development.

The basolateral complex of the rat amygdala emerges by embryonic day 17 (E17; (Berdel *et al*., 1997b), with the majority of neurogenesis occurring between E14 and E16 (Bayer *et al*., 1993). The BLA continues to increase in volume until P14 (Berdel *et al*., 1997b), although the total number of neurons reaches the mature value at P7. Interestingly, in terms of BLA volume and number of neurons, throughout development no differences were observed across sex (Rubinow & Juraska, 2009); this corroborates our findings of no sex differences in principal neuron physiology. From birth to P7, the cross-sectional area of rat BLA neurons doubles, but at P7 the majority of neurons are still small and have only one or two main dendrites (Berdel *et al*., 1997a). By P14, the cross-sectional area is the same as in the adult. A 3-fold increase in total synapse in the BLA from P7 to P28, as measured by synaptophysin staining (Morys *et al*., 1998), probably reflects increased intrinsic connectivity as well as maturation of inputs to the amygdala.

The BLA contributes to a network of brain regions that produce and regulate emotional behavior, including the prefrontal cortex, which itself develops substantially during the first postnatal month (Van Eden & Uylings, 1985; Bourgeois *et al.*, 1994; Anderson *et al.*, 1995; Rakic, 1995; Gourley *et al.*, 2012). Afferents from cortical areas, including the prefrontal and auditory cortices, do not emerge in the BLA until around P13, while thalamic afferents are present as early as P7 (Bouwmeester *et al*., 2002). Interestingly, a functional interaction of the prefrontal cortex and BLA also develops late; the medial prefrontal cortex does not contribute to extinction learning until P24 (Kim *et al*., 2009).

We have provided evidence that neurons of the BLA are not physiologically mature at birth, and have argued that postnatal changes in amygdala function and emotional processing are likely driven by drastic changes to the physiology of amygdala neurons. Cellular physiology, however, as characterized here, is only part of the picture.

As is often the case in biological systems, form is function, and the morphology of developing neurons is critical to the development of their mature physiology and connectivity. In the subsequent chapter, we will explore the development of BLA principal neuron morphology in detail over the first postnatal month in order to correlate these changes with what we have learned here and what is known about the behavioral roles of the BLA.

Chapter 4

Morphology of Developing Principal Neurons in the Rat Basolateral Amygdala

Content presented in **Chapter 4** previously published as:
Morphology and dendritic maturation of developing principal neurons in the rat basolateral amygdala. **Ryan SJ**, Ehrlich DE, Rainnie DG. *Brain Struct Funct*. 2014 Nov 9

Abstract

The basolateral nucleus of the amygdala (BLA) assigns emotional valence to sensory stimuli, and many amygdala-dependent behaviors undergo marked development during postnatal life. We recently showed principal neurons in the rat BLA undergo dramatic changes to their electrophysiological properties during the first postnatal month, but no study to date has thoroughly characterized changes to morphology that may underlie the functional development of this neuronal population. We addressed this knowledge gap with reconstructions of biocytin-filled principal neurons in the rat BLA at postnatal days 7 (P7), 14, 21, 28, and 60. BLA principal neurons underwent a number of morphological changes, including a two-fold increase in soma volume from P7 to P21. Dendritic arbors expanded significantly during the first postnatal month and achieved a mature distribution around P28, in terms of total dendritic length and distance from soma. The number of primary dendrites and branch points were consistent with age, but branch points were found farther from the soma in older animals. Dendrites of BLA principal neurons at P7 had few spines, and spine density increased nearly five-fold by P21. Together, these developmental transitions in BLA principal neuron morphology help

explain a number of concomitant electrophysiological changes during a critical period in amygdala development.

Introduction

The basolateral nucleus of the amygdala (BLA) is critical for the production of appropriate emotional responses and the processing of emotional memories (Davis et al., 2003; LeDoux, 2007; Pape and Pare, 2010; Stuber et al., 2011). In recent years, many studies have implicated amygdala dysfunction in the etiology of psychiatric disorders, including anxiety, depression, and autism (Adolphs et al., 2002; Rainnie et al., 2004; Shekhar et al., 2005; Truitt et al., 2007; Koob and Volkow, 2010). These and other psychiatric disorders have roots in development, with early ages of onset or vulnerability to risk-factors early in life (Pine et al., 1998; Kim-Cohen et al., 2003; McEwen, 2003; Steinberg, 2005). Furthermore, a wealth of studies have identified deficits or changes to fear learning and expression during postnatal development (Rudy et al.,1993; Sullivan et al., 2000; Wiedenmayer and Barr, 2001; Hubbard et al., 2004; Kim and Richardson, 2008; Ito et al., 2009; Raineki et al., 2009; Pattwell et al., 2011, 2012). Despite the critical role for the amygdala in the expression of normative and maladaptive emotional behaviors, relatively few studies have characterized how BLA structure and function change with age.

Many prior studies addressing maturation of the BLA have been performed in rats. These studies have identified a window during the first postnatal month wherein the morphology and physiology of the nucleus undergo rapid and pronounced change. In particular, during this window the volume of the BLA increases while the density of neurons is reduced by half (Morys et al., 1998; Rubinow and Juraska, 2009; Chareyron et al., 2012). Neurons in the BLA grow during this period, with somas and dendritic arbors expanding (Escobar and Salas, 1993). We recently characterized the developmental changes to electrophysiological properties of BLA principal neurons, which comprise approximately 85% of BLA neurons and mediate virtually all output of the nucleus (Ehrlich et al., 2012). Specifically, we showed that BLA principal neurons

exhibit significant changes to their excitability and sensitivity to synaptic input across the first postnatal month, including a ten-fold reduction in input resistance and a hyperpolarization of action potential threshold greater than 5 mV. There are also concomitant changes to the waveform and patterning of action potential output, including the emergence of a fast after-hyperpolarization and spike doublets.

While previous studies have addressed gross morphological changes to the BLA and its component neurons throughout postnatal development, several important knowledge gaps remain. The only study to date examining the morphology of individual neurons in the BLA was not specific to principal neurons and did not address features such as the quantity or branching of dendritic material or the expression of spines (Escobar and Salas, 1993). Developmental changes to these features should substantially alter neuronal function, as the surface area of BLA principal neurons and the types of ion channels inserted into their membranes directly impact neurophysiology, including firing patterns (Mainen and Sejnowski, 1996). We have addressed this knowledge gap by characterizing BLA principal neuron morphology throughout the first postnatal month and in adulthood. Specifically, we used whole cell patch clamp at postnatal days 7, 14, 21, 28, and 60 to fill neurons with biocytin for post-hoc morphological reconstruction and analysis. Here, we describe a number of changes to the soma, dendritic arbor, and dendritic spines of developing BLA principal neurons.

Materials and Methods

Ethical approval

All experimental protocols strictly conform to National Institutes of Health guidelines for the Care and Use of Laboratory Animals, and were approved by the Institutional Animal Care and Use Committee of Emory University.

Animals

Male rats born in-house to time-mated Sprague–Dawley female rats (embryonic day 5 on arrival from Charles River, Wilmington, MA, USA) were used in all experiments. Pups were housed with the dam prior to weaning on postnatal day (P)22 or P23 (considering P1 as day of birth). After weaning, rats were isolated by sex and housed three to four per cage with access to food and water *ad libitum*. Animals attributed to each developmental time-point (P7, P14, P21, P28, and P60) were used on that day or the following day (P7–8, P14–15, P21–22, P28–29, and P60-61, respectively).

Slice Physiology

To perform neuronal reconstructions at each time-point, we performed whole-cell patch clamp to identify BLA principal neurons based on electrophysiological properties as described previously (Ehrlich et al., 2012) and to visualize neurons, biocytin (0.35%, Sigma-Aldrich, St Louis, MO, USA) was included in the patch recording solution. Acute brain *s*lices containing the BLA were obtained as previously described (Rainnie, 1999). Briefly, animals were decapitated under isoflurane anesthesia (Fisher Scientific, Hanoverpark, IL, USA) if older than 11 days, and the brains rapidly removed and immersed in ice cold, 95% oxygen–5% carbon dioxide-perfused ‘cutting solution' with the following composition (in mM): NaCl (130), $NaHCO_3$ (30), KCl (3.50), KH_2PO4 (1.10), $MgCl_2$ (6.0), $CaCl_2$ (1.0), glucose (10), ascorbate (0.4), thiourea (0.8), sodium pyruvate (2.0) and kynurenic acid (2.0). Coronal slices containing the BLA were cut at a thickness of 300–350 μm using a Leica VTS-1000 vibrating blade microtome (Leica Microsystems Inc., Bannockburn, IL, USA). Slices were kept in oxygenated cutting solution at 32°C for 1 h before transferring to regular artificial cerebrospinal fluid (ACSF) containing (in mM): NaCl (130), $NaHCO_3$ (30), KCl (3.50), KH_2PO_4 (1.10), $MgCl_2$ (1.30), $CaCl_2$ (2.50), glucose (10), ascorbate (0.4), thiourea (0.8) and sodium pyruvate (2.0).

Patch clamp recording

Individual slices were transferred to a recording chamber mounted on the fixed stage of a Leica DMLFS microscope (Leica Microsystems Inc., Bannockburn, IL, USA) and maintained fully submerged and continuously perfused with oxygenated 32°C ACSF at a flow rate of 1–2 mL min^{-1}. The BLA was identified under 10x magnification. Individual BLA neurons were identified at 40x using differential interference contrast (DIC) optics and infrared (IR) illumination with an IR sensitive CCD camera (Orca ER, Hamamatsu, Tokyo Japan). The location of recorded neurons was chosen randomly throughout the BLA. Putative principal neurons were selected based on soma size, and their identities were later verified electrophysiologically, as described below. Patch pipettes were pulled from borosilicate glass and had a resistance of 4–6 MΩ. Patch electrode solution had the following composition (in mM): potassium gluconate (130), KCl (2), HEPES (10), $MgCl_2$ (3), K-ATP (2), Na-GTP (0.2), phosphocreatine (5), and 0.35% biocytin, titrated to pH 7.3 with KOH, and 290 mosmol L^{-1}. Data acquisition was performed using either a MultiClamp 700A or an Axopatch 1D amplifier in conjunction with pCLAMP 10.2 software and a DigiData 1322A AD/DA interface (Molecular Devices, Sunnyvale, CA, USA). Whole-cell patch clamp recordings were obtained and low-pass filtered at 2 kHz and digitized at 10 kHz. The membrane potential was held at −60 mV for all neurons if not specified . Cells were excluded if they did not meet the following criteria: a stable resting membrane potential more negative than −55 mV; access resistance lower than 30 MΩ; stable access resistance throughout recording, changing less than 15%; and action potentials crossing 0 mV. BLA principal neurons were distinguished from interneurons, as previously, by their input resistance and spiking pattern in response to injection of a series of 10 hyperpolarizing and depolarizing, 1 s long, square-wave current steps (Ehrlich et al., 2012; Rainnie et al., 2006). Current amplitudes were scaled so that, for each cell, the peak voltage deflections were to

approximately −80 mV and −40 mV. Traces were analyzed using Clampfit 10.2 (Molecular Devices, Sunnyvale, CA, USA).

Histochemical Processing

Patched neurons were labeled with biocytin (Sigma-*Aldrich, St Louis, MO, USA*) included in the patch pipette recording solution. After neurons were recorded for at least 15 minutes, slices were fixed in 10% buffered formalin (Fisher Scientific, Hanoverpark, IL, USA) for 12-72 hours, and then transferred to cryo-protectant for storage at -20 C. After three consecutive 10 minute washes in 0.05 M phosphate buffered saline (PBS), slices were permeabilized for 30 minutes in phosphate buffered saline (PBS) and 0.5% Triton X-100 (Sigma-Aldrich, St Louis, MO, USA). Slices were then treated with Alexa Fluor 488-conjugated Streptavidin (Invitrogen, Grand Island, New York, USA) diluted to 1:1000 in PBS with Triton X-100 overnight at room temperature. Slices were then washed 2 times for 1 hour each in 0.05 M PBS and washed for 10 minutes in 0.05 M phosphate buffer. Finally, the slices were mounted on glass slides, air dried for two to twelve hours, and cover-slipped with mowiol mounting medium (Sigma-*Aldrich, St Louis, MO, USA*). To create representative outlines of the nucleus at different positions along the rostrocaudal axis for depicting the location of recorded neurons, one rat at each juvenile time point was transcardially perfused and the BLA was traced in every sixth section of thickness 60 µm (P14, P21, and P28) or 90 µm (P7). The locations of neuron reconstructions were registered to theseoutlines, excluding 2 neurons for which location could not be recovered.

Neuronal reconstruction and Data Analysis

For morphological analysis, the dendritic arbor of each neuron was first reconstructed by hand using Neurolucida neuron tracing software (MicroBrightField, Colchester, VT) from single z-stack images taken at 10x magnification with a 0.4 µm step size using a Leica DM5500B spinning disk confocal microscope (Leica

Microsystems Inc., Bannockburn, IL, USA) and SimplePCI data acquisition software (Compix, Sewickley, PA). Slices were examined live at 63x to support tracing of fine or overlapping dendritic segments. Reconstructions of neuronal somas were performed using AutoNeuron workflow in Neurolucida from image stacks obtained with a 63x objective. Quantitative analysis of reconstructions was performed using Neurolucida Explorer (MicroBrightField). The volume and surface area of somas were estimated using the 'Marker and Region Analysis' subroutine to provide a 3-D contour summary. Dendritic length and branching were analyzed in Neurolucida Explorer using Sholl analyses with ring radius increments of 2 µm, and data were analyzed in Matlab (The MathWorks, Natick, MA, USA). Corrections were made for shrinkage due to tissue processing. Thickness of processed tissue samples was estimated using confocal microscopy and compared to known thickness of live samples before fixation and mounting. Tissue correction factors varied between 2.8 and 4.6, and there was no clear relationship between postnatal age and the degree of shrinkage.

To estimate the average spine density for BLA principal neurons, we manually counted dendritic spines with Neurolucida on image stacks of dendrite segments taken at 100x magnification. The sampling method is explained in **Figure 4.1**. For each neuron, spines were counted by a blinded experimenter on 10 non-overlapping dendritic segments. Each segment spanned 50 µm and was centered on 1 of 10 points in the dendritic arbor chosen pseudo-randomly by a custom Matlab script (available upon request). This script weighted each micron-long section of the dendrite evenly when making selections, so the distribution of sampled segments reflected the actual distribution of dendritic material with regard to branch order and primary dendrite. All protrusions were counted as spines. Total spine number was estimated for each neuron individually using the product of average spine density and aggregate dendritic length, defined as the sum of the lengths of all dendritic segments.

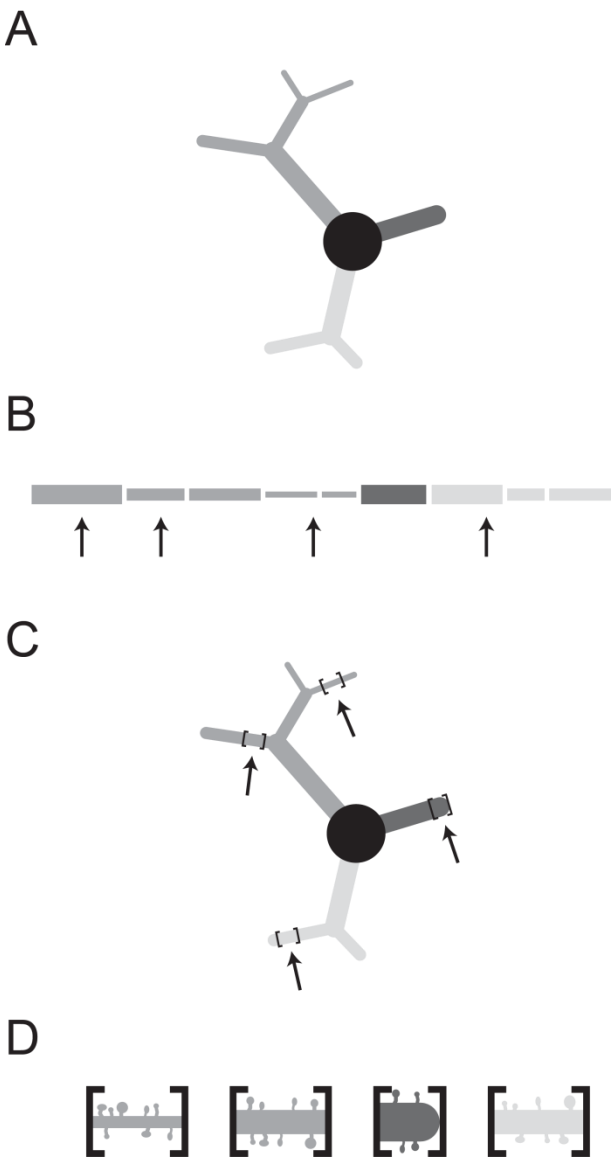

Figure 4.1: *Spine counting methodology is depicted for a cartoon neuron (A), comprised of a soma and three dendritic branches. (B) Locations for spine counting are randomly selected throughout the arbor (see Methods for details). (C) Segments spanning up to 50 µm, centered on the randomly chosen locations, are imaged at 100x magnification and (D) spines are counted manually. Average spine density is calculated for each segment and averaged across these locations to determine the average density for each neuron.*

Statistics

To compensate for age-dependent changes in variance (assessed using Bartlett's test with GraphPad, GraphPad Software Inc., La Jolla, CA, USA), data for soma volume, critical value of dendritic length, dendritic spine density, and total spine estimate were log-transformed before statistical analysis. Unless otherwise noted, data are presented as mean ± SEM. The values for aggregate dendritic length, critical value of dendritic length, dendritic spine density, and total dendritic spine estimate were fit with a Boltzman sigmoidal equation (**Equation 4.1**) in GraphPad. Most data sets were

analyzed with a One-way ANOVA to determine effects of age (GraphPad). Data from Sholl analyses were analyzed with Two-way ANOVA to determine effects of age and distance from soma. Data for aggregate dendritic length, branch point number, and spine density were compared across anterior and posterior BLA subdivision using Two-way ANOVAs (factors of subdivision and age).

Equation 4.1 $$y = A_2 + (A_1 - A_2)/(1 + e^{(V_{1/2} - x)/\alpha})$$

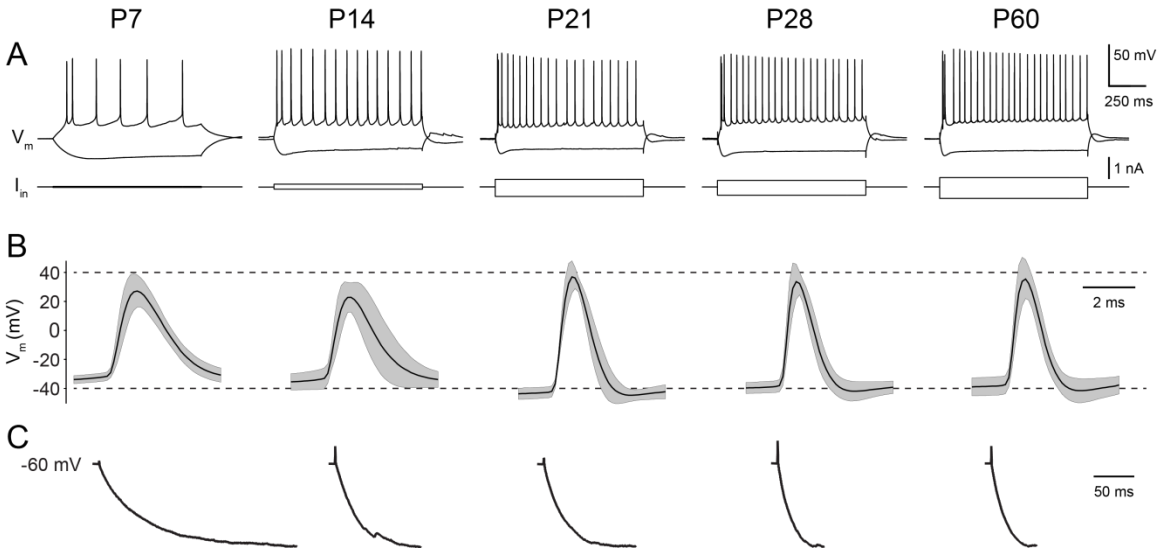

***Figure 4.2**: **BLA principal neuron electrophysiology matures in parallel with morphology**. Whole-cell patch clamp recordings were used to fill BLA principal neurons with biocytin. (A) Representative responses of developing neurons to depolarizing and hyperpolarizing current injections from holding potential of -60 mV. (B) Action potential waveform (mean as black line, standard deviation as gray band) of developing neurons included in this study. (C) Charging curves in response to hyperpolarizing current injection, averaged across neurons and normalized across time points.*

Results

In total, 40 BLA principal neurons were filled with biocytin and reconstructed at postnatal day 7 (P7), P14, P21, P28, and P60 (n = 8 per time-point). Basic electrophysiological properties were measured and found to be consistent with previously reported values (**Figure 4.2**; Ehrlich et al., 2012). Specifically, neurons at P7 and P14 were highly sensitive to direct current injection, reflecting large input resistances, but fired action potentials at lower frequencies than more mature neurons (**Figure 4.2A**). Action potentials had larger amplitudes and shorter durations with age, as action potential threshold became more hyperpolarized (**Figure 4.2B**). In addition, immature neurons charged more slowly in response to hyperpolarizing current injectons (**Figure 4.2C**).

Following recordings, filled neurons were stained and visualized post-hoc to make reconstructions (see Methods). Representative photomicrographs are provided at each time point (**Figure 4.3A**). The locations of reconstructed neurons are illustrated in **Figure 4.3B**. To compare dendritic arborization across age, representative neuronal reconstructions are depicted for each time-point in **Figure 4.4**. We observed a variety of developmental changes to BLA principal neuron morphology that are quantified in detail below. Principal neurons at all ages lacked a consistent orientation in the slice.

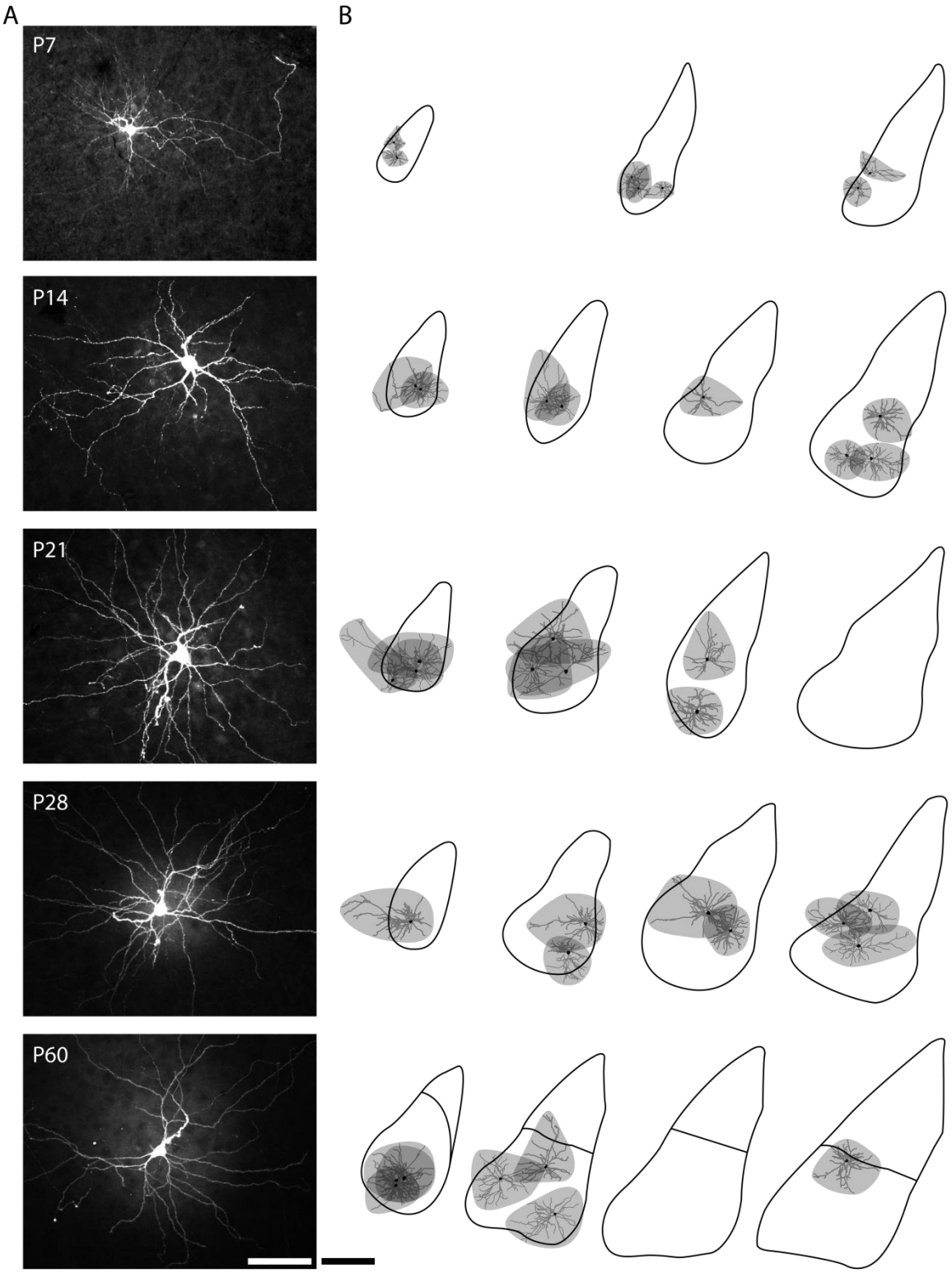

Figure 4.3: Location of reconstructed BLA principal neurons*. (A) Representative photomicrographs of filled neurons at each time point were produced from maximum*

projections of z-stack images through entire recording slices. Scale bar represents 100 µm. (B) Approximate locations and dendritic arborization of filled BLA neurons at each time point are depicted on representative coronal sections of BLA. Soma and dendrites are illustrated in black and gray, respectively, while the area covered by the dendritic arbor is shaded in gray. Traces were drawn from every sixth section of 90 µm (P7) or 60 µm thickness (P14-P28). Outlines at P60 correspond to Bregma coordinates -2.30 mm, -2.80 mm, -3.14 mm, and -3.30 mm. Scale bar represents 500 µm.

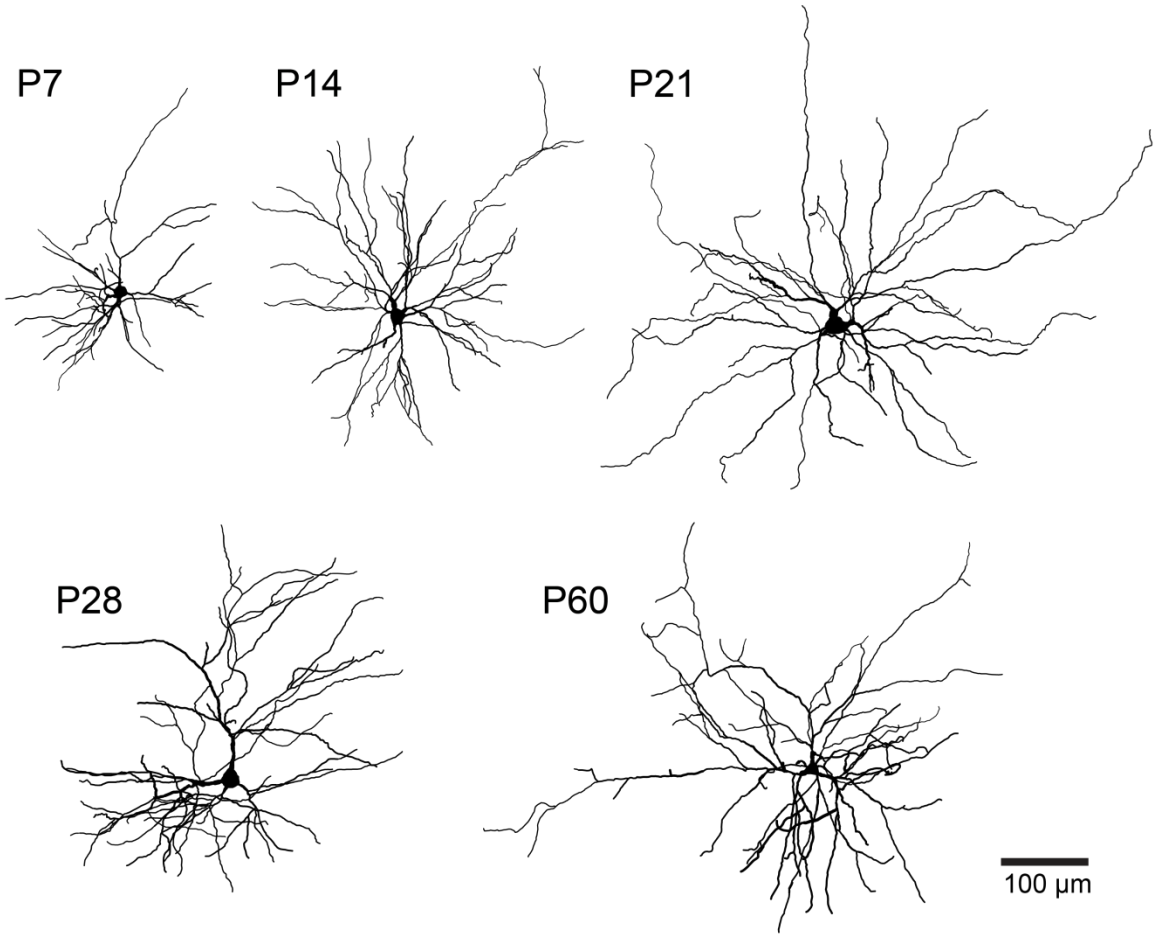

***Figure 4.4**: **Soma and dendrites of BLA principal neurons grow during the first postnatal month**. Reconstructions of representative, biocytin-filled BLA principal neurons at postnatal days 7 (P7), 14, 21, 28, and 60.*

Soma size

We first quantified somatic volume and surface area of BLA principal neurons throughout postnatal development (**Figure 4.5**). Somatic diameters ranged between 10 and 16 µm and somatic volume changed significantly during postnatal development (**Figure 4.5A**, $P < 0.001$, One-way ANOVA, $F_{4,29} = 6.51$), increasing across the first three postnatal weeks and then remaining stable until P60. Mean somatic volume increased by 66% from P7 to P21, followed by a change of less than 3% by P60. Somatic volume exhibited an asymptotic relationship with age, increasing from 2644 ± 186.7 μm^3 (mean ± SEM) at P7 (n = 7) to 3758 ± 176.5 μm^3 at P14 (n = 7; Tukey's *post hoc* test, $P > 0.05$), 4399 ± 444.9 μm^3 at P21 (n = 7, $P < 0.01$), 4250 ± 174.1 μm^3 at P28 (n = 6, $P < 0.01$), and 4304 ± 471.9 μm^3 (n = 7) by P60.

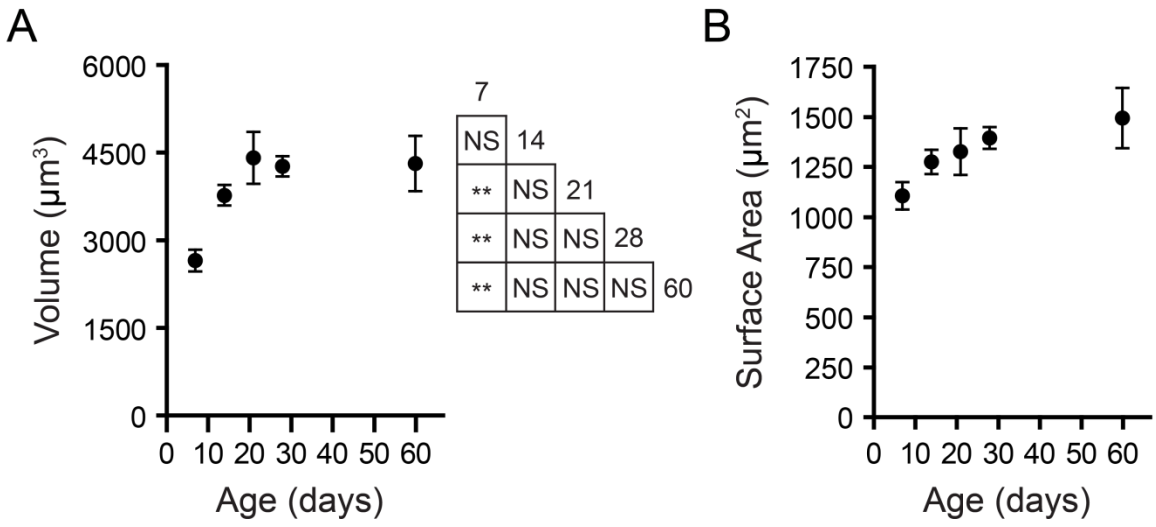

***Figure 4.5**: **Soma size increases across the first postnatal month, then decreases in adulthood**. (A, B) Soma volume (A) and surface area (B) of BLA principal neurons are depicted as mean ± SEM at postnatal days 7 (P7), 14, 21 and 28. At P7, P14, P21 and P60, n = 7; at P28, n = 6. The results of Tukey's tests following one-way ANOVA are depicted in grids (* P < 0.05; ** P < 0.01; *** P < 0.001; NS: not significant).*

A qualitatively similar but non-significant trajectory was exhibited by somatic surface area (**Figure 4.5B**, $P > 0.05$, One-way ANOVA, $F_{4,29} = 2.146$). Somatic surface area increased from 1106 ± 68.2 μm^2 at P7 (n = 7) to 1276 ± 60.4 μm^2 at P14 (n = 7), 1327 ± 116 μm^2 at P21 (n = 7), 1395 ± 54.6 μm^2 at P28 (n = 6), and 1495 ± 150.9 μm^2 at P60.

Growth and Subsequent Retraction of Dendritic Arbor

Extensive remodeling of dendritic architecture of BLA principal neurons also occurred across postnatal development (**Figure 4.6**). The aggregate length of dendrites for each neuron changed significantly with age ($P < 0.0001$, One-way ANOVA, $F_{4,34} = 26.41$), increasing more than threefold across the first postnatal month (**Figure 4.6A**). Aggregate dendritic length increased significantly from 2.347 ± 0.184 mm at P7 (n = 7) to 5.417 ± 0.474 mm at P14 (n = 8; Tukey's *post hoc* test, $P < 0.001$), 6.665 ± 0.379 mm at P21 (n = 8; $P < 0.001$), 7.709 ± 0.432 mm at P28 (n = 8; $P < 0.001$), and 7.908 ± 0.540 mm at P60 (n = 8; $P < 0.001$). The aggregate dendritic length also increased significantly from P14 to P28 ($P < 0.01$). The distribution of aggregate dendritic length vs. age was fit with a sigmoidal Boltzmann function (**Eqn. 4.1**), which estimated the inflection point at $V_{1/2}$ = 10.72 days with a slope of α = 4.90 days. The lower asymptote of aggregate length was constrained to be greater than or equal to 0, and was estimated to be A_2 = 0.0 µm and the upper asymptote to be A_1 = 7837 µm. The goodness of fit was $R^2 = 0.749$. No difference in aggregate dendritic length was found between anterior and posterior subdivisions of the BLA (Two-way ANOVA, main effect of subdivision: $F_{1,26} = 0.59$, $P = 0.45$).

The observed increase in aggregate dendritic length with age corresponded with an increased distance of that material to the soma (**Figure 4.6B**). Using a Sholl analysis with concentric rings of 4 µm thickness, we were able to determine the critical value for dendritic length, defined as the radius of the Sholl ring with the greatest amount of

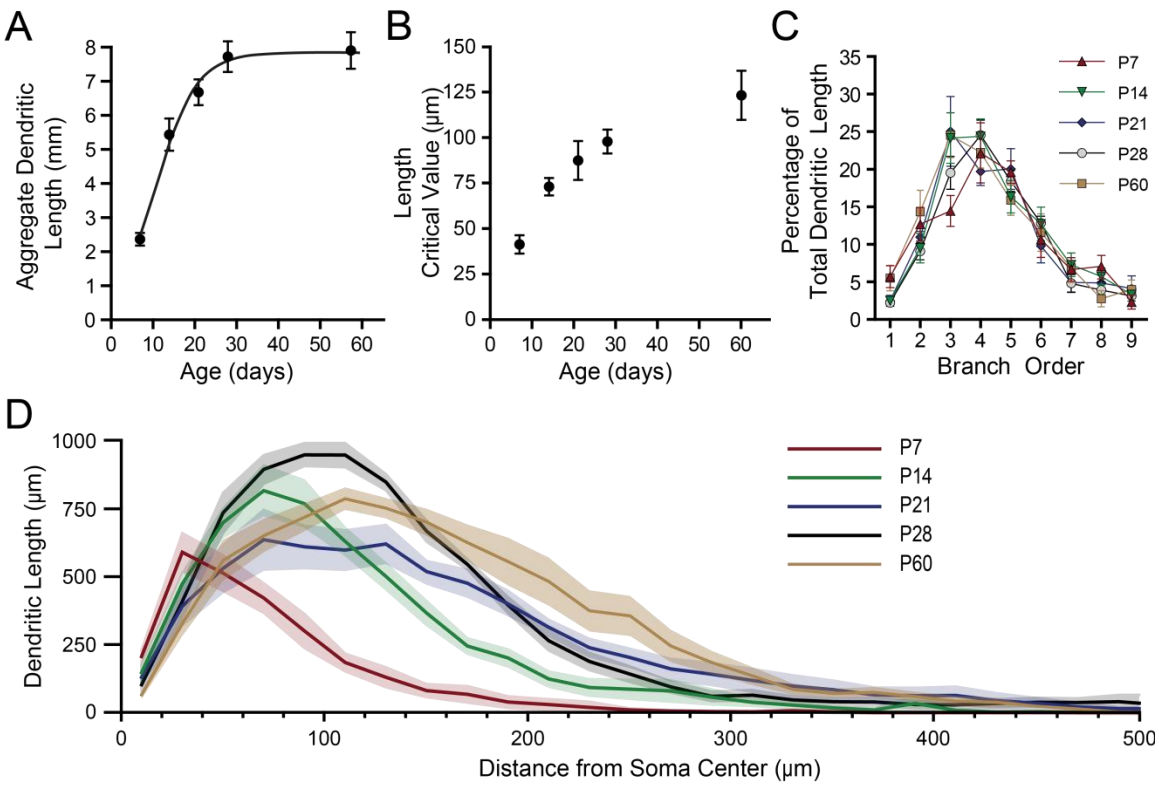

Figure 4.6: ***Dendritic arbors expand with a specific pattern across postnatal development***. *Sholl analysis was performed on reconstructed neurons with 20 µm steps between rings. (A, B) Aggregate length (A) and the critical value for length (B) of the dendritic arbor are plotted versus age as mean ± SEM, with a best-fit sigmioidal Boltzmann curve. The results of Tukey's tests following two-way ANOVA are depicted in inset grids (* P < 0.05; ** P < 0.01; *** P < 0.001; NS: not significant; n = 8 per time-point). (C) Percentage of total dendritic length found in branches of a given order is plotted as mean ± SEM for each age (n = 8 neurons per age). (D) The profile of dendritic length derived from the Sholl analysis is plotted as mean (black line) and SEM (grey band) versus distance from the center of the soma, illustrating the expansion and pruning of the dendritic arbor with age (n = 8).*

dendritic length. With age, dendrites became concentrated farther from the soma, with the critical value increasing significantly across the first postnatal month ($P < 0.0001$, One-way ANOVA, $F_{4,35} = 11.96$). Specifically, the critical value for dendritic length increased significantly from 41.0 ± 5.1 µm at P7 (n = 8; Tukey's *post hoc* test, $P < 0.01$) to 73.0 ± 4.8 µm at P14 (n = 8) and increased to 87.5 ± 10.7 µm at P21 (n = 7, $P < 0.001$ vs P7), 98.0 ± 6.5 µm at P28 (n = 8; $P < 0.001$), and 123.0 ± 13.5 µm at P60 (n = 8; $P < 0.001$).

The proximity of dendrites to the soma matures in a specific pattern, exemplified by the representative reconstructions in **Figure 4.4**. Across the first few postnatal weeks, dendrites extend farther from the soma. From P21 to P28 there is expansion of dendrites near the soma, and by P60 there is a reduction of dendrites proximal to the soma and an expansion of the more distal branches. Using Sholl analysis, we identified specific portions of the dendritic arbor where significant growth and retraction occur during postnatal development (**Figure 4.6D**; Two-way ANOVA with Bonferroni *post hoc* tests; main effect of age: $P < 0.0001$, $F_{4,1155} = 112.7$; main effect of distance from soma: $P < 0.0001$, $F_{34,1155} = 219.9$; interaction effect: $P < 0.0001$, $F_{136,1155} = 9.478$). In P7 neurons (n = 7), more than 98% of dendritic length is found within 200 µm of the soma. By P14, the proportion found within 200 µm drops to 91.6%, while 99.8% of dendritic length is found within 400 µm of the soma. From P7 to P14, there is also a significant expansion of dendrites in the region 40 to 180 µm from the soma ($P < 0.01$). By P21, only 96.8% of dendritic material is found within 400 µm of the soma, with the remainder extending as far as 640 µm from the soma. From P14 to P21, significant growth of dendrites occurs in the region 160 to 200 µm from the soma ($P < 0.01$). At P28, dendritic arbors occupy a similar space as those at P21, extending as far as 660 µm from the soma, with 96.9% of dendritic length found within 400 µm of the soma. From P21 to P28, there was a significant increase in dendritic material found in the region 40

to 120 µm from the soma ($P < 0.001$). The developmental expansion of dendrites in this window is reversed by P60, at which age significantly less dendritic material is found in the region 40 to 100 µm from the soma ($P < 0.05$ vs. P28). By P60, the reduction in dendritic length also occurs in the most distal parts of the arbor, with 99.1% of dendritic length being found within 400 µm of the soma (compared to 96.9% at P28).

We also examined the pattern of dendrite maturation by considering the growth of specific orders of dendritic branches (**Figure 4.6C**). When we normalized the dendritic length for individual orders of branches to the aggregate dendritic length of an entire neuron, we found the majority of dendritic length in second through sixth order dendrites. The length of dendrites varied significantly by branch order, but age did not significantly affect this distribution (Two-way ANOVA; main effect of branch order: $P < 0.0001$, $F_{8,268} = 54.58$; main effect of age: $P > 0.05$, $F_{4,268} = 0.26$).

Maturation of Dendritic Branching

We also investigated the maturation of branch points in the dendritic arbor, because the location of branch points determines the relationship between dendrite order and proximity to the soma (**Figure 4.7**). The number of primary dendrites was consistent throughout postnatal development (**Figure 4.7A**; $P > 0.05$, Kruskal-Wallis, $H(4) = 5.93$; mean ± SD: 7 ± 2.4 at P7, 5.75 ± 1.5 at P14, 5.5 ± 1.1 at P21, 6.1 ± 1.5 at P28, and 7.75 ± 2.4 at P60; $n = 8$). We analyzed the total number of branch points in the dendritic arbor for neurons at each time-point, and found no significant effect of age (**Figure 4.7B**; $P > 0.05$, Kruskal-Wallis, $H(4) = 7.10$; mean ± SD: 42 ± 18.0 at P7, 34.7 ± 13.3 at P14, 35.0 ± 8.5 at P21, 45.0 ± 8.8 at P28, and 34.5 ± 8.8 at P60; $n = 7$-8). No difference in branch point number was found between anterior and posterior subdivisions of the BLA (Two-way ANOVA, main effect of subdivision: $F_{1,26} = 2.36$, $P = 0.14$).

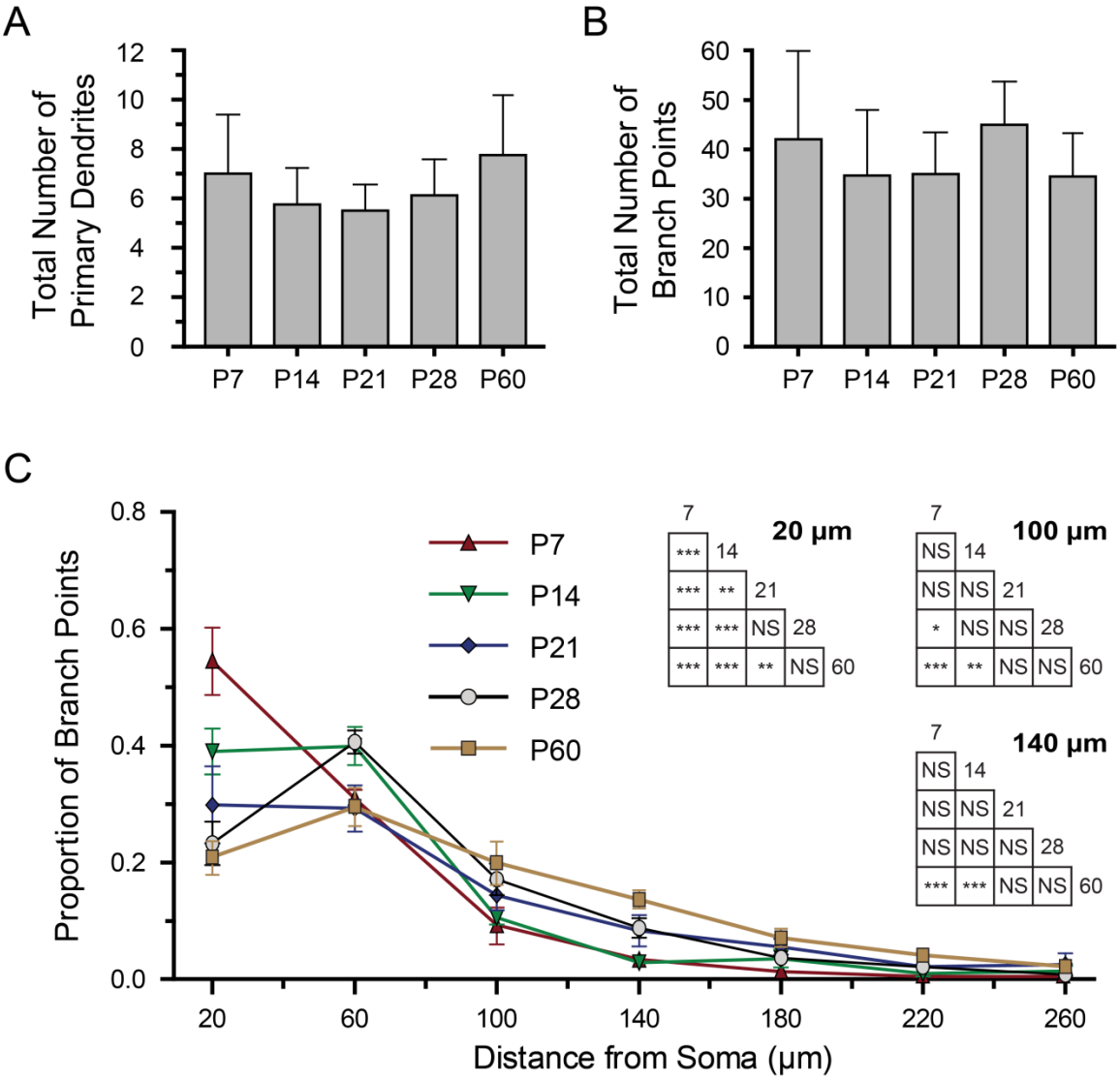

***Figure 4.7**: **Dendritic branch points become more distant from the soma during postnatal development**. (A, B) Bar graphs illustrate the mean ± SD of the total number of primary dendrites (A) and branch points (B) for BLA principal neurons at each time-point (n = 8). (C) The proximity of branch points to the soma was derived from Sholl analyses on reconstructed neurons with 40 µm thick rings, and the proportion of total branch points found in each ring is plotted as mean ± SEM (n = 8). The results of Tukey's tests following two-way ANOVA are depicted in inset grids for Sholl rings with significant effects of age, namely those centered at 20, 100, and 140 µm from the soma (* P < 0.05; ** P < 0.01; *** P < 0.001; NS: not significant).*

Furthermore, we quantified the proximity of branch points to the soma using a Sholl analysis with 40 µm thick rings. We found significant changes in the proximity of branch points to the soma with age (**Figure 4.7C**; Two-way ANOVA with Bonferroni *post hoc* tests; main effect of distance from soma: $P < 0.0001$, $F_{15,512} = 220.9$; interaction of age and distance from soma: $P < 0.0001$, $F_{60,512} = 6.167$). In P7 neurons, branch points were found very close to the soma, with 54.5 ± 15% occurring within 40 µm of the soma and 97.8 ± 4.3% occurring within 160 µm (mean ± SEM, n = 7). With age, branch points transitioned away from the soma: by P14, branch points were found more distally, extending as far as 320 µm from the soma, and with significantly fewer within 40 µm (9.0 ± 10.4%, $P < 0.001$, n = 7). The proportion of branch points within 40 µm of the soma also decreases significantly from P14 to P21 (29.8 ± 17%, $P < 0.01$, n = 7), and from P14 to P28 (23.3 ± 10.6%, $P < 0.001$, n = 8) and P60 (20.8 ± 8.2%, $P < 0.001$, n = 8). Conversely, the proportion of branch points located more distally increases significantly with age. Specifically, in P7 neurons 3.3 ± 4.3% of branch points are located 120 to 160 µm from the soma, while this number increases to 8.3 ± 7% at P21 and significantly increases to 8.8 ± 4.6% at P21 ($P < 0.001$) and 13.7 ± 4.4% at P60 ($P < 0.001$, see **Figure 4.7C**).

Developmental Emergence of Dendritic Spines

We next investigated the maturation of dendritic spines (**Figure 4.8**), which were much more apparent on the arbors of neurons at later time-points. Neurons at P7 frequently possessed smooth dendrites with few spines, while neurons at P21 and older had spine-laden dendrites (**Figure 4.8A**). To quantify the emergence of dendritic spines with age, we counted spines on 10 random segments of dendrite for neurons at each time-point (see Methods). We found that the density of dendritic spines changed significantly with age, increasing nearly six-fold across the time period studied, reaching adult levels at the end of the first postnatal month (**Figure 4.8B**; $P < 0.0001$, One-way

ANOVA, $F_{4,25}$ = 59.41; n = 6 neurons per time-point). Specifically, neurons at P7 had a spine density of 0.21 ± 0.03 spines/µm (mean ± SEM) which increased significantly to 0.53 ± 0.05 spines/µm at P14 ($P < 0.001$), 1.03 ± 0.12 at P21 ($P < 0.001$), 1.18 ± 0.05 at P28 ($P < 0.001$), and 1.29 ± 0.07 at P60 ($P < 0.001$). Spine density also increased significantly from P14 to all later time points ($P < 0.001$). The distribution of dendritic spine density vs. age was fit with a sigmoidal Boltzmann function (**Eqn. 4.1**), which estimated the inflection point at $V_{1/2}$ = 15.97 days with a slope of α = 3.89 days. The lower asymptote for spine density was estimated to be A_2 = 0.10 spines and the upper asymptote to be A_1 = 1.26 spines. The goodness of fit was R^2 = 0.868. No difference in spine density was found between anterior and posterior subdivisions of the BLA (Two-way ANOVA, main effect of subdivision: $F_{1,20}$ = 0.62, P = 0.44).

Using our measurements of mean spine density and the aggregate dendritic length from our reconstructions, we were able to estimate the total number of dendritic spines for each neuron (**Figure 4.8C**). These estimates suggest the total number of spines is more than seventeen times larger at P60 than at P7, as the number of spines increases significantly across postnatal development ($P < 0.0001$, One-way ANOVA, $F_{4,25}$ = 61.61; n = 6). Specifically, neurons at P7 had an estimated 601 ± 154 spines (mean ± SEM) which increased significantly to 2822 ± 379 spines at P14 ($P < 0.001$), 6694 ± 572 at P21 ($P < 0.001$), 8745 ± 698 at P28 ($P < 0.001$), and 10719 ± 1150 at P60 ($P < 0.001$). Total spine number also increased significantly from P14 to all later time-points ($P < 0.01$). As with spine density, the distribution of total dendritic spines vs. age was fit with a sigmoidal Boltzmann function (**Eqn. 4.1**), which estimated the inflection point at $V_{1/2}$ = 18.8 days with a slope of α = 4.92 days. The lower asymptote for spine density was constrained at A_2 = 0 spines and the upper asymptote was estimated to be A_1 = 10520 spines. The goodness of fit was R^2 = 0.83.

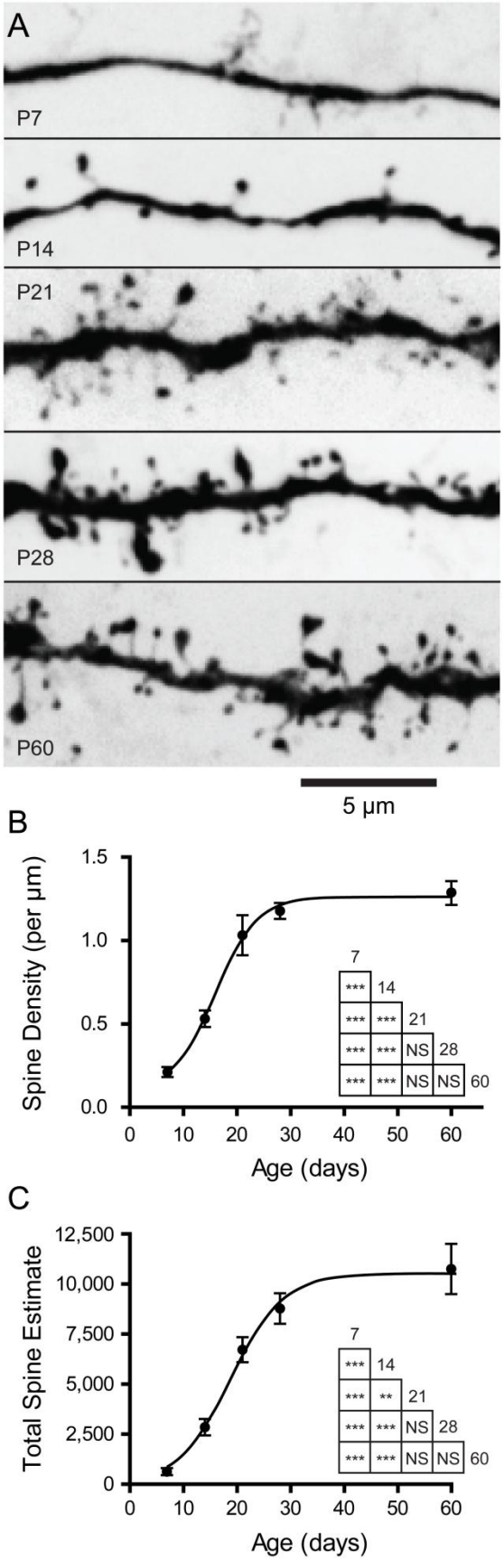

***Figure 4.8**: **Dendritic spines emerge during the first month of postnatal development in BLA principal neurons**. (A) Representative maximum projections of z-stack photomicrographs taken of segments of dendrites from filled BLA principal neurons at each time-point. (B,C) Dendritic spine density and the estimated total number of spines are plotted as mean ± SEM for neurons at each time-point (n = 6). The results of Tukey's tests following one-way ANOVA are depicted in inset grids (* P < 0.05; ** P < 0.01; *** P < 0.001; NS: not significant).*

Discussion

In this study, we presented a detailed analysis of the morphological properties of BLA principal neurons, conducted across the first two postnatal months in rats. During this window, BLA principal neurons exhibit a variety of structural changes with the most dramatic maturation occurring before P21. Significant morphological changes included: soma size increasing nearly two fold from P7 to P28; a three-fold increase in aggregate dendritic length from P7 to P21; a monotonic increase in length critical value from P7 to P60; a shift of branch points more distally in the dendritic arbor through P60; and an increase in the density of dendritic spines, reaching maturity around P28. Taken together, these developmental changes to principal neuron morphology help explain a wealth of electrophysiological changes occurring in the first postnatal month, including dramatic changes to passive membrane properties, action potential waveform and patterning, and intrinsic frequency preference (Ehrlich et al., 2012). The structural and functional maturation of amygdala neurons may underlie a variety of developmental changes to emotional behavior outlined in **Table 4.1** (for review, see King et al., 2013), which also occur during the first postnatal month and include conditioned avoidance (Sullivan et al., 2000), fear-potentiated startle (Hunt et al., 1994; Richardson et al., 2000), trace conditioning (Moye and Rudy, 1987), and extinction (Kim and Richardson, 2007). Our observations suggest that developmental changes in the mammalian amygdala extend from birth until adolescence, based on developmental milestones in the rat (Quinn, 2005).

Somatic Development

The most basic metrics of morphological development we examined were somatic volume and surface area. Values for both measures increased dramatically from P7 to P28, with soma volume nearly doubling in this window, and remaining stable between P28 and P60. Our measurements of adult soma size are larger than those

from a previous report in rat amygdala (Chareyron et al., 2011); the different estimates are likely due to technical differences, potentially due to methodology for calculating soma size or biasing towards larger neurons in patch clamp electrophysiology.

Behavior or Function	**Emerges**	**Reference(s)**
Avoidance of aversively conditioned stimuli	P10	Sullivan et al., 2000
Long-term potentiation of amygdala afferents	P10	Thompson et al., 2008
Innate defensive behavior (freezing upon exposure to conspecific)	P14	Takahashi, 1992
Amygdala activation upon exposure to conspecific	P12	Moriceau et al., 2004
Distinct responses to appetitive and aversive stimuli	P12	Camp and Rudy, 1988
Conditioned suppression of heart rate	P16-17	Campbell and Ampuero, 1985; Hunt, 1999
Conditioned freezing	P16-18	Hunt et al., 1998; Barnet and Hunt, 2006
Fear-potentiated startle to shock-paired tone or odor	P23-25	Hunt et al., 1994; Richardson et al., 2000; Barnet and Hunt, 2006
Extinction of learned fear becomes new learning, not erasure	P23	Kim and Richardson, 2007
Extinction requires NMDA receptors	P23	Langton et al., 2007
Re-extinction becomes amygdala independent	P24	Kim and Richardson, 2008
Trace and long-delay fear conditioning	P28	Moye and Rudy, 1987; Barnet and Hunt, 2005
Fear-potentiated startle to shock-paired light	P30	Hunt et al., 1994

Table 4.1*: Ontogeny of Amygdala-related Behavior in the Rat*

Contrasting our findings, in the macaque amygdala no significant effect of postnatal age was found on soma size (Chareyron et al., 2012). Nevertheless, we have shown that in rat BLA principal neurons the most drastic increase in soma size parallels the major period of dendritic outgrowth suggesting the soma may enlarge specifically during a period of dendritic outgrowth, potentially to produce proteins or support the assembly of

microtubules for dendritic growth (Baas and Lin, 2011). Pyramidal cells in layer V of the prefrontal cortex exhibit somatic enlargement with the same developmental trajectory as BLA principal neurons (Zhang, 2004), suggesting neuron maturation occurs in parallel in these regions.

Dendritic Morphology

Our data suggests almost all growth of the dendritic arbor of BLA principal neurons occurs by P28, with a large proportion occurring between P7 and P21. While the aggregate length of dendritic material reaches the mature value around P21, Sholl analyses suggest the dendritic arbor is still remodeled beyond this time-point, with dendrites retracting from P21 to P28, and extending further again between P28 and P60. We also used a Sholl analysis to compare the distribution of branch points throughout development. Interestingly, the proportion of dendritic length for each branch order was comparable across ages, suggesting there is an optimal distribution of branch points in the dendritic arbor that is maintained through development. The total number of branch points was consistent at every age, as was the number of primary dendrites. Our Sholl analysis further revealed a shift of branch points more distally with age. While P7 neurons have over half of their dendritic branch points within 40 μm of the soma, for P60 the proportion is below one-quarter. On the other hand, at P60 nearly one-sixth of branch points are found between 120 and 160 μm from the soma, a much greater proportion than at any earlier time-point. The net effect of these changes is that the critical value is found gradually farther from the soma until P28. Maturation of the dendritic arbor is dependent on the excitatory actions of GABA early in development, and loss of excitatory GABA in development severely limits dendritic arborization and complexity (Cancedda et al., 2007). We have reported that GABAergic transmission onto BLA principal neurons is excitatory at P7 but switches to inhibitory by P14, suggesting the first two postnatal weeks represent a critical period for dendrite

maturation (Ehrlich et al., 2013). Furthermore, activation of $GABA_B$ receptors early in development has been shown to promote dendrite outgrowth, and we have previously demonstrated large $GABA_B$ responses in P7 and P14 BLA principal neurons that diminish by P21, when dendrite expansion ends (Bony et al., 2013; Ehrlich et al., 2013).

The developmental trajectory of dendritic arbor morphology we report here is corroborated by previous studies in the BLA and developmental studies of pyramidal neurons in other brain regions. A previous study of BLA principal neurons in adult rats found a comparable spatial distribution of dendrites to our P60 time-point using a traditional Sholl analysis (Yajeya et al., 1997). A morphological analysis of developing layer V pyramidal neurons in somatosensory cortex by Romand and colleagues revealed a very similar growth pattern in the distribution of dendritic material, although their Sholl curves were notably broader, likely due to larger aggregate dendritic lengths (Romand et al., 2011). Stereological studies in the rat have also shown an increase in the volume of the rat BLA between P7 and P21, consistent with an expansion of dendritic arbors of BLA neurons during this period (Chareyron et al., 2012). Furthermore, a Golgi-Cox study of developing BLA neurons, which reported the area encompassed by the dendritic arbor, found a similar expansion during the first few postnatal weeks, albeit with substantially smaller arbors (Escobar and Salas, 1993). Notably, previous Golgi-Cox studies of adult BLA neurons have estimated the aggregate dendritic length between 300 and 2000 µm (Tosevski et al., 2002; Johnson et al., 2009; Pillai et al., 2012; Torres-Garcia et al., 2012), which differs greatly from our measurement of ~6,400 microns at P60. We argue that the Golgi-Cox technique provides underestimates of dendritic length, possibly by selectively sampling smaller neurons or staining only proximal dendritic segments. However, it is possible we are overestimating the dendritic length due to bias in the visual selection of neurons for patch clamp. Interestingly, while BLA principal neurons exhibit an increase in aggregate dendritic length of more than 3-

fold from P7 to P28, layer V pyramidal cells in the prefrontal cortex exhibit only a 2-fold increase in apical dendrite length during the same window (Zhang, 2004). These results suggest BLA principal neurons are relatively less developed at P7 than those in prefrontal cortex.

The growth of the dendritic arbor in both quantity and complexity has substantial implications for neuronal physiology, particularly passive electrical properties. The increase in neuronal surface area across the first postnatal month undoubtedly contributes to the concurrent, nearly ten-fold decrease in input resistance and three-fold decrease in membrane time constant we previously reported in this cell population (Ehrlich et al., 2012). Furthermore, multi-compartment modeling has revealed that expansion of the dendritic arbor can promote the expression of doublets of action potentials, driven by depolarization of the soma due to a dendritic spike (Mainen and Sejnowski, 1996). In our hands, the expansion of the dendritic arbor of BLA principal neurons during the first postnatal month reported here does in fact correspond with the emergence of doublets (Ehrlich et al., 2012). In addition, expansion of the dendritic arbor has the potential to effectively increase the diversity of presynaptic partners or sensory modalities of input for a BLA principal neuron, due to the topographical organization of sensory input to the BLA (McDonald, 1998). Interestingly, these inputs also undergo developmental change; tract tracing studies have demonstrated thalamic afferents are present in the BLA at P7 and remain relatively unchanged with age, while cortical afferents continue to mature throughout the first postnatal month (Bouwmeester et al., 2002). It will be critical for future studies to address the sensitivity of this developmental trajectory to experience, considering the well documented effects of stressors on the dendritic arborization of principal neurons in the adult BLA (Roozendaal et al., 2009; Padival et al., 2013) and in the case of autism spectrum disorders and

Fragile X syndrome (Kaufmann and Moser, 2000; Beckel-Mitchener and Greenough, 2004; Puram et al., 2011).

Dendritic Spine Emergence

As the dendritic arbor expands throughout the first postnatal month, BLA principal neurons come to express many more dendritic spines. We observed a progressive increase in the density of dendritic spines between P7 and P28, by which time spines are as dense as in adulthood (~1.2 spines/µm at P60). Comparable studies examining the development of dendritic spines in other brain regions have reported similar spine densities and developmental trajectories. For example, the spine density of layer V neurons in somatosensory cortex stabilizes around P21 at ~0.6 spines/µm (Romand et al., 2011). Previous measurements of spine density in the BLA have yielded values slightly lower than ours, ~0.7 spines/µm in late-adolescence (Torres-Garcia et al., 2012). This discrepancy may be because this study utilized the Golgi-Cox staining method, which, as discussed above, may be biased towards proximal dendrites. It is important to consider that our analysis counted and grouped all protrusions, including filopodia, and we have therefore likely overestimated the number of functional synaptic compartments. Furthermore, the developmental trajectories portrayed here do not account for possible age-dependent variation in the proportion of dendritic spines of various morphology.

Interestingly, previous studies of synapse formation in the developing BLA, measured by synaptophysin staining, show the number of presynaptic terminals reaches a peak at P14 (Morys et al., 1998), while our data show that dendritic spines reach about half their mature density at this age. Although synaptophysin is not specific for afferents of principal neurons or those targeting dendritic spines, this mismatch in synaptophysin and spine development suggests during the first few postnatal weeks glutamatergic presynaptic terminals may form synapses with dendritic shafts or release transmitter

without direct synaptic contact. The emergence of dendritic spines corresponds with the age when glutamate removal from synapses switches from primarily diffusion-based to uptake-dependent (Thomas et al., 2011). The early peak of synaptophysin expression may indicate an increase in glutamatergic transmission that could trigger the outgrowth of dendritic spines (Calabrese et al., 2006). In support of this notion, tract-tracing studies have shown that putative glutamatergic inputs to the BLA mature between P7 and P13 (Bouwmeester et al., 2002) and stabilize by P25, before undergoing pruning in late adolescence (Cressman et al., 2010). Dopaminergic and noradrenergic inputs to the BLA, which largely target spine shafts and heads on distal dendrites (Muller et al., 2009; Muly et al., 2009; Zhang et al., 2013), become more dense between P14 and P20 (Brummelte and Teuchert-Noodt, 2006). Our own previous work demonstrates the presence of stimulation-evoked and spontaneous glutamatergic transmission onto BLA principal neurons as early as P7 (Ehrlich et al., 2013), when very few spines are present.

The emergence of dendritic spines in BLA principal neurons has numerous potential implications for neurotransmission in the amygdala. Glutamatergic afferents to the BLA are thought to provide representations for sensory stimuli that are critical to amygdala function, including noxious and neutral stimuli that undergo plasticity during associative fear learning (Rodrigues et al., 2004; Maren, 2005; Pape and Pare, 2010). Dendritic spines provide a means of compartmentalization of biochemical and electrical signals related to neurotransmission (Shepherd, 1996; Lee et al., 2012), meaning the lack of spines early in development should impact the specificity of synaptic plasticity. Coincidentally, during the same window when spines emerge and reach mature numbers, there is increased abundance in BLA synaptic terminals of zinc, which promotes long-term potentiation of glutamategic synapses in the BLA (Mizukawa et al., 1989; Li et al., 2011). Interestingly, juvenile mice exhibit generalization of conditioned

fear, which could be related to poor specificity of synaptic plasticity (Ito et al., 2009). During infancy, rats also exhibit deficits to fear learning, and many forms of associative emotional learning emerge during the first few postnatal weeks (for review, see King et al., 2013). Perhaps most interesting is the observation that the amygdala is activated by odor-shock pairing after but not before P10, corresponding with the emergence of aversive conditioning and a change in amygdala synaptic plasticity (Sullivan et al., 2000; Thompson et al., 2008), precisely when dendritic spines begin to emerge.

Here we have shown that the morphology of BLA principal neurons matures profoundly across the first two postnatal months and discussed these changes in the context of concurrent, substantial changes to neuronal physiology, animal behavior, and synaptic plasticity. Together, these findings clearly illustrate that the first postnatal month, a previously defined critical period of rodent development, includes morphological changes in brain regions that process emotion. Developmental milestones in emotional behavior suggest the maturation of dendritic branching and spine emergence of amygdala neurons observed here, as well as the physiological changes we previously reported, contribute to the early emergence of innate fear-related behavior and the improved ability to form associative memories and integrate increasingly complex stimuli with age.

Chapter 5

Postnatal Development of Spike-Timing Precision and Membrane Potential Oscillations in Principal Neurons of the Rat Basolateral Amygdala

Introduction

In the previous chapters, we have outlined the developmental trajectory of basic morphological and physiological characteristics of BLA principal neurons, as well as mechanisms and regulatory properties of low-theta-frequency oscillations. Theta frequency oscillations play an important part in the BLA's role in processing affective sensory input. The amygdala, together with the prefrontal cortex and the hippocampus, produce a coordinated theta-frequency oscillation during the acquisition (Madsen & Rainnie, 2009) and retrieval (Sangha et al., 2009) of learned fear. Furthermore, anti-phase theta-frequency stimulation applied to the hippocampus and amygdala disrupts fear extinction, suggesting a critical role for these theta-frequency oscillations in facilitating communication between the two regions (Lesting et al., 2011). In the BLA, synchronized nhibition is a critical component of the mechanism for generating theta-frequency oscillations. BLA principal neurons receive large, highly synchronized, compound inhibitory post-synaptic potentials (cIPSPs) originating from a syncytium of gap-junction-connected parvalbumin-positive (PV^+) interneurons (Rainnie, 1999; Paré & Popescu, 2011; Ryan et al., 2012; Schwartzkroin & Knowles, 1984). These compound IPSPs engender membrane potential oscillations (MPOs) and synchronize spike-timing (Ryan et al., 2012). However, parvalbumin expression is not found in the amygdala before postnatal day (P)14, and does not reach mature levels for another two weeks. Moreover, the perisomatic PV^+ synapses, which are believed to produce the cIPSPs, are first observed around P17 and continue to develop into adulthood (Berdel & Morys, 2000). As a result, little is known about the ability of compound IPSPs to engender MPOs or enhance spike-timing in developing BLA principal neurons.

Furthermore, the MPOs we have observed in BLA principal neurons are subject to modulation by intracellular adenylyl cyclase activity; previous experiments (see **Chapter 2**) have demonstrated that the application of forskolin leads to enhancement of

MPOs. Since adenylyl cyclase activity can be modulated by numerous neurotransmitter systems, it is likely that endogenous neuromodulators use this pathway to modulate the oscillatory activity of BLA principal neurons. Notably, activation of β-adrenergic receptors has been shown to be critically involved in the formation of fear memories, and may do so partially through coupling through $G_{\alpha s}$ and adenylyl cyclase to modulate MPOs in the BLA (Gallagher et al., 1977; Galvez et al., 1996; Roozendaal et al., 2008). Moreover, the noradrenergic neurotransmitter system matures substantially over the first month of postnatal development, suggesting that β-adrenergic receptor modulation of MPOs may also change across development (Weiner & Ganon, 1972; Marshall et al., 1991; Liu et al., 1993). Nothing is known, however, about the role of the noradrenergic system in modulating MPOs, or how this may evolve during postnatal development.

We have elucidated and discussed some of the basic oscillatory tendencies of BLA principal neurons in Chapter 3, but many questions still remain. Here we will continue this line of questioning, examining the pharmacological modulation of membrane potential oscillations in BLA principal neurons along with their interaction with compound IPSPs. Specifically, we will utilize isoproterenol, a β-adrenergic receptor agonist, to evaluate whether β-adrenergic receptor activation enhances the propensity of BLA principal neurons to oscillate, and whether this changes throughout development.

Methods

Ethical approval

All experimental procedures strictly conform to guidelines set by the National Institutes of Health and were approved by the Institutional Animal Care and Use Committee at Emory University.

Animals

Male rats born in-house to time-mated, outbred Sprague–Dawley female rats (embryonic day 14 on arrival from Charles River, Wilmington, MA, USA) were used in all

experiments. Pups were housed with the dam prior to weaning on postnatal day (P)22 or P23 (considering P1 as day of birth). After weaning, rats were isolated by sex and housed three to four per cage with access to soft food, dry food, and water *ad libitum*. Animals attributed to each developmental time-point (P14, P21, and P28) were used on that day or the following day (P14–15, P21–22, and P28–29, respectively).

Slice Preparation

*Acute brain s*lices containing the BLA were obtained as previously described (Rainnie, 1999). Briefly, animals were decapitated under isoflurane anesthesia (Fisher Scientific, Hanoverpark, IL, USA) if older than 11 days, and the brains rapidly removed and immersed in ice cold, 95% oxygen–5% carbon dioxide-perfused 'cutting solution' with the following composition (in mM): NaCl (130), $NaHCO_3$ (30), KCl (3.50), KH_2PO4 (1.10), $MgCl_2$ (6.0), $CaCl_2$ (1.0), glucose (10), ascorbate (0.4), thiourea (0.8), sodium pyruvate (2.0) and kynurenic acid (2.0). Coronal slices containing the BLA were cut at a thickness of 300–350 μm using a Leica VTS-1000 vibrating blade microtome (Leica Microsystems Inc., Bannockburn, IL, USA). Slices were kept in oxygenated cutting solution at 32°C for 1 h before transferring to regular artificial cerebrospinal fluid (ACSF) containing (in mM): NaCl (130), $NaHCO_3$ (30), KCl (3.50), KH_2PO_4 (1.10), $MgCl_2$ (1.30), $CaCl_2$ (2.50), glucose (10), ascorbate (0.4), thiourea (0.8) and sodium pyruvate (2.0).

Whole-Cell Patch Clamp Recordings

Individual slices were transferred to a recording chamber mounted on the fixed stage of a Leica DMLFS microscope (Leica Microsystems Inc., Bannockburn, IL, USA) and maintained fully submerged and continuously perfused with oxygenated 32°C ACSF at a flow rate of 1–2 mL min^{-1}. The BLA was identified under 10X magnification. Individual BLA neurons were identified at 40x using differential interference contrast (DIC) optics and infrared (IR) illumination with an IR sensitive CCD camera (Orca ER, Hamamatsu, Tokyo Japan). The location of recorded neurons was chosen randomly

throughout the BLA. Putative principal neurons were selected based on soma size, and their identities were later verified electrophysiologically, as described below. Patch pipettes were pulled from borosilicate glass and had a resistance of 4–6 MΩ. Patch electrode solution had the following composition (in mM): potassium gluconate (130), KCl (2), HEPES (10), $MgCl_2$ (3), K-ATP (2), Na-GTP (0.2), phosphocreatine (5), and 0.35% biocytin, titrated to pH 7.3 with KOH, and 290 mosmol L^{-1}. Data acquisition was performed using either a MultiClamp 700A or an Axopatch 1D amplifier in conjunction with pCLAMP 10.2 software and a DigiData 1322A AD/DA interface (Molecular Devices, Sunnyvale, CA, USA). Whole-cell patch clamp recordings were obtained and low-pass filtered at 2 kHz and digitized at 10 kHz. The membrane potential was held at −60 mV for all neurons if not specified. Cells were excluded if they did not meet the following criteria: a stable resting membrane potential more negative than −55 mV; access resistance lower than 30 MΩ; stable access resistance throughout recording, changing less than 15%; and action potentials crossing 0 mV. BLA principal neurons were distinguished from interneurons, as previously, by their input resistance and spiking pattern in response to injection of a series of 10 hyperpolarizing and depolarizing, 1 s long, square-wave current steps (Ehrlich et al., 2012; Rainnie et al., 2006). Current amplitudes were scaled so that, for each cell, the peak voltage deflections were to approximately −80 mV and −40 mV. Traces were analyzed using Clampfit 10.2 (Molecular Devices, Sunnyvale, CA, USA) and Matlab (Mathworks, Natick, MA, USA).

Drug Application.

Drugs were applied by gravity perfusion at the required concentration in the circulating ACSF. Drugs used: nickel chloride ($NiCl_2$), 500 µM; 4-aminopyridine (4-AP), 100-500 µM; tetrodotoxin (TTX), 1 µM; 6,7-dinitroquinoxaline-2,3-dione (DNQX), 20 µM; RS-CPP, 10 µM; CGP 52432, 2 µM; 4-[1-Hydroxy-2-[(1-methylethyl)amino]ethyl]-1,2-benzenediol hydrochloride (Isoproterenol), 50 µM. All drugs were stored frozen as

concentrated stock solutions in dH_2O except DNQX, which was made in 50% dimethyl sulfoxide and buffered to pH 7.3.

Data Analysis

Data were analyzed by importing the raw voltage and current traces into Matlab (Mathworks, Natick, MA, USA) using scripts provided with sigTOOL (http://sigtool.sourceforge.net/, developed at King's College, London) and processed with customized scripts (available upon request). To characterize neurons in current clamp, first, a series of ten hyperpolarizing and depolarizing, 1 second long, square-wave current steps were injected. They were scaled so that, for each cell, the peak voltage deflections were to approximately -80 mV and -40 mV. Second, linear ramps of depolarizing current were injected, lasting 250 ms and scaled to depolarize the neuron to -35 mV and elicit an action potential within the final 50 ms.

Membrane Properties and Action Potentials

Input resistance and time constant were calculated using the deflection (approx. 5 mV) in response to the smallest, hyperpolarizing current step. Time constant was defined as the time necessary for the cell to reach 63.2% of its maximal deflection; input resistance was calculated as the ratio of peak voltage deflection to the current injected. Action potentials were detected using a heuristic to locate peaks in the second derivative of the membrane potential waveform. The time of the peak was assigned to be the time of spike initiation and the voltage assigned as action potential threshold, which correlated well with visual inspection of the data. Since the sampling rate used here was not fast compared to the frequency of the action potential waveform (10 kHz compared to ~1 kHz), linear interpolation between data points was used to enhance the temporal resolution of measurements of 10-90% rise time, 90-10% decay time, and half-maximal width. These parameters and average action potential waveforms were calculated using spikes collected in the ramp protocol described above.

Resonance and Oscillations

Resonance was assessed by injecting neurons with a ZAP current, a sinusoidal current of fixed amplitude that sweeps logarithmically from 0.1 to 12 Hz over 30 seconds. The amplitude of the current was adjusted to elicit a 20 mV maximal depolarization from a baseline potential of -70 mV. Impedance was calculated as a function of input frequency for each neuron by deriving a power spectrum for the voltage response to the ZAP current, using fast Fourier transforms in the Chronux toolbox for Matlab (Bokil *et al*., 2010), and normalizing it to the power spectrum of the injected current. In order to extract peak values from noisy power spectra and generate averages, the raw impedance traces were fit with a 6^{th} order polynomial. Membrane potential oscillations were also analyzed by means of multi-taper spectral analysis using a custom program that was modified from the Chronux toolbox. Prominence was calculated using power spectra as the proportion of total power in the entire range considered (1-10 Hz) found in a given frequency band (0.1-2, 2-4, 4-6, 6-8, or 8-10 Hz).

Spike Timing Correlation

Spike-timing precision was assessed using a correlation-based metric adapted from Schreiber et al., 2003. The correlation statistic (R_{corr}) was calculated for overlapping windows of 200 ms every 66 ms, using the equation (Equation 5.1) as published. Briefly, spike times from N traces were convolved with a Gaussian filter of pre-determined width (σ) to create spike vectors (*s*). For experiments involving artificial and evoked IPSPs, σ = 6 ms. The degree of correlation between the vectors (s_i, s_j) was calculated using a dot-product normalized to the product of their magnitudes and the number of comparisons being made.

Eq. 5.1

$$R_{corr} = \frac{2}{N(N-1)} \sum_{i=1}^{N} \sum_{j=i+1}^{N} \frac{\vec{s}_i \cdot \vec{s}_j}{\left|\vec{s}_i\right|\left|\vec{s}_j\right|}$$

When calculating spike-timing precision within cells, all 5 traces (N = 6) were compared using this algorithm. Except where stated otherwise, statistical analyses were performed using a two-way Analysis of Variance (ANOVA), with Bonferroni post-tests to compare across windows and conditions. When evaluating drug effects on membrane potential oscillations, statistical comparisons were made using a test previously described by Bokil and colleagues (Bokil et al., 2007) which identifies frequency bands in which two spectral analysis have significantly greater or lesser power.

Results

Whole cell patch clamp recordings were obtained from **58** cells from **35** animals. Animals were distributed across **8** litters and no litter contributed more than **2** recordings to a given experimental protocol at any given time point. All patch clamp recordings began by characterizing the basic electrophysiological properties of the neuron in order to compare to previous data (see **Chapter 3**) and confirm the cellular phenotype was that of BLA principal neurons. Neurons were held at -60 mV with manual DC current injection. Input resistance and membrane time constant were estimated using small (< 5 mV) hyperpolarizing voltage deflections elicited by a square-wave current injection. No measurements were made at P7 in this study; our previous studies suggest that the synaptic and intrinsic physiology of the neurons is too immature to observe compound IPSPs. Because the effect of age on input resistance and membrane time constant was large, variances were generally not equal among groups, and so non-parametric statistical analyses were used. As previously reported, we observed a significant reduction in input resistance (**Figure 5.1A**; overall effect $P < 0.001$, Kruskal-Wallis, $\chi2(2) = 30.72$) and membrane time constant (**Figure 5.1B**; overall effect $P < 0.001$, Kruskal-Wallis, $\chi2(2) = 24.15$) between P14 and P28. Specifically, input resistance decreased significantly from a median value of 117.2 MΩ at P14 almost two-fold to 61.7 MΩ at P21

and 62.10 MΩ at P28. Membrane time constant decreased significantly from a median of 22.95 ms at P14 to 16.2 ms at P21 and 16.0 ms by P28.

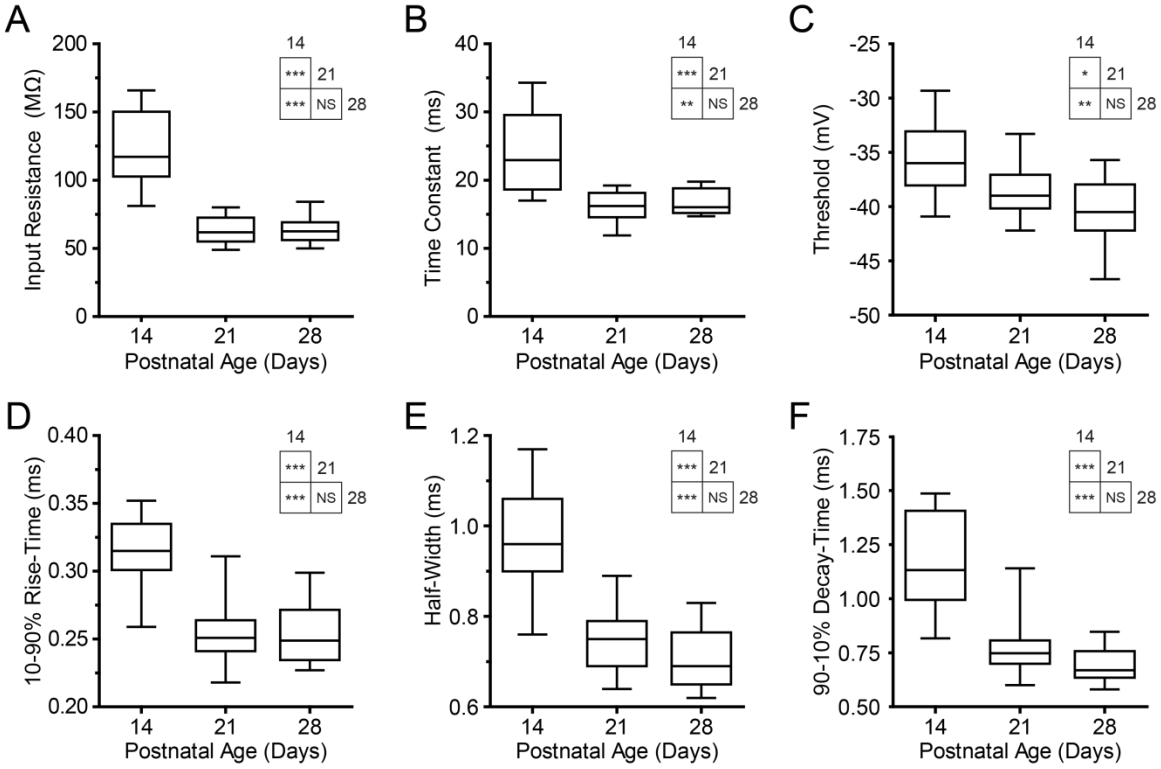

Figure 5.1**: **Physiological profile of recorded neurons is consistent with previous reports**. (A-F) Box and whisker plots display input resistance (A), time constant of charging (B), action potential threshold (C), 10-90% rise time (D), half-width (E), and 90-10% decay time for neurons at each developmental age (n = 17 (P14), n = 18 (P21), n = 11 (P28)). Significance was assessed with Kruskal-Wallis rank-sum test and pairwise comparisons were made for each age using Dunn's posthoc test - see inset tables for results (, P < 0.001; ** P < 0.01; * P < 0.05).*

Characteristics of action potential waveform were also measured in order to compare with previous values. Action potential threshold hyperpolarized significantly from a median value of -36 mV at P14 to -39 mV at P21 and -40.5 by P28 (**Figure 5.1C**; overall effect P < 0.01, Kruskal-Wallis, $\chi 2(2) = 13.73$). Action potential 10-90% rise-time

exhibited a median value of 0.32 ms at P14, which was significantly reduced to 0.25 ms at P21 and P28 (**Figure 5.1D**; overall effect $P < 0.001$, Kruskal-Wallis, $\chi2(2) = 25.24$). The half-width of action potentials was measured to have a median of 0.96 ms in P14 neurons, and decreased significantly to 0.75 ms at P21 and 0.69 ms by P28 (**Figure 5.1E**; overall effect $P < 0.001$, Kruskal-Wallis, $\chi2(2) = 29.04$). Finally, action potential 90-10% decay time decreased significantly from a median value of 1.15 ms at P14 to 0.76 ms at P21 and 0.68 ms by P28 (**Figure 5.1F**; overall effect $P < 0.001$, Kruskal-Wallis, $\chi2(2) = 30.58$). Each of these trends is consistent with those previously reported. Having satisfactorily confirmed that we were recording from principal neurons of the BLA, we next examined the postnatal development of the interaction between compound IPSPs and spike-timing precision.

Spike-timing across development

Using the same protocols shown in Chapter 2, we next sought to quantify the nature of spike-timing precision within single neurons and its interactions with compound IPSPs across development from P14 to P28. To establish the baseline tendency towards precise spike-timing in an individual neuron, square steps of current are injected to bring the cell to action potential threshold. In all cells, the timing of the first few spikes in this control condition is very consistent. However, as successive trains are generated, the later spikes in each train occur with less consistent timing. Using a correlation-based metric, we assessed the spike-timing precision of six sweeps recorded in a single neuron at postnatal ages P14, P21, and P28 (Control; **Figure 5.2A_1-C_1**). At all ages, the correlation metric was at its peak value at the start of the trace, where spike-timing was visibly at its most precise. In P14 neurons, the correlation value started at 0.60 ± 0.10, and diminished to 0.11 ± 0.08 within 500 ms. At P21, the correlation value was 0.59 ± 0.12 at the start of the trace, and had diminished to 0.14 ± 0.07 within 500 ms. By P28,

the correlation value had an initial value of 0.55 ± 0.12, and had reduced to only 0.19 ± 0.08 within 500 ms.

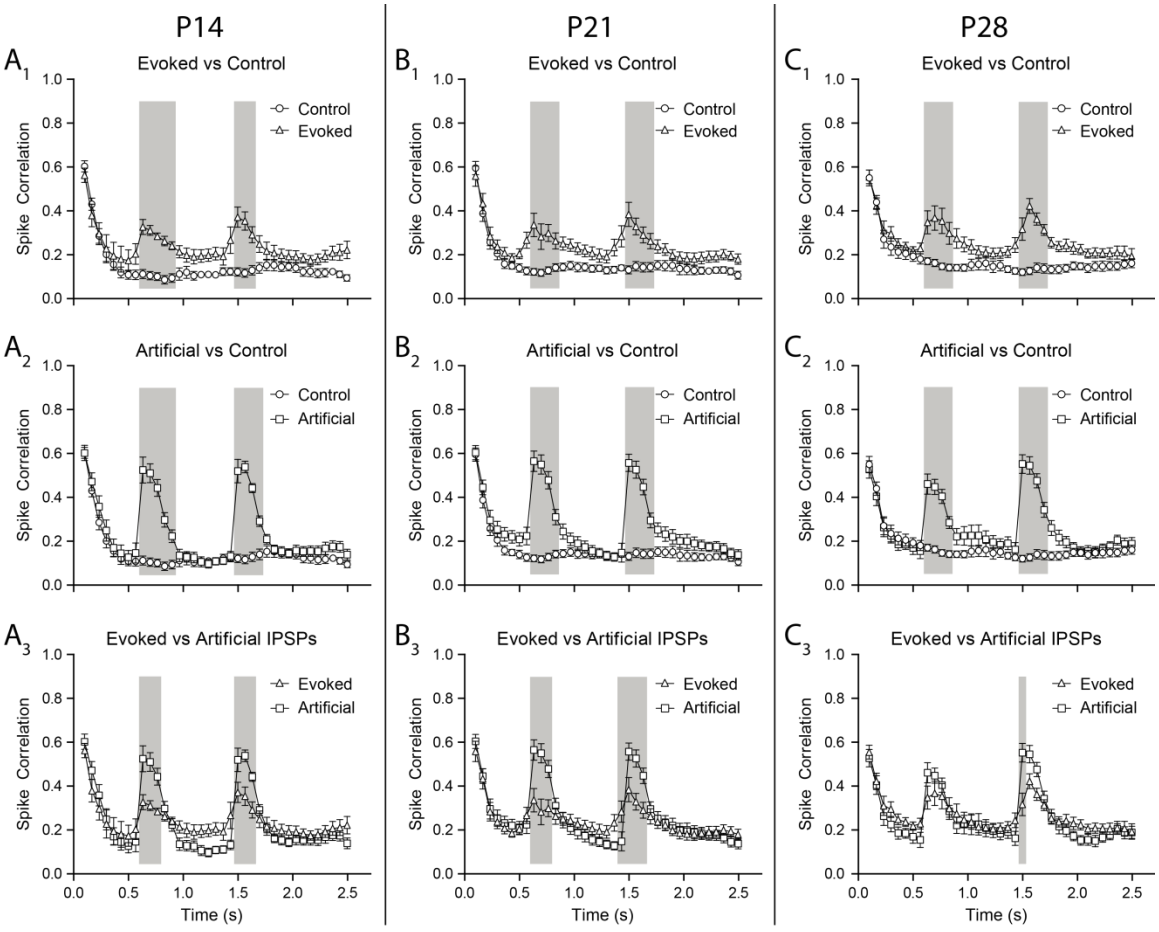

***Figure 5.2**: **Artificial and evoked IPSPs significantly enhance spike-timing precision as early as P14**. (A1-C3) Comparisons of spike-timing reliability between traces with no IPSPs (Control, n = 15), evoked IPSPs (n = 9) and artificial IPSPs (n = 15) assessed with a metric of spike-timing correlation (see Methods) and plotted as mean ± STD. Comparisons made with two-way ANOVA and windows of significant difference are shown with grey boxes.*

Next, we evaluated the effect on spike-timing precision of stimulus-evoked isolated IPSPs (**Figure 5.2A_1-C_1)** and artificial IPSPs produced by injection of negative current across development. Electrical stimulation applied to the dorsal BLA in the

presence of AMPA- and NMDA-type glutamate receptor antagonists and $GABA_B$ receptor antagonists produced a large, fast IPSP which closely resembled the compound IPSPs seen in these slices. As previously observed in adult BLA principal neurons, activation of both evoked and artificial IPSPs during a train of action potentials significantly increased spike-timing precision compared to the baseline condition at all ages (P14, **Figure 5.2A$_{1-3}$**, Two-way ANOVA, effect of group: $F_{(2,1368)} = 120.1$, $P < 0.001$; P21, **Figure 5.2B$_{1-3}$**, Two-way ANOVA, effect of group: $F_{(2,1558)} = 149.1$, $P < 0.001$; P28, **Figure 5.2C$_{1-3}$**, effect of group: $F_{(2,1102)} = 114$, $P < 0.001$). This increase in spike-timing precision lasted for between 270 and 340 ms (P14, effect of interaction: $F_{(74,1368)} = 5.58$, $P < 0.001$; P21, effect of interaction: $F_{(74,1558)} = 5.46$, $P < 0.001$; P28, effect of interaction: $F_{(74,1102)} = 4.47$, $P < 0.001$), and the duration of the affect did not seem to vary with age. Artificial IPSPs produced a significantly greater effect on spike-timing precision than did evoked IPSPs, as illustrated in **Figure 5.2A$_3$-C$_3$**. Overall, age is not a significant factor determining the ability of IPSPs to coordinate activity.

Membrane potential oscillations and resonance frequency

Our final objective was to explore the development of resonant and oscillatory properties of BLA principal neurons in more detail. Resonance frequency was assessed by injection of a ZAP current - a sinusoidal current which is fixed in amplitude, but varies in frequency. Average membrane potential responses to this current are shown in **Figure 5.3**. Resonance was assessed initially in the presence of TTX to prevent Na+ spikes and post-synaptic potentials from interfering with the measurement. In previous studies in adult principal neurons, we have explored the modulation of resonance using a mixture of TTX, 4-AP, and forskolin, a direct activator of adenylyl cyclase, and have shown that elevated adenylyl cyclase activity leads to enhanced resonance. Because of the critical role of β-adrenergic receptor activation in fear memory formation, here we elected to use isoproterenol, a non-selective β-adrenergic receptor agonist, to explore

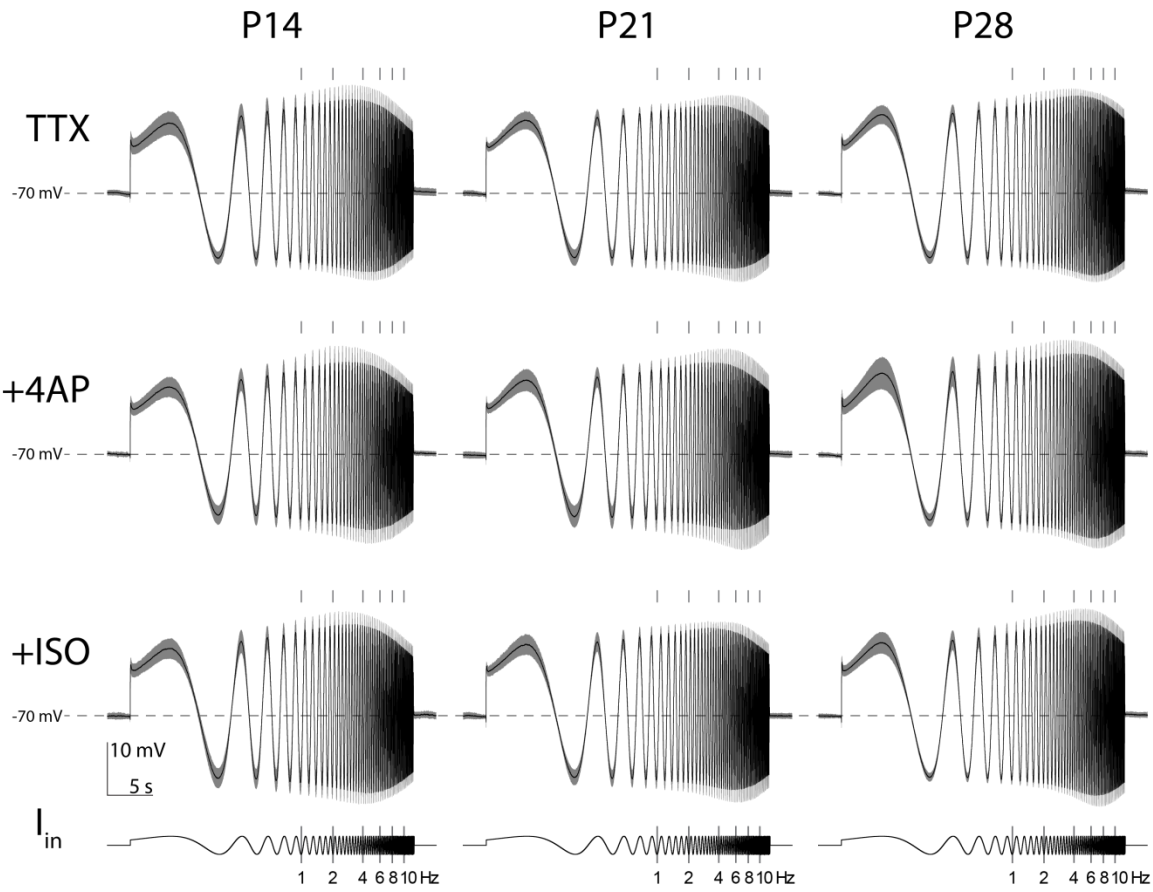

***Figure 5.3**: **Intrinsic resonance frequency matures with age but is unaffected by activation of β receptors**. Membrane potential response, shown as mean ± standard deviation, to the injection of a ZAP current (I_{in}, shown at the bottom, a sinusoid with a fixed amplitude and logarithmically increasing frequency) is depicted for each age (Columns) and for each drug condition (Rows; TTX, TTX+4-AP, TTX+4-AP+Isoproterenol). P7, n = 9; P14, n = 9; P21, n = 11.*

the role of more physiologically relevant endogenous neuromodulatory systems. There was a consistent trend of increasing resonance frequency with age, but the effect was not significant (**Figure 5.4**; Kruskal-Wallis, overall effect: $\chi 2(2) = 5.37$, $P > 0.05$). Moreover, no effect was observed on the amplitude or peak frequency of resonance as a result of treatment with 4-AP or isoproterenol (**Figure 5.4B**). We also performed a

prominence analysis on resonance traces to evaluate whether the width of resonance peaks had changed with drug application, and found no significant effects or trends (**Figure 5.5**).

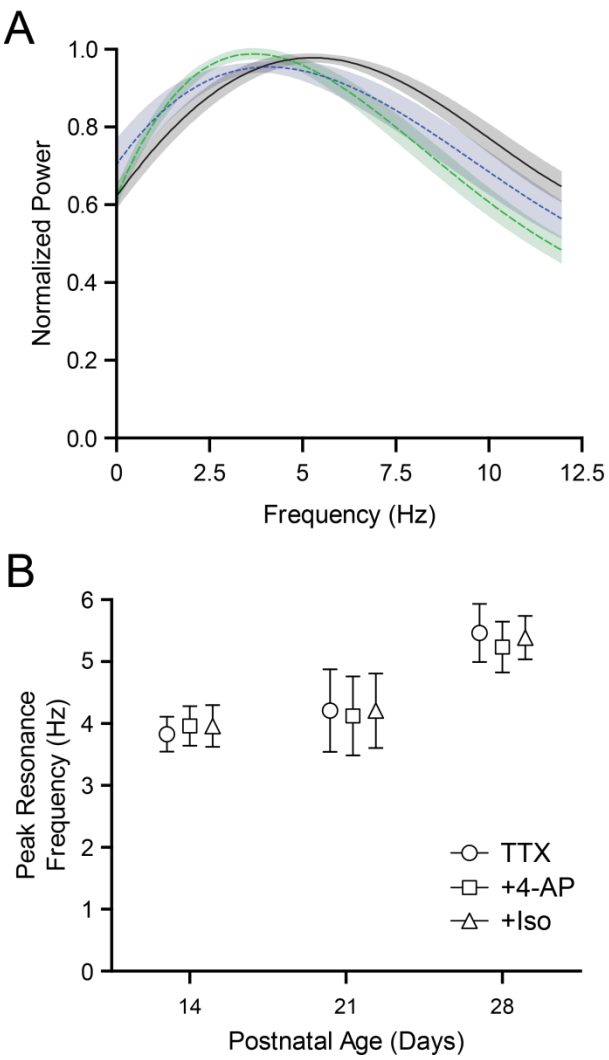

***Figure 5.4**: **Intrinsic resonance is unaffected by pharmacological manipulations**. Normalized power spectra (A) are similar to those observed previously, and show an appropriate trend with respect to age. Peak resonance frequency was calculated for each age and drug condition (B) and shows no affect of pharmacological manipulation.*

BLA principal neurons have been reported to exhibit long-lasting membrane potential oscillations mediated by many of the same currents responsible for establishing the resonance frequency (Pape et al., 1998; Pape & Driesang, 1998; **Chapter 2**; Hutcheon et al., 1996a,b; Hutcheon et al., 1994). The fact that BLA neurons express a similar resonance frequency across development raised the question of whether they may also express similar membrane potential oscillations (MPOs) across development.

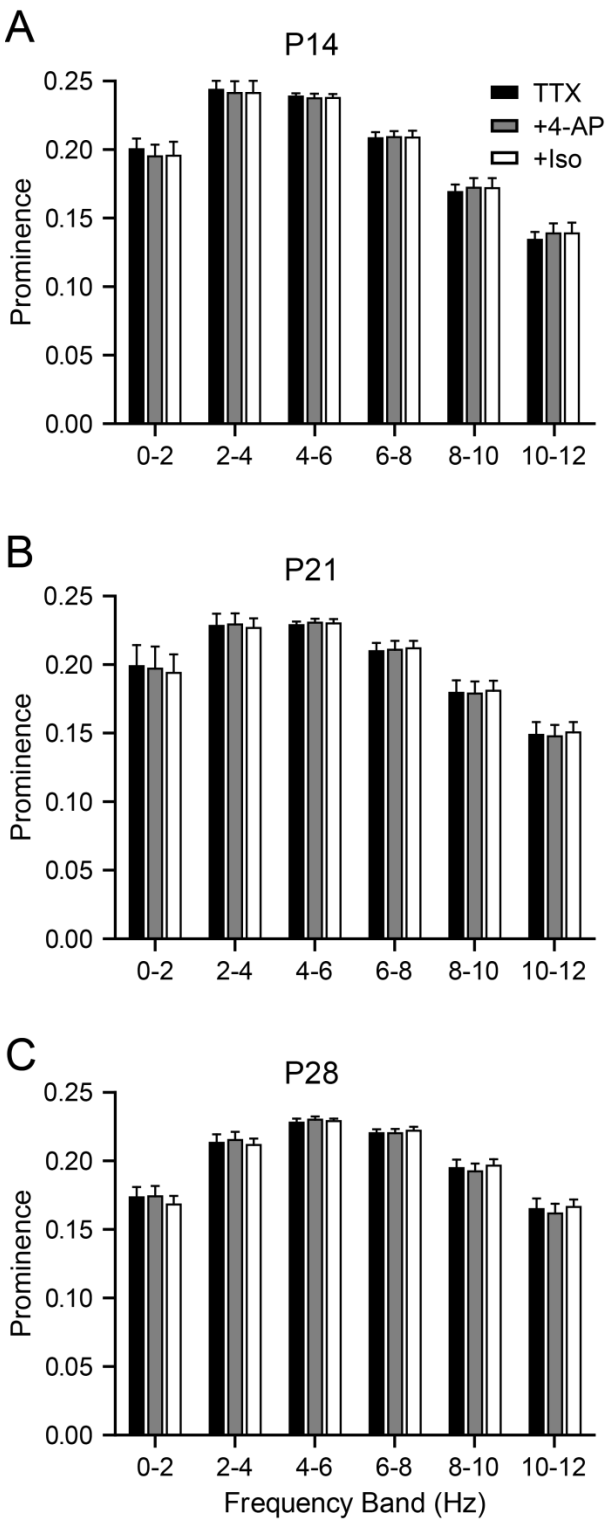

***Figure 5.5**: **Resonance frequency shows no tuning with drug application as measured by prominence.** (A-C) Prominence analysis of resonance traces shown in Figure 3 illustrates that prominence in each frequency band matures with post-natal age, but the peak prominence is unaffected by age or drug condition.*

MPOs were induced by injecting a pulse of current which depolarized the cell to between -35 and -30 mV. Representative traces from each age and condition are

shown in **Figures 5.6-5.8.** At P14, the oscillations induced by depolarization were minimal, and injection of artificial IPSPs into the depolarizing pulse resulted in only a small overshoot on repolarization (**Figure 5.6**). Application of 4-AP enhanced the amplitude of the overshoot, and the combination of 4-AP and isoproterenol brought out a small but defined MPO in 6/9 cells. At P21, in the baseline TTX condition, the overshoot after the artificial IPSPs was already noticeably larger (**Figure 5.7**).

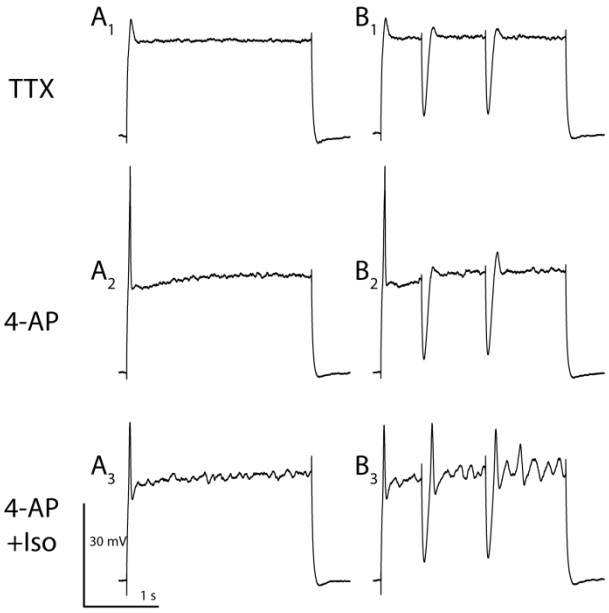

***Figure 5.6**: **Membrane potential oscillations can be observed at P14**. (A$_1$-A$_3$) Traces with no IPSPs injected show very little oscillatory activity, while traces with two IPSPs injected (B$_1$-B$_3$) do show some oscillatory activity in 4-AP + Isoproterenol.*

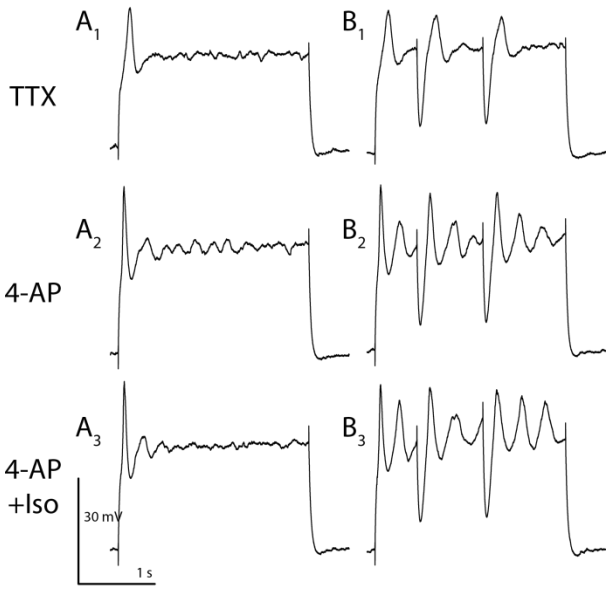

***Figure 5.7**: **Membrane potential oscillations are enhanced by P21**. Relative to P14, P21 shows more oscillations without IPSPs (A$_1$-A$_3$) and more enhancement of oscillations by injection of IPSPs (B$_1$-B$_3$).*

Prominent oscillations were already visible in the presence of 4-AP, and noticeably enhanced with the addition of isoproterenol in 7/9 cells, but only a small, damped oscillation was visible without the injection of IPSPs. By P28, a similar damped oscillation was already visible in the baseline TTX condition, and strongly enhanced by the injection of IPSPs 8/11. Application of 4-AP and, subsequently, isoproterenol strongly enhanced the oscillations visibly more than at either P14 or P21. At each age, comparisons were made using a test previously described by Bokil and colleagues (2007) which identifies frequency bands in which two spectral analysis have significantly greater or lesser power. At all ages, the Bokil test revealed that application of 4-AP and isoproterenol significantly increased spectral power in traces with no IPSPs (comparison made to content present in TTX condition) from 2 to 6 Hz in 56% of cells, and from 6-10 Hz in 78% of cells. Injection of IPSPs resulted in a more specific increase in spectral power, from 4-8 Hz in 78% of cells.

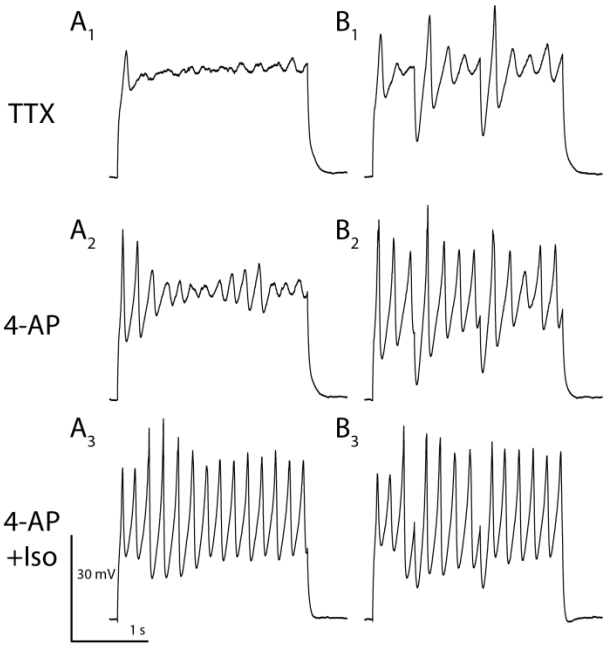

***Figure 5.8**: **Membrane potential oscillations observed at P28 are comparable to those seen in adults**. Even without injection of IPSPs (A_1-A_3), substantial MPOs can be seen with 4-AP and Isoproterenol on the slice. Injection of IPSPs (B_1-B_3) enhance these even further, particularly visible in B_1-B_2.*

Interestingly, similar to the observations above regarding spike-timing precision, injection of IPSPs seems to organize the MPOs. Figure 5.9 shows examples of the MPO protocol from cells at P14 (**Figure 5.9A_1-B_1**) and P28 (**Figure 5.9A_2-B_2**) in which multiple sweeps of the protocol are superimposed. At both ages, MPOs are synchronous towards the beginning of the trace and quickly become disorganized (**5.9A_1-A_2**); however, injection of IPSPs appears to organize the timing of oscillations at P28 (**5.9B_2**) but not P14 (**5.9B_1**).

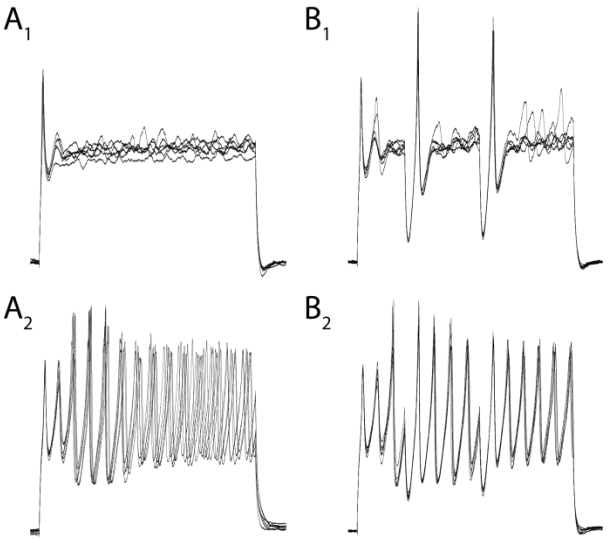

***Figure 5.9**: **IPSPs organize the MPOs observed in P28 animals**. Multiple sweeps are superimposed on one another from cells recorded at P14 (A1 & B1) and P28 (A2 & B2). Artificial IPSPs injected into the depolarizing pulse are able to organize the phase of high-amplitude MPOs observed at P28, but not the low-amplitude ones observed at P14.*

Discussion

This study has provided the first detailed exploration of the development of spike timing precision and membrane potential oscillations in BLA principal neurons. We have shown that, as previously reported in the adult rat, compound IPSPs are able to organize spike-timing as early as P14 (Ryan et al., 2012). Furthermore, we have demonstrated that BLA principal neurons are able to express membrane potential oscillations (MPOs) as early at P14 and that, as in the adult, these oscillations can be triggered by the

injection of artificial cIPSPs. Finally, we have also shown that these MPOs can be modulated by activation of β adrenergic receptors, and that the effects of β adrenergic receptor activation increases across development.

Compound IPSPs can enhance spike-timing precision throughout juvenile development

Both evoked and artificial IPSPs were capable of improving spike-timing precision at all ages examined. It is worth pointing out that artificial IPSPs were more effective than evoked IPSPs at every age, as seen previously in the adult system (Ryan et al., 2012; **Chapter 2**); however, at P28, the window within which the artificial IPSPs were significantly more effective was much smaller than at other ages. This is likely at least in part a result of the evoked IPSPs increasing in effectiveness throughout postnatal development, which may be related to the maturation of inhibitory synaptic transmission (Ehrlich et al., 2013). The diminished relative effectiveness at P28 may also be related to the non-linearity of fear maturation during the juvenile and adolescent periods (Hartley & Lee, 2014).

Since synchronized, compound IPSPs are not typically observed in all recorded slices, it is difficult to estimate their prevalence in developmental tissue. Furthermore, it is unclear to what extent the gap junctions which connect PV^+ interneurons are expressed across development. One study performed in the locus coeruleus found different developmental expression patterns for different subtypes of connexin, the protein responsible for forming gap junctions (Van Bockstaele et al., 2004). For these reasons, it is not yet clear to what extent synchronized, compound IPSPs organize spike-timing in the intact animal, but it seems clear that the basic mechanisms necessary to do so are present early in postnatal development. Future studies looking to further characterize this feature should start earlier in order to find the onset of this capability.

MPOs are modulated by β adrenoceptors throughout juvenile development

We have also shown that MPOs can be observed at all postnatal ages examined using similar pharmacological manipulations to those used previously to characterize the adult system, but that this manipulation results in much larger and more organized MPOs in older animals. Importantly, in this study we showed that activation of β adrenoceptors can lead to enhanced expression of MPOs. This finding merits significant further study, as β adrenergic activation has long been known to be involved in various forms of fear memory formation in the BLA (Roozendaal et al., 2006). This new evidence suggests that enhancement of low-theta-frequency oscillations in the BLA, themselves tightly linked to fear memory formation, is a likely candidate for the mechanism by which β adrenergic receptor activation promotes fear memory formation.

The measurements of neuronal resonance presented here failed to replicate observations discussed in earlier chapters; in **Chapter 2** we reported a significant increase in resonance amplitude in response to 4-AP and forskolin, and in **Chapter 3** we reported a significant effect of age on resonance frequency. Here, we would have expected to observe at least the effects of age and 4-AP on resonance frequency and amplitude, respectively, and hypothesized that we would also see an effect of isoproterenol on resonance amplitude, based on the common action of forskolin and isoproterenol through adenylyl cyclase. This inconsistency may be due to the high sensitivity of measurements of resonance to the exact details of how it is measured (Tseng & Nadim, 2010). Measurements made for **Chapter 2** used a different ZAP protocol than those in **Chapters 3** and **5**, and measurements in **Chapter 5** were performed in triplicate and averaged to reduce noise, while those in **Chapter 3** were not. Future studies will incorporate a more rigorous regime for measuring resonance that will hopefully settle these inconsistencies.

We have previously argued that these MPOs are engendered by synchronous compound IPSPs and that this interaction of the IPSP with the MPO enhances spike-timing precision in BLA principal neurons. Our observation here that BLA principal neurons show enhancement of spike-timing precision in response to compound IPSPs as early as P14 at first seems to complicate this argument. It is possible, however, that the low-amplitude MPOs observed at P14 are sufficient to enhance spike-timing. It is also important to note that we are using multiple sweeps of action potential trains in a single neuron as a convenient experimental substitute for simultaneous recordings in multiple neurons. Our previous, more extensive characterization of principal neuron physiology throughout development showed that basic electrophysiological properties are not just different in juvenile animals than in adults, but also far more variable. This inter-neuronal variability could radically affect the ability of compound IPSPs and MPOs to organize the activity of neuronal ensembles. Future studies should re-evaluate our assessment of spike-timing precision here and examine interactions between pairs of cells in juvenile animals.

Preliminary observations were also made suggesting IPSPs are sufficient to reset the phase of ongoing MPOs in older animals, but not in younger ones. Future studies should examine this phase-resetting in more detail, examining phase coherence across pairs of cells or measuring synchronized oscillations through local field potentials while evoking pharmacologically isolated IPSPs. This final data set suggests numerous future directions for study of the developing amygdala. The data presented in this and previous chapters will provide a foundation for future explorations of the developing basolateral amygdala, however, and are a crucial first step towards understanding how perturbations to this developmental process can lead to psychopathology later in life.

Chapter 6

Summary & Future Directions

The preceding chapters have outlined an incredibly dynamic program of physiological, morphological, and functional changes in the basolateral amygdala (BLA) over the course of the first postnatal month of rodent development. The highly dynamic nature of this developmental window undoubtedly confers some sensitivity to the system – perturbations early in development can have far-reaching consequences. In the case of the BLA, a brain region involved in social cognition and the formation of emotional memory, perturbations which alter the normal developmental trajectory could lead to the onset of psychiatric disorders later in life.

For this exact reason, in future studies, it will be critically important to identify ways in which early-life experience can modulate the normal developmental program. In each aspect of development, there exists a tension between the genetic program contained in our cells and the effect of environmental and/or experience-dependent cues to determine the eventual phenotype. A deeper understanding of brain development will be necessary for us to understand what kinds of gene x environment interactions can lead to adaptive vs. maladaptive outcomes. We have begun to explore these interactions in our own lab using the valproic acid (VPA) model of autistic spectrum disorders (ASD) (Meador & Loring 2013; Markram et al., 2008). The rodent model mimics the human condition through prenatal exposure to valproic acid, which, in humans, leads to a massively increased incidence of ASD in offspring (Meador & Loring 2013). Many studies using this model have been published recently, but so far almost all report differences in the adult offspring, and do not chart the developmental progression of behavioral or molecular deficits (Schneider & Przewlocki, 2004; Rinaldi et al., 2008a,b; Schneider et al., 2001; Ingram et al., 2000; Banerjee et al., 2014). Our own preliminary data, on the other hand, suggests that major changes are observable in the expression of neurotransmitter receptors, innervation by neuromodulators, and animal behavior as early as P7. In order to make true progress understanding how

developmental disorders manifest and, ultimately, how they can be both diagnosed and treated as early as possible, it will be necessary for future studies to directly examine the developmental trajectory throughout juvenile and adolescent development.

Based on the fundamentally different nature of the changes involved, the genetic programs involved in transitioning an animal through adolescence are likely to be largely non-overlapping with the ones necessary to transition them from birth to the beginning of adolescence. These adolescent programs will have their own natural time course and their own environmental susceptibilities, and the adolescent period may include the onset of even more psychiatric disorders than the juvenile period. For example, autistic spectrum disorders are often observed very early in development (DSM-5), whereas schizophrenia and depression are more commonly observed in adolescence (Liu et al., 2013; Kessler et al., 2005). Consequently, future studies must address the nature of the physiological developments taking place during adolescent development, which will undoubtedly be more subtle by simple virtue of occurring in a later stage of development. Indeed, many of the parameters observed in the preceding studies were highly dynamic during the first month of rodent development, but had stabilized by the beginning of adolescence, and strong evidence suggests many of these parameters remain relatively stable throughout adulthood. We must therefore examine other parameters to find those that are dynamic during adolescent development, as these may determine critical periods of adolescent development and be involved in sensitivity to the development of adolescent-onset psychiatric illness.

Among the many interesting aspects of development outside the scope of this study is the development of sexual dimorphism. The amygdala and related structures are sexually dimorphic in adults, but the physiological correlates of this and the developmental timeline thereof are unknown. One might expect that sexual dimorphism would emerge in the adolescent growth period directly following the juvenile period

covered in many of our studies here; indeed, many of the most obvious dimorphisms are likely triggered by the gonadal hormones which are highly expressed by adolescents and adults, but not by juveniles. Recent evidence, however, suggests that sexual dimorphism can be detected at the level of neuronal morphology in rodents during embryonic development (Carrer & Cambiasso, 2002), well before gonadal hormone levels are elevated. I would hypothesize, therefore, that in future studies examining sexual dimorphism, careful observation might detect dimorphic aspects of BLA development at least as early as the first postnatal month. It is interesting to note, however, that our own examination of intrinsic physiology (**Chapter 3**) revealed no sex differences in those measures. Future studies, therefore, should pursue the possibility of sexual dimorphism in neuronal morphology or synaptic physiology.

Additionally, a careful examination of the data presented here, in the context of literature on the development of BLA-dependent behaviors, presents some interesting correlations. The most notable example would be the development of fear-learning behavior – work by Haroutunian and colleagues originally showed that, prior to postnatal day 10, rodent pups were incapable of learning an odor aversion paradigm (Haroutunian & Campbell, 1979). Later work by Thompson, Sullivan and colleagues demonstrated that this transition in BLA-dependent emotional learning around P10 appeared to be concomitant with a transition in synaptic plasticity in the BLA (Thompson et al., 2008). It is interesting to note that, in our own data set, this exact window of development is when the first emergence of dendritic spines is observed on BLA principal neurons. The structure of dendritic spines is believed to be a critical substrate for the formation of long-term memory, and so it is no surprise, in retrospect, that the development of this morphological feature would precede or accompany the expression of learning.

Finally, the data presented in **Chapter 5** is particularly exciting, indicating a likely endogenous mechanism for the modulation of oscillatory properties of BLA principal

neurons. Recent work suggests that, when presented with emotionally salient sensory stimuli, a small subset of BLA principal neurons will spontaneously organize into a cellular assembly to process the input into memory (Josselyn et al., 2001, 2004). We have hypothesized above that MPOs may be a part of the mechanism that determines which neurons are selected for inclusion into this memory engram. Our new data suggests that modulation of oscillatory properties by noradrenaline may be an important part of that process. Further study will be necessary to map out noradrenaline's role in the formation of fear memory in more detail, and these experiments will be the foundation of that work.

Abbreviations

4-AP, 4-aminopyridine
aCSF, artificial cerebrospinal fluid
AHP, afterhyperpolarization
AMPA, α-Amino-3-hydroxy-5-methyl-4-isoxazolepropionic acid
ANOVA, analysis of variance
BLA, basolateral amygdala
cAMP, cyclic adenosine monophosphate
cIPSP, compound inhibitory postsynaptic potential
CNQX, 6-cyano-7-nitroquinoxaline-2,3-dione
D1, Dopamine receptor
DNQX, 6,7-Dinitroquinoxaline-2,3-dione
E#, embryonic day #
fAHP, fast AHP
FFT, fast fourier transform
GABA, γ-amino-butyric-acid
Hz, Hertz
IA, A-current
IH, H-current, hyperpolarization-activated mixed cation current
IT, T-current, transiently active Calcium current
IPSC, Inhibitory post-synaptic current
IPSP, Inhibitory post-synaptic potential
ISI, inter-spike interval
LFP, local field potential
mAHP, medium AHP

mV, milliVolts
MΩ, MegaOhms
MPO, membrane potential oscillation
NMDA, N-methyl,D-aspartate
NS, not significant
P#, postnatal day #
PBS, Phosphate Buffered Saline
PKA, Protein Kinase A
PV+, Parvalbumin-positive
R_{in}, input resistance
SEM, Standard Error of the Mean
τ_{memb}, membrane time constant
TEA, Tetra-ethyl ammonium
TTX, Tetrodotoxin
µm, micrometers
µM, micromolar

Literature Cited

Adolphs R, Baron-Cohen S, Tranel D (2002) Impaired Recognition of Social Emotions Following Amygdala Damage. *J Cogn Neurosci* **14** (8): 1264–74.

American Psychiatric Association. (2013). Diagnostic and statistical manual of mental disorders: **DSM-5**. Washington, D.C: American Psychiatric Association.

Anderson SA, Classey JD, Conde F, Lund JS & Lewis DA. (1995). Synchronous development of pyramidal neuron dendritic spines and parvalbumin-immunoreactive chandelier neuron axon terminals in layer III of monkey prefrontal cortex. *Neuroscience* **67**, 7-22.

Anderson D, Mehaffey WH, Iftinca M, Rehak R, Engbers JDT, et al. (2010) Regulation of neuronal activity by Cav3-Kv4 channel signaling complexes. *Nat Neurosci* **13**: 333-337.

Baas PW, Lin S (2011) Hooks and Comets: The Story of Microtubule Polarity Orientation in the Neuron. *Dev Neurobiol* **71** (6): 403–18.

Banerjee A, Engineer CT, Sauls BL, Morales AA, Kilgard MP, Ploski JE (2014) Abnormal emotional learning in a rat model of autism exposed to valproic acid in utero. *Front Behav Neurosci* **8**:387

Barnet RC, Hunt PS (2005) Trace and Long-Delay Fear Conditioning in the Developing *Rat. Learn Behav* **33**:437-443.

Barnet RC, Hunt PS (2006) The Expression of Fear-Potentiated Startle During Development: Integration of Learning and Response Systems. *Behav Neurosci* **120**: 861-872.

Bartos M, Vida I, Jonas P (2007) Synaptic mechanisms of synchronized gamma oscillations in inhibitory interneuron networks. *Nat Rev Neurosci* **8**: 45-56.

Bauer EP, Paz R, Pare D (2007) Gamma oscillations coordinate amygdalo-rhinal interactions during learning*. J Neurosci* **27**: 9369-9379.

Bayer SA, Altman J, Russo RJ & Zhang X. (1993). Timetables of neurogenesis in the human brain based on experimentally determined patterns in the rat. *Neurotoxicology* **14**, 83-144.

Beckel-Mitchener A, Greenough WT (2004) Correlates Across the Structural, Functional, and Molecular Phenotypes of Fragile X Syndrome. *Ment Retard Dev Disabil Res Rev* **10** (1): 53–9.

Benchenane K, Peyrache A, Khamassi M, Tierney PL, Gioanni Y, et al. (2010) Coherent theta oscillations and reorganization of spike timing in the hippocampal- prefrontal network upon learning. *Neuron* **66**: 921-936.

Bender RA, Brewster A, Santoro B, Ludwig A, Hofmann F, Biel M & Baram TZ. (2001). Differential and age-dependent expression of hyperpolarization-activated, cyclic nucleotide-gated cation channel isoforms 1-4 suggests evolving roles in the developing rat hippocampus. *Neuroscience* **106**, 689-698.

Berdel B, Moryś J (2000) Expression of calbindin-D28k and Parvalbumin During Development of Rat's Basolateral Amygdaloid Complex. *Int J Dev Neurosci* **18** (6): 501–13.

Berdel B, Morys J & Maciejewska B. (1997a). Neuronal changes in the basolateral complex during development of the amygdala of the rat. *Int J Dev Neurosci* **15**, 755-765.

Berdel B, Morys J, Maciejewska B & Dziewiatkowski J. (1997b). Volume and topographical changes of the basolateral complex during the development of the rat's amygdaloid body. *Folia morphologica* **56**, 1-11.

Boehlen A, Heinemann U & Erchova I. (2010). The range of intrinsic frequencies represented by medial entorhinal cortex stellate cells extends with age. *J Neurosci* **30,** 4585-4589.

Bokil H, Purpura K, Schoffelen JM, Thomson D, Mitra P (2007). Comparing spectra and coherences for groups of unequal size. *J Neurosci Methods* **159**(2):337:45

Bokil H, Andrews P, Kulkarni JE, Mehta S & Mitra PP. (2010). Chronux: a platform for analyzing neural signals. *Journal of neuroscience methods* **192,** 146-151.

Bony G, Szczurkowska J, Tamagno I, Shelly M, Contestabile A, Cancedda L (2013) Non-hyperpolarizing GABAB Receptor Activation Regulates Neuronal Migration and Neurite Growth and Specification by cAMP/LKB1. *Nat Commun* **4**: 1800.

Bourgeois JP, Goldman-Rakic PS & Rakic P. (1994). Synaptogenesis in the prefrontal cortex of rhesus monkeys. *Cereb Cortex* **4,** 78-96.

Bouwmeester H, Smits K, Van Ree JM (2002) Neonatal Development of Projections to the Basolateral Amygdala from Prefrontal and Thalamic Structures in Rat. *J Comp Neurol* **450** (3): 241–55.

Brummelte S, Witte V & Teuchert-Noodt G. (2007). Postnatal development of GABA and calbindin cells and fibers in the prefrontal cortex and basolateral amygdala of gerbils (Meriones unguiculatus). *Int J Dev Neurosci* **25,** 191-200.

Brummelte S, Teuchert-Noodt G (2006) Postnatal Development of Dopamine Innervation in the Amygdala and the Entorhinal Cortex of the Gerbil (Meriones Unguiculatus). *Brain Res* **1125** (1): 9–16.

Burton BG, Economo MN, Lee GJ & White JA. (2008). Development of theta rhythmicity in entorhinal stellate cells of the juvenile rat. *Journal of Neurophysiology* **100,** 3144-3157.

Buzsaki G (1997) Functions for interneuronal nets in the hippocampus. *Can J Physiol Pharmacol* **75**: 508-515.

Calabrese B, Wilson MS, Halpain S (2006) Development and Regulation of Dendritic Spine Synapses. *Physiol* (Bethesda, Md.) **21**: 38–47.

Camp LL, Rudy JW (1988) Changes in the Categorization of Appetitive and Aversive Events During Postnatal Development of the Rat. *Dev Psychobiol* **21**: 25-42.

Campbell BA, Ampuero MX (1985) Dissociation of Autonomic and Behavioral Components of Conditioned Fear During Development in the Rat. *Behav Neurosci* **99**: 1089-1102.

Campeau S, Miserendino MJ, Davis M (1992) Intra-amygdala infusion of the N-methyl-D-aspartate receptor antagonist AP5 blocks acquisition but not expression of fear-potentiated startle to an auditory conditioned stimulus. *Behav Neurosci* **106**: 569-574.

Cancedda L, Fiumelli H, Chen K, Poo M (2007) Excitatory GABA Action Is Essential for Morphological Maturation of Cortical Neurons in Vivo. *J Neurosci* **27** (19): 5224.

Canolty RT, Edwards E, Dalal SS, Soltani M, Nagarajan SS, et al. (2006) High gamma power is phase-locked to theta oscillations in human neocortex. *Science* **313**: 1626-1628.

Canolty RT & Knight RT. (2010). The functional role of cross-frequency coupling. *Trends Cogn Sci* **14,** 506-515.

Carlsen J, Heimer L (1988) The basolateral amygdaloid complex as a cortical-like structure. *Brain Res* **441**: 377-380.

Carrer HF, Cambiasso MJ (2002) Sexual differentiation of the brain: genes, estrogen, and neurotrophic factors. *Cell Mol Neurobiol* **22**(5-6):479-500.

Chareyron LJ, Banta Lavenex P, Amaral DG, Lavenex P (2011) Stereological Analysis of the Rat and Monkey Amygdala. *J Comp Neurol* **519** (16): 3218–39.

Chareyron LJ, Banta Lavenex P, Lavenex P (2012) Postnatal Development of the Amygdala: a Stereological Study in Rats. *J Comp Neurol* **520** (16): 3745–63.

Chhatwal J, Gutman, AR, Maguschak, KA, Bowser, M, Yang, Y, et al. (2009) Functional Interactions between Endocannabinoid and CCK Neurotransmitter Systems May Be Critical for Extinction Learning. *Neuropsychopharmacology* **34**(2): 509-521.

Chung L, Moore SD (2007) Cholecystokinin enhances GABAergic inhibitory transmission in basolateral amygdala. *Neuropeptides* **41**: 453-463.

Cressman VL, Balaban J, Steinfeld S, Shemyakin A, Graham P, Parisot N, Moore H (2010) Prefrontal Cortical Inputs to the Basal Amygdala Undergo Pruning During Late Adolescence in the Rat. *J Comp Neurol* **518** (14): 2693–709.

Cohen J. (1977). Statistical power analysis for the behavioral sciences (revised edition). Academic Press, New York.

Collins DR, Pelletier JG, Pare D (2001) Slow and fast (gamma) neuronal oscillations in the perirhinal cortex and lateral amygdala. *J Neurophysiol* **85**: 1661-1672.

Dan Y, Poo MM (2004) Spike timing-dependent plasticity of neural circuits. *Neuron* **44**: 23-30.

Davila JC, Olmos L, Legaz I, Medina L, Guirado S & Real MA. (2008). Dynamic patterns of colocalization of calbindin, parvalbumin and GABA in subpopulations of mouse basolateral amygdalar cells during development. *J Chem Neuroanat* **35,** 67-76.

Davis M. (2000). The role of the amygdala in conditioned and unconditioned fear and anxiety. In *The Amygdala: A Functional Analysis*, ed. Aggleton JP. Oxford University Press, London.

Davis M, Walker DL, Myers KM (2003) Role of the Amygdala in Fear Extinction Measured with Potentiated Startle. *Ann NY Acad Sci* **985**: 218–32.

Desmaisons D, Vincent JD & Lledo PM. (1999). Control of action potential timing by intrinsic subthreshold oscillations in olfactory bulb output neurons. *J Neurosci* **19,** 10727-10737.

Driesang RB & Pape HC. (2000). Spike doublets in neurons of the lateral amygdala: mechanisms and contribution to rhythmic activity. *Neuroreport* **11,** 1703-1708.

Ehrlich DE, Ryan SJ, Hazra R, Guo JD, Rainnie DG. (2010). Postnatal Development of I(h) Subunit Expression Contributes to Maturation of Intrinsic Resonance Properties in Principal Neurons of the Basolateral Amygdala. In *Society for Neuroscience Annual Meeting*. San Diego, CA.

Ehrlich DE, Ryan SJ, Rainnie DG (2012) Postnatal Development of Electrophysiological Properties of Principal Neurons in the Rat Basolateral Amygdala. *J Physiol* **590** (19): 4819–38.

Ehrlich DE, Ryan SJ, Hazra R, Guo JD, Rainnie DG (2013) Postnatal Maturation of GABAergic Transmission in the Rat Basolateral Amygdala. *J Neurophysiol* **110** (4): 926-41.

Ehrlich I, Humeau Y, Grenier F, Ciocchi S, Herry C & Luthi A. (2009). Amygdala inhibitory circuits and the control of fear memory. *Neuron* **62,** 757-771.

Escobar C, Salas M (1993) Neonatal Undernutrition and Amygdaloid Nuclear Complex Development: An Experimental Study in the Rat. *Exp Neurol* **122** (2): 311–318.

Engel AK, Fries P & Singer W. (2001). Dynamic predictions: oscillations and synchrony in top-down processing. *Nat Rev Neurosci* **2,** 704-716.

Erchova I, Kreck G, Heinemann U & Herz AV. (2004). Dynamics of rat entorhinal cortex layer II and III cells: characteristics of membrane potential resonance at rest predict oscillation properties near threshold. *J Physiol* **560,** 89-110.

Erdfelder, E., Faul, F., & Buchner, A. (1996). GPOWER: A general power analysis program. *Behavior Research Methods, Instruments, & Computers* **28**, 1-11.

Faber ES & Sah P. (2002). Physiological role of calcium-activated potassium currents in the rat lateral amygdala. *J Neurosci* **22,** 1618-1628.

Fujisawa S & Buzsaki G. (2011). A 4 Hz oscillation adaptively synchronizes prefrontal, VTA, and hippocampal activities. *Neuron* **72,** 153-165.

Gallagher M, Kapp BS, Musty RE, Driscoll PA (1977). Memory Formation: evidence for a specific neurochemical system in the amygdala. *Science* **198**(4315):423:5.

Galvez R, Mesches MH, McGaugh JL (1996). Norepinephrine release in the amygdala in response to footshock stimulation. *Neurobiol Learn Mem* **66**(3):253-7.

Gerhardstein BL, Puri TS, Chien AJ, Hosey MM (1999) Identification of the Sites Phosphorylated by Cyclic AMP-Dependent Protein Kinase on the beta2 Subunit of L-Type Voltage-Dependent Calcium Channels. *Biochemistry* **38**: 10361-10370.

Gean PW, Shinnick-Gallagher P (1989) The transient potassium current, the A-current, is involved in spike frequency adaptation in rat amygdala neurons. *Brain Res* **480**: 160-169.

Giesbrecht CJ, Mackay JP, Silveira HB, Urban JH & Colmers WF. (2010). Countervailing modulation of Ih by neuropeptide Y and corticotrophin-releasing factor in basolateral amygdala as a possible mechanism for their effects on stress-related behaviors. *J Neurosci* **30,** 16970-16982.

Gleich O, Strutz J (2002) Age Dependent Changes in the Medial Nucleus of the Trapezoid Body in Gerbils. *Hearing Res* **164** (1-2): 166–78.

Gourley SL, Olevska A, Warren MS, Taylor JR & Koleske AJ. (2012). Arg kinase regulates prefrontal dendritic spine refinement and cocaine-induced plasticity. *J Neurosci* **32,** 2314-2323.

Greba Q, Gifkins A, Kokkinidis L (2001) Inhibition of amygdaloid dopamine D2 receptors impairs emotional learning measured with fear-potentiated startle. *Brain Res* **899**: 218-226.

Guo YY, Liu SB, Cui GB, Ma L, Feng B, Xing JH, Yang Q, Li XQ, Wu YM, Xiong LZ, Zhang W & Zhao MG. (2012). Acute stress induces down-regulation of large-conductance Ca2+-activated potassium channels in the lateral amygdala. *The J Physiol* **590,** 875-886.

Gutfreund Y, yarom Y & Segev I. (1995). Subthreshold oscillations and resonant frequency in guinea-pig cortical neurons: physiology and modelling. *J Physiol* **483 (Pt 3),** 621-640.

Hammack SE, Mania I, Rainnie DG (2007) Differential expression of intrinsic membrane currents in defined cell types of the anterolateral bed nucleus of the stria terminalis. *J Neurophysiol* **98**: 638-656.

Han JH, Kushner SA, Yiu AP, Cole CJ, Matynia A, et al. (2007) Neuronal competition and selection during memory formation. *Science* **316**: 457-460.

Han JH, Kushner SA, Yiu AP, Hsiang HL, Buch T, et al. (2009) Selective erasure of a fear memory. *Science* **323**: 1492-1496.

Haroutunian V, Campbell BA (1979) Emergence of interoceptive and exteroceptive control of behavior in rats. *Science* **205**(4409):927:9.

Hartley CA, Lee FS (2014) Sensitive periods in affective development: nonlinear maturation of fear learning. *Neuropsychopharmacology* **40**(1):50-60

Hasenstaub A, Shu Y, Haider B, Kraushaar U, Duque A, et al. (2005) Inhibitory postsynaptic potentials carry synchronized frequency information in active cortical networks. *Neuron* **47**: 423-435.

Heim C & Nemeroff CB. (2002). Neurobiology of early life stress: clinical studies. *Semin Clin Neuropsychiatry* **7,** 147-159.

Hicks BM, DiRago AC, Iacono WG & McGue M. (2009). Gene-environment interplay in internalizing disorders: consistent findings across six environmental risk factors. *J Child Psychol Psychiatry* **50,** 1309-1317.

Hoffman DA, Johnston D (1998) Downregulation of Transient K+ Channels in Dendrites of Hippocampal CA1 Pyramidal Neurons by Activation of PKA and PKC. *J Neurosci* **18**: 3521-3528.

Hu H, Vervaeke K & Storm JF. (2002). Two forms of electrical resonance at theta frequencies, generated by M-current, h-current and persistent Na+ current in rat hippocampal pyramidal cells. J*o Physiol* **545,** 783-805.

Hubbard DT, Blanchard DC, Yang M, Markham CM, Gervacio A, Chun-I L, Blanchard RJ (2004) Development of Defensive Behavior and Conditioning to Cat Odor in the Rat. *Physiol Behav* **80** (4): 525–30.

Hunt PS, Richardson R, Campbell BA (1994) Delayed Development of Fear-potentiated Startle in Rats. *Behav Neurosci* **108** (1): 69–80.

Hunt PS, Hess MF, Campbell BA (1998) Inhibition of the Expression of Conditioned Cardiac Responses in the Developing Rat. *Devel Psychobiol* **33** (3): 221-33.

Hunt PS (1999) A Further Investigation of the Developmental Emergence of Fear-Potentiated Startle in Rats. *Devel Psychobiol* **34**: 281-291.

Hutcheon B, Miura RM & Puil E. (1996). Models of subthreshold membrane resonance in neocortical neurons. *J Neurophysiol* **76,** 698-714.

Hutcheon B, Miura RM, Puil E (1996) Subthreshold membrane resonance in neocortical neurons. *J Neurophysiol* **76**: 683-697.

Hutcheon B & Yarom Y. (2000). Resonance, oscillation and the intrinsic frequency preferences of neurons. *Trends Neurosci* **23,** 216-222.

Hutcheon B, Miura RM, Yarom Y, Puil E (1994) Low-threshold calcium current and resonance in thalamic neurons: a model of frequency preference. *J Neurophysiol* **71**: 583-594.

Ingram SL, Williams JT (1996) Modulation of the hyperpolarization-activated current (Ih) by cyclic nucleotides in guinea-pig primary afferent neurons. *J Physiol* **492**: 97-106.

Ingram JL, Peckham SM, Tisdale B, Rodier PM (2000) Prenatal exposure of rats to valproic acid reproduces the cerebellar anomalies associated with autism. *Neurotoxicol Teratol* **22**(3):319:24.

Ito W, Pan BX, Yang C, Thakur S, Morozov A (2009) Enhanced Generalization of Auditory Conditioned Fear in Juvenile Mice. *Learn Mem* **16** (3): 187–92.

Izhikevich EM. (2002). Resonance and selective communication via bursts in neurons having subthreshold oscillations. *Bio Systems* **67,** 95-102.

Jensen O, Colgin LL (2007) Cross-frequency coupling between neuronal oscillations. *Trends Cogn Sci* **11**: 267-269.

Johnson SA, Wang JF, Sun X, McEwen BS, Chattarji S, Young LT (2009) Lithium Treatment Prevents Stress-induced Dendritic Remodeling in the Rodent Amygdala. *Neuroscience* **163** (1): 34–9.

Josselyn SA, Kida S, Silva AJ (2004) Inducible repression of CREB function disrupts amygdala-dependent memory. *Neurobiol Learn Mem* **82**: 159-163.

Josselyn SA, Nguyen PV (2005) CREB, synapses and memory disorders: past progress and future challenges. *Curr Drug Targets CNS Neurol Disord* **4**: 481-497.

Josselyn SA, Shi C, Carlezon WA, Jr., Neve RL, Nestler EJ, et al. (2001) Long-term memory is facilitated by cAMP response element-binding protein overexpression in the amygdala. *J Neurosci* **21**: 2404-2412.

Jutras MJ, Buffalo EA (2010) Synchronous neural activity and memory formation. *Curr Opin Neurobiol* **20**: 150-155.

Kamp TJ, Hell JW (2000) Regulation of Cardiac L-Type Calcium Channels by Protein Kinase A and Protein Kinase C. *Circ Res* **87**: 1095-1102.

Kanyshkova T, Pawlowski M, Meuth P, Dube C, Bender RA, Brewster AL, Baumann A, Baram TZ, Pape HC & Budde T. (2009). Postnatal expression pattern of HCN channel isoforms in thalamic neurons: relationship to maturation of thalamocortical oscillations. *J Neurosci* **29,** 8847-8857.

Kaufmann WE, Moser HW (2000) Dendritic Anomalies in Disorders Associated with Mental Retardation. *Cereb Cortex* **10** (10): 981–91.

Kessler RC, Berglund P, Demler O, Jin R, Merikangas KR & Walters EE. (2005). Lifetime prevalence and age-of-onset distributions of DSM-IV disorders in the National Comorbidity Survey Replication. *Archives of general psychiatry* **62,** 593-602.

Khurana S, Liu Z, Lewis AS, Rosa K, Chetkovich D & Golding NL. (2012). An essential role for modulation of hyperpolarization-activated current in the development of binaural temporal precision. *J Neurosci* **32,** 2814-2823.

Kida S, Josselyn SA, de Ortiz SP, Kogan JH, Chevere I, et al. (2002) CREB required for the stability of new and reactivated fear memories. *Nat Neurosci* **5**: 348-355.

Kim JH, Richardson R (2007) A Developmental Dissociation in Reinstatement of an Extinguished Fear Response in Rats. *Neurobiol Learn Mem* **88** (1): 48–57.

Kim JH, Richardson R (2008) The Effect of Temporary Amygdala Inactivation on Extinction and Reextinction of Fear in the Developing Rat: Unlearning as a Potential Mechanism for Extinction Early in Development. *J Neurosci* **28** (6): 1282–90.

Kim-Cohen J, Caspi A, Moffitt TE, Harrington HL, Milne BJ, Poulton R (2003) Prior Juvenile Diagnoses in Adults with Mental Disorder: Developmental Follow-back of a Prospective-longitudinal Cohort. *Arch Gen Psych* **60** (7): 709–17.

Kim JH, Hamlin AS & Richardson R. (2009). Fear extinction across development: the involvement of the medial prefrontal cortex as assessed by temporary inactivation and immunohistochemistry. *J Neurosci* **29,** 10802-10808.

Kim J-A, Park J-Y, Kang H-W, Huh S-U, Jeong S-W, et al. (2006) Augmentation of Cav3.2 T-Type Calcium Channel Activity by cAMP-Dependent Protein Kinase A. *J Pharmacol Exp Ther* **318**: 230-237.

King EC, Pattwell SS, Glatt CE, Lee FS (2013) Sensitive Periods in Fear Learning and Memory. *Stress* **17** (1): 13-21.

Koob GF, Volkow ND (2010) Neurocircuitry of Addiction. *Neuropsychopharm* **35** (1): 217–38.

Kraszpulski M, Dickerson PA & Salm AK. (2006). Prenatal stress affects the developmental trajectory of the rat amygdala. *Stress* **9,** 85-95.

Langton JM, Kim JH, Nicholas J, Richardson R (2007) The Effect of the NMDA Receptor Antagonist MK-801 on the Acquisition and Extinction of Learned Fear in the Developing Rat. *Learn Mem* **14**: 665-668.

Lamont EW, Kokkinidis L (1998) Infusion of the dopamine D1 receptor antagonist SCH 23390 into the amygdala blocks fear expression in a potentiated startle paradigm. *Brain Res* **795**: 128-136.

Lampl I & Yarom Y. (1997). Subthreshold oscillations and resonant behavior: two manifestations of the same mechanism. *Neuroscience* **78,** 325-341.

LeDoux J. (2000). The amygdala and emotion: a view through fear. In *The Amygdala: A Functional Analysis*, ed. Aggleton JP. Oxford University Press, London.

LeDoux JE (2007) The Amygdala. *Curr Biol* **17** (20): R868–74.

Lee KF, Soares C, Béïque JC (2012) Examining Form and Function of Dendritic Spines. *Neural Plast* **2012**: 704103.

Lee JH, Gomora JC, Cribbs LL, Perez-Reyes E (1999) Nickel block of three cloned T-type calcium channels: low concentrations selectively block alpha1H. *Biophys J* **77**: 3034-3042.

Lesting J, Narayanan RT, Kluge C, Sangha S, Seidenbecher T & Pape HC. (2011). Patterns of coupled theta activity in amygdala-hippocampal-prefrontal cortical circuits during fear extinction. *PloS One* **6,** e21714.

Lewis DA, Hashimoto T, Volk DW (2005) Cortical inhibitory neurons and schizophrenia. *Nat Rev Neurosci* **6**: 312-324.

Li C, Dabrowska J, Hazra R, Rainnie DG (2011) Synergistic Activation of Dopamine D1 and TrkB Receptors Mediate Gain Control of Synaptic Plasticity in the Basolateral Amygdala. *PloS One* **6** (10): e26065.

Liao CC, Lee LJ (2012) Evidence for Structural and Functional Changes of Subplate Neurons in Developing Rat Barrel Cortex. *Brain Struct Funct* **217** (2): 275–92.

Lin HC, Wang SJ, Luo MZ, Gean PW (2000) Activation of group II metabotropic glutamate receptors induces long-term depression of synaptic transmission in the rat amygdala. *J Neurosci* **20**: 9017-9024.

Lin CH, Lee CC, Huang YC, Wang SJ, Gean PW (2005) Activation of group II metabotropic glutamate receptors induces depotentiation in amygdala slices and reduces fear-potentiated startle in rats. *Learn Mem* **12**: 130-137.

Lisman JE. (1997). Bursts as a unit of neural information: making unreliable synapses reliable. *Trends Neurosci* **20,** 38-43.

Liu Y, Jia W, Strosberg AD, Cynader M (1993). Development and regulation of beta adrenergic receptors in kitten visual cortex: an immunocytochemical and autoradiographic study. *Brain Res* **632**(1-2):274:86

Liu JJ, Norman RM, Manchanda R, De Luca V (2013). Admixture analysis of age at onset in schizophrenia: evidence of three subgroups in a first-episode sample. *Gen Hosp Psychiatry* **35**(6):664-7

Llinas RR, Grace AA & Yarom Y. (1991). In vitro neurons in mammalian cortical layer 4 exhibit intrinsic oscillatory activity in the 10- to 50-Hz frequency range. *Proc Natl Acad Sci U S A* **88,** 897-901.

Loretan K, Bissiere S, Luthi A (2004) Dopaminergic modulation of spontaneous inhibitory network activity in the lateral amygdala. *Neuropharm* **47**: 631-639.

Madsen TE & Rainnie DG. (2009). Local field potentials in the rat basolateral amygdala and medial prefrontal cortex show coherent oscillations in multiple frequency bands during fear. *Society for Neuroscience Annual Meeting, Chicago, IL, Oct 18, 2009*.

Mainen ZF, Sejnowski TJ (1995) Reliability of spike timing in neocortical neurons. *Science* **268**: 1503-1506.

Mainen ZF, Sejnowski TJ (1996) Influence of Dendritic Structure on Firing Pattern in Model Neocortical Neurons. *Nature* **382** (6589): 363–366.

Marcelin B, Liu Z, Chen Y, Lewis AS, Becker A, McClelland S, Chetkovich DM, Migliore M, Baram TZ, Esclapez M & Bernard C. (2012). Dorsoventral differences in intrinsic properties in developing CA1 pyramidal cells. *J Neurosci* **32,** 3736-3747.

Markram K, Rinaldi T, La Mendola D, Sandi C, Markram H (2008) Abnormal fear conditioning and amygdala processing in an animal model of autism. *Neuropsychopharmacology* **33**(4):901-12.

Maren S (2005) Synaptic Mechanisms of Associative Memory in the Amygdala. *Neuron* **47** (6): 783–6.

Marshall KC, Christie MJ, Finlayson PG, Williams JT (1991). Developmental aspects of the locus coeruleus-noradrenaline system. *Prog Brain Res* **88**:173:85.

Mascagni F, McDonald AJ (2003) Immunohistochemical characterization of cholecystokinin containing neurons in the rat basolateral amygdala. *Brain Res* **976**: 171-184.

McCormick DA & Prince DA. (1987). Post-natal development of electrophysiological properties of rat cerebral cortical pyramidal neurones. *J Physiol* **393,** 743-762.

McDonald AJ. (1985). Immunohistochemical identification of gamma-aminobutyric acid-containing neurons in the rat basolateral amygdala. *Neuroscience letters* **53,** 203-207.

McDonald AJ (1998) Cortical Pathways to the Mammalian Amygdala. *Prog Neurobiol* **55** (3): 257–332.

McDonald AJ, Beitz AJ, Larson AA, Kuriyama R, Sellitto C & Madl JE. (1989). Co-localization of glutamate and tubulin in putative excitatory neurons of the hippocampus and amygdala: an immunohistochemical study using monoclonal antibodies. *Neuroscience* **30,** 405-421.

McDonald AJ, Betette RL (2001) Parvalbumin-containing neurons in the rat basolateral amygdala: morphology and co-localization of Calbindin-D(28k). *Neuroscience* **102**: 413-425.

McDonald AJ, Mascagni F (2002) Immunohistochemical characterization of somatostatin containing interneurons in the rat basolateral amygdala. *Brain Res* **943**: 237-244.

McDonald AJ, Mascagni F, Mania I, Rainnie DG (2005) Evidence for a perisomatic innervation of parvalbumin-containing interneurons by individual pyramidal cells in the basolateral amygdala. *Brain Research* **1035**: 32-40.

McDonald AJ, Shammah-Lagnado SJ, Shi C, Davis M (1999) Cortical afferents to the extended amygdala. *Ann N Y Acad Sci* **877**: 309-338.

McEwen BS (2003) Early Life Influences on Life-long Patterns of Behavior and Health. *Ment Retard Dev D R* **9** (3): 149–54.

Meador KJ, Loring DW (2013) Prenatal valproate exposure is associated with autism spectrum disorder and childhood autism. *J Pediatr* **163**(3):924

Miserendino MJ, Sananes CB, Melia KR, Davis M (1990) Blocking of acquisition but not expression of conditioned fear- potentiated startle by NMDA antagonists in the amygdala. *Nature* **345**: 716-718.

Mitra S, Bokil H (2008) Observed brain dynamics. New York: Oxford University Press.

Mizukawa K, Tseng IM, Otsuka N (1989) Quantitative Electron Microscopic Analysis of Postnatal Development of Zinc-positive Nerve Endings in the Rat Amygdala Using Timm's Sulphide Silver Technique. *Brain Res Dev Brain Res* **50** (2): 197–203.

Molineux ML, Fernandez FR, Mehaffey WH, Turner RW (2005) A-Type and T-Type Currents Interact to Produce a Novel Spike Latency-Voltage Relationship in Cerebellar Stellate Cells. *J Neurosci* **25**: 10863-10873.

Monk CS. (2008). The development of emotion-related neural circuitry in health and psychopathology. *Development and psychopathology* **20,** 1231-1250.

Monteiro RA, Henrique RM, Oliveira MH, Silva MW, Rocha E(2005) Postnatal Cerebellar Granule Cells of the White Rat (Rattus Norvegicus): a Quantitative Study, Using Design-based Stereology. *Ann Anat* **187** (2): 161–73.

Monteiro RA, Henrique RM, Rocha E, Marini-Abreu MM, Oliveira MH, Silva MW(1998) Age-related Changes in the Volume of Somata and Organelles of Cerebellar Granule Cells. *Neurobiol Aging* **19** (4): 325–32.

Moriceau S, Roth TL, Okotoghaide T, Sullivan RM (2004) Corticosterone Controls the Developmental Emergence of Fear and Amygdala Function to Predator Odors in Infant Rat Pups. *Int J Dev Neurosci* **22**: 415-422.

Moryś J1, Berdel B, Kowiański P, Dziewiatkowski J(1998) The Pattern of Synaptophysin Changes During the Maturation of the Amygdaloid Body and Hippocampal Hilus in the Rat. *Folia Neuropathol* **36** (1): 15–23.

Moye TB, Rudy JW (1987) Ontogenesis of Trace Conditioning in Young Rats: Dissociation of Associative and Memory Processes. *Dev Psychobiol* **20** (4): 405–14.

Muller JF, Mascagni F, McDonald AJ (2005) Coupled networks of parvalbumin-immunoreactive interneurons in the rat basolateral amygdala. *J Neurosci* **25**: 7366-7376.

Muller JF, Mascagni F, McDonald AJ (2006) Pyramidal cells of the rat basolateral amygdala: synaptology and innervation by parvalbumin-immunoreactive interneurons. *J Comp Neurol* **494**: 635-650.

Muller JF, Mascagni F, McDonald AJ (2009) Dopaminergic Innervation of Pyramidal Cells in the Rat Basolateral Amygdala. *Brain Struct Funct* **213** (3): 275–88.

Muly EC, Mania I, Guo J-D, Rainnie DG (2007) Group II metabotropic glutamate receptors in anxiety circuitry: Correspondence of physiological response and subcellular distribution. *J Comp Neurol* **505**: 682-700.

Muly EC, Senyuz M, Khan ZU, Guo JD, Hazra R, Rainnie DG(2009) Distribution of D1 and D5 Dopamine Receptors in the Primate and Rat Basolateral Amygdala. *Brain Struct Funct* **213** (4-5): 375–93.

Padival MA, Blume SR, Rosenkranz JA (2013) Repeated Restraint Stress Exerts Different Impact on Structure of Neurons in the Lateral and Basal Nuclei of the Amygdala. *Neurosci* **246**: 230–42.

Pape HC & Driesang RB. (1998). Ionic mechanisms of intrinsic oscillations in neurons of the basolateral amygdaloid complex. *J Neurophysiol* **79,** 217-226.

Pape HC, Munsch T, Budde T (2004) Novel vistas of calcium-mediated signalling in the thalamus. *Pflugers Arch* **448**: 131-138.

Pape HC, Narayanan RT, Smid J, Stork O, Seidenbecher T (2005) Theta activity in neurons and networks of the amygdala related to long-term fear memory. *Hippocampus* **15**: 874-880.

Pape HC, Pare D (2010) Plastic Synaptic Networks of the Amygdala for the Acquisition, Expression, and Extinction of Conditioned Fear. *Physiol Rev* **90** (2): 419.

Pape HC, Pare D & Driesang RB. (1998). Two types of intrinsic oscillations in neurons of the lateral and basolateral nuclei of the amygdala. *J Neurophysiol* **79,** 205-216.

Pare D, Collins DR, Pelletier JG (2002) Amygdala oscillations and the consolidation of emotional memories. *Trends Cogn Sci* 6**:** 306-314.

Pare D, Gaudreau H (1996) Projection cells and interneurons of the lateral and basolateral amygdala: distinct firing patterns and differential relation to theta and delta rhythms in conscious cats. *J Neurosci* **16**: 3334-3350.

Pattwell SS, Bath KG, Casey BJ, Ninan I, Lee FS (2011) Selective Early-acquired Fear Memories Undergo Temporary Suppression During Adolescence. *Proc Natl Acad Sci U S A* **108** (3): 1182–7.

Pattwell SS, Duhoux S, Hartley CA, Johnson DC, Jing D, Elliott MD, Ruberry EJ, Powers A, Mehta N, Yang RR, Soliman F, Glatt CE, Casey BJ, Ninan I, Lee FS (2012) Altered Fear Learning Across Development in Both Mouse and Human. *Proc Natl Acad Sci U S A* **109** (40): 16318–23.

Paz R, Bauer EP, Pare D (2008) Theta synchronizes the activity of medial prefrontal neurons during learning. *Learn Mem* **15**: 524-531.

Pelletier JG, Pare D (2004) Role of amygdala oscillations in the consolidation of emotional memories. *Biol Psychiatry* **55**: 559-562.

Pena F, Amuzescu B, Neaga E & Flonta ML. (2006). Thermodynamic properties of hyperpolarization-activated current (Ih) in a subgroup of primary sensory neurons. *Experimental brain research Experimentelle Hirnforschung Experimentation cerebrale* **173,** 282-290.

Penttonen M, Kamondi A, Acsady L, Buzsaki G (1998) Gamma frequency oscillation in the hippocampus of the rat: intracellular analysis in vivo. *Eur J Neurosci* **10**: 718-728.

Perez-Reyes E (2003) Molecular Physiology of Low-Voltage-Activated T-type Calcium Channels. *Physiol Rev* **83**: 117-161.

Person AL, Perkel DJ (2005) Unitary IPSPs Drive Precise Thalamic Spiking in a Circuit Required for Learning. *Neuron* **46**: 129-140.

Pillai AG, de Jong D, Kanatsou S, Krugers H, Knapman A, Heinzmann JM, Holsboer F, Landgraf R, Joëls M, Touma C(2012) Dendritic Morphology of Hippocampal and Amygdalar Neurons in Adolescent Mice Is Resilient to Genetic Differences in Stress Reactivity. *PLoS One* **7** (6): e38971.

Pin JP, Duvoisin R (1995) The metabotropic glutamate receptors: Structure and functions. *Neuropharmacology* **34**: 1-26.

Pine DS. (2002). Brain development and the onset of mood disorders. *Semin Clin Neuropsychiatry* **7,** 223-233.

Pine DS, Cohen P, Gurley D, Brook J, Ma Y(1998) The Risk for Early-adulthood Anxiety and Depressive Disorders in Adolescents with Anxiety and Depressive Disorders. *Arch Gen Psychiatry* **55** (1): 56–64.

Pike FG, Goddard RS, Suckling JM, Ganter P, Kasthuri N, et al. (2000) Distinct frequency preferences of different types of rat hippocampal neurones in response to oscillatory input currents. *J Physiol* **529** Pt 1: 205-213.

Pouille F, Scanziani M (2001) Enforcement of Temporal Fidelity in Pyramidal Cells by Somatic Feed-Forward Inhibition. *Science* **293**: 1159-1163.

Popa D, Duvarci S, Popescu AT, Lena C & Pare D. (2010). Coherent amygdalocortical theta promotes fear memory consolidation during paradoxical sleep. *Proc Natl Acad Sci U S A* **107,** 6516-6519.

Popescu AT, Pare D (2011) Synaptic interactions underlying synchronized inhibition in the basal amygdala: evidence for existence of two types of projection cells. *J Neurophysiol* **105**: 687-696.

Prescott SA & Sejnowski TJ. (2008). Spike-rate coding and spike-time coding are affected oppositely by different adaptation mechanisms. *J Neurosci* **28,** 13649-13661.

Puram SV, Kim AH, Ikeuchi Y, Wilson-Grady JT, Merdes A, Gygi SP, Bonni A (2011) A CaMKIIβ Signaling Pathway at the Centrosome Regulates Dendrite Patterning in the Brain. *Nat Neurosci* **14** (8): 973–83.

Quinn R (2005) Comparing Rat's to Human's Age: How Old Is My Rat in People Years? *Nutrition* **21** (6): 775–7.

Quirk GJ, Repa C, LeDoux JE (1995) Fear conditioning enhances short-latency auditory responses of lateral amygdala neurons: parallel recordings in the freely behaving rat. *Neuron* **15**: 1029-1039.

Raineki C, De Souza MA, Szawka RE, Lutz ML, De Vasconcellos LF, Sanvitto GL, Izquierdo I, Bevilaqua LR, Cammarota M, Lucion AB(2009) Neonatal Handling and the Maternal Odor Preference in Rat Pups: Involvement of Monoamines and Cyclic AMP Response Element-binding Protein Pathway in the Olfactory Bulb. *Neuroscience* **159** (1): 31–8.

Rainnie DG. (1999). Serotonergic modulation of neurotransmission in the rat basolateral amygdala. *J Neurophysiol* **82,** 69-85.

Rainnie DG, Asprodini EK & Shinnick-Gallagher P. (1991a). Excitatory transmission in the basolateral amygdala. *J Neurophysiol* **66,** 986-998.

Rainnie DG, Asprodini EK & Shinnick-Gallagher P. (1991b). Inhibitory transmission in the basolateral amygdala. *J Neurophysiol* **66,** 999-1009.

Rainnie DG, Asprodini EK & Shinnick-Gallagher P. (1993). Intracellular recordings from morphologically identified neurons of the basolateral amygdala. *J Neurophysiol* **69,** 1350-1362.

Rainnie DG, Bergeron R, Sajdyk TJ, Patil M, Gehlert DR, Shekhar A (2004) Corticotrophin Releasing Factor-induced Synaptic Plasticity in the Amygdala Translates Stress into Emotional Disorders. *J Neurosci* **24** (14): 3471–3479.

Rainnie D, Holmes K, Shinnick-Gallagher P (1994) Activation of postsynaptic metabotropic glutamate receptors by trans- ACPD hyperpolarizes neurons of the basolateral amygdala. *J Neurosci* **14**: 7208-7220.

Rainnie DG, Mania I, Mascagni F, McDonald AJ (2006) Physiological and Morphological Characterization of Parvalbumin-Containing Interneurons in the Rat Basolateral Amygdala. *J Comp Neurol* **498** (1): 142-61.

Rainnie DG, Ressler KJ (2009) Physiology of the Amygdala: Implications for PTSD. In: Shiromani P, Keane T, LeDoux JE, editors. Post-Traumatic Stress Disorder: Basic Science and Clinical Practice: Humana Press.

Rakic P. (1995). The development of the frontal lobe. A view from the rear of the brain. *Adv Neurol* **66,** 1-6; discussion 6-8.

Ramadan O, Qu Y, Wadgaonkar R, Baroudi G, Karnabi E, et al. (2009) Phosphorylation of the Consensus Sites of Protein Kinase A on alpha1D L-type Calcium Channel. *Journal of Biological Chemistry* **284**: 5042-5049.

Ramoa AS & McCormick DA. (1994). Developmental changes in electrophysiological properties of LGNd neurons during reorganization of retinogeniculate connections. *J Neurosci* **14,** 2089-2097.

Randall FE, Whittington MA, Cunningham MO (2011) Fast oscillatory activity induced by kainate receptor activation in the rat basolateral amygdala in vitro. *Eur J Neurosci* **33**: 914-922.

Richardson MJ, Brunel N & Hakim V. (2003). From subthreshold to firing-rate resonance. *J Neurophysiol* **89,** 2538-2554.

Richardson R, Paxinos G, Lee J (2000) The Ontogeny of Conditioned Odor Potentiation of Startle. *Behav Neurosci* **114** (6): 1167–73.

Rinaldi T, Silberberg G, Markam H (2008a) Hyperconnectivity of local neocortical microcircuitry induced by prenatal exposure to valproic acid. *Cereb Cortex* **18**(4):763-70.

Rinaldi T, Perrodin C, Markram H (2008b) Hyper-connectivity and hyper-plasticity in the medial prefrontal cortex in the valproic acid animal model of autism. *Front Neural Circuits* **29**:2:4

Robinson RB, Siegelbaum SA (2003) Hyperpolarization-activated cation currents: from molecules to physiological function. *Ann Rev Physiol* **65**: 453-480.

Robbe D, Montgomery SM, Thome A, Rueda-Orozco PE, McNaughton BL, et al. (2006) Cannabinoids reveal importance of spike timing coordination in hippocampal function. *Nat Neurosci* **9**: 1526-1533.

Rodrigues SM, Schafe GE, LeDoux JE (2001) Intra-amygdala blockade of the NR2B subunit of the NMDA receptor disrupts the acquisition but not the expression of fear conditioning. *J Neurosci* **21**: 6889-6896.

Rodrigues SM, Schafe GE, LeDoux JE (2004) Molecular Mechanisms Underlying Emotional Learning and Memory in the Lateral Amygdala. *Neuron* **44** (1): 75–91.

Romand S, Wang Y, Toledo-Rodriguez M, Markram H(2011) Morphological Development of Thick-tufted Layer v Pyramidal Cells in the Rat Somatosensory Cortex. *Front Neuroanat* **5**:5.

Roozendaal B, Hui GK, Hui IR, Berlau DJ, McGaugh JL, Weinberger NM (2006) Basolateral amygdala noradrenergic activity mediates corticosterone-induced enhancement auditory fear conditioning. *Neurobiol Learn Mem* **86**(3):249-55.

Roozendaal B, Castello NA, Vedana G, Barsegyan A, McGuagh JL (2008). Noradrenergic activation of the basolateral amygdala modulates consolidation of object recognition memory. *Neurobiol Learn Mem* **90**(3):576-9.

Roozendaal B, McEwen BS, Chattarji S (2009) Stress, Memory and the Amygdala*. Nat Rev Neurosci* **10** (6): 423–33.

Rubinow MJ, Drogos LL, Juraska JM (2009) Age-related Dendritic Hypertrophy and Sexual Dimorphism in Rat Basolateral Amygdala. *Neurobiol Aging* **30** (1): 137–146.

Rubinow MJ & Juraska JM. (2009). Neuron and glia numbers in the basolateral nucleus of the amygdala from preweaning through old age in male and female rats: a stereological study. *J Comp Neurol* **512,** 717-725.

Rudy B (1988) Diversity and ubiquity of K channels. *Neuroscience* 25: 729-749.

Rudy JW (1993) Contextual Conditioning and Auditory Cue Conditioning Dissociate During Development. *Behav Neurosci* **107** (5): 887–91.

Russier Ml, Carlier E, Ankri N, Fronzaroli L, Debanne D (2003) A-, T-, and H-type Currents Shape Intrinsic Firing of Developing Rat Abducens Motoneurons. *J Physiol* **549**: 21-36.

Ryan SJ, Ehrlich DE, Jasnow AM, Daftary S, Madsen TE, Rainnie DG (2012) Spike-timing Precision and Neuronal Synchrony Are Enhanced by an Interaction Between

Synaptic Inhibition and Membrane Oscillations in the Amygdala. *PloS One* **7** (4): e35320.

Sadler TR, Nguyen PT, Yang J, Givrad TK, Mayer EA, Maarek JM, Hinton DR & Holschneider DP. (2011). Antenatal maternal stress alters functional brain responses in adult offspring during conditioned fear. *Brain Res* **1385,** 163-174.

Sancristobal B, Sancho JM & Garcia-Ojalvo J. (2010). Phase-response approach to firing-rate selectivity in neurons with subthreshold oscillations. *Phys Rev E Stat Nonlin Soft Matter Phys* **82,** 041908.

Sangha S, Narayanan RT, Bergado-Acosta JR, Stork O, Seidenbecher T & Pape HC. (2009). Deficiency of the 65 kDa isoform of glutamic acid decarboxylase impairs extinction of cued but not contextual fear memory. *J Neurosci* **29,** 15713-15720.

Schaefer AT, Angelo K, Spors H, Margrie TW (2006) Neuronal oscillations enhance stimulus discrimination by ensuring action potential precision. *PLoS Biol* **4**: e163.

Schafe GE, Nadel NV, Sullivan GM, Harris A, LeDoux JE (1999) Memory consolidation for contextual and auditory fear conditioning is dependent on protein synthesis, PKA, and MAP kinase. *Learn Mem* **6**: 97-110.

Schneider T, Labuz D, Przewłocki R (2001) Nociceptive changes in rats after prenatal exposure to valproic acid. *Pol J Pharmacol* **53**(5):531-4

Schneider T, Przewłocki R (2005) Behavioral alterations in rats prenatally exposed to vaproic acid: animal model of autism. *Neuropsychopharmacology* **30**(1):80-9.

Schreiber S, Fellous JM, Whitmer D, Tiesinga P, Sejnowski TJ (2003) A new correlation-based measure of spike timing reliability. *Neurocomputing* **52-54**: 925-931.

Schwartzkroin PA, Knowles WD (1984) Intracellular study of human epileptic cortex: in vitro maintenance of epileptiform activity? *Science* **223**(4637):709-12.

Seidel K, Helmeke C, Poeggel G & Braun K. (2008). Repeated neonatal separation stress alters the composition of neurochemically characterized interneuron subpopulations in the rodent dentate gyrus and basolateral amygdala. *Developmental Neurobiology* **68,** 1137-1152.

Seidenbecher T, Laxmi TR, Stork O, Pape HC (2003) Amygdalar and hippocampal theta rhythm synchronization during fear memory retrieval. *Science* **301**: 846-850.

Shekhar A, Truitt W, Rainnie DG, Sajdyk T (2005) Role of Stress, Corticotrophin Releasing Factor (CRF) and Amygdala Plasticity in Chronic Anxiety. *Stress* **8** (4): 209–19.

Shepherd GM (1996) The Dendritic Spine: a Multifunctional Integrative Unit. *J Neurophysiol* **75** (6): 2197–210.

Sinfield JL, Collins DR (2006) Induction of synchronous oscillatory activity in the rat lateral amygdala in vitro is dependent on gap junction activity. *Eur J Neurosci* **24**: 3091-3095.

Singer W. (2009). Distributed processing and temporal codes in neuronal networks. *Cognitive Neurodynamics* **3,** 189-196.

Snead OC, 3rd & Stephens HI. (1983). Ontogeny of cortical and subcortical electroencephalographic events in unrestrained neonatal and infant rats. *Experimental Neurology* **82,** 249-269.

Sohal VS, Pangratz-Fuehrer S, Rudolph U, Huguenard JR (2006) Intrinsic and synaptic dynamics interact to generate emergent patterns of rhythmic bursting in thalamocortical neurons. *J Neurosci* **26**: 4247-4255.

Soltesz I, Deschenes M (1993) Low- and high-frequency membrane potential oscillations during theta activity in CA1 and CA3 pyramidal neurons of the rat hippocampus under ketamine-xylazine anesthesia. *J Neurophysiol* **70**: 97-116.

Spear LP. (2009). Heightened stress responsivity and emotional reactivity during pubertal maturation: Implications for psychopathology. *Development and Psychopathology* **21,** 87-97.

Steinberg L (2005) Cognitive and Affective Development in Adolescence. *Trends Cogn Sci* **9** (2): 69–74.

Storm JF. (1989). An after-hyperpolarization of medium duration in rat hippocampal pyramidal cells. *J Physiol* **409,** 171-190.

Stuber GD, Sparta DR, Stamatakis AM, van Leeuwen WA, Hardjoprajitno JE, Cho S, Tye KM, Kempadoo KA, Zhang F, Deisseroth K, Bonci A(2011) Excitatory Transmission from the Amygdala to Nucleus Accumbens Facilitates Reward Seeking. *Nature* **475** (7356): 377–80.

Sullivan RM, Landers M, Yeaman B, Wilson DA (2000) Good Memories of Bad Events in Infancy. *Nature* **407** (6800): 38–9.

Surges R, Freiman TM & Feuerstein TJ. (2004). Input resistance is voltage dependent due to activation of Ih channels in rat CA1 pyramidal cells. *J Neurosci Res* **76,** 475-480.

Szinyei C, Heinbockel T, Montagne J, Pape HC (2000) Putative cortical and thalamic inputs elicit convergent excitation in a population of GABAergic interneurons of the lateral amygdala. *J Neurosci* **20**: 8909-8915.

Szucs A, Huerta R, Rabinovich MI, Selverston AI (2009) Robust microcircuit synchronization by inhibitory connections. *Neuron* **61**: 439-453.

Takahashi LK (1992) Ontogeny of Behavioral Inhibition Induced by Unfamiliar Adult Male Conspecifics in Preweanling Rats. *Physiol Behav* **52**: 493 – 8.

Thomas CG, Tian H, Diamond JS (2011) The Relative Roles of Diffusion and Uptake in Clearing Synaptically Released Glutamate Change During Early Postnatal Development. *J Neurosci* **31** (12): 4743–54.

Thompson JV, Sullivan RM, Wilson DA (2008) Developmental Emergence of Fear Learning Corresponds with Changes in Amygdala Synaptic Plasticity. *Neuroscience* **1200**: 58-65.

Tohidi V & Nadim F. (2009). Membrane resonance in bursting pacemaker neurons of an oscillatory network is correlated with network frequency. *J Neurosci* **29,** 6427-6435.

Torres-García ME, Solis O, Patricio A, Rodríguez-Moreno A, Camacho-Abrego I, Limón ID, Flores G(2012) Dendritic Morphology Changes in Neurons from the Prefrontal Cortex, Hippocampus and Nucleus Accumbens in Rats after Lesion of the Thalamic Reticular Nucleus. *Neuroscience* **223**: 429–38.

Tosevski J, Malikovic A, Mojsilovic-Petrovic J, Lackovic V, Peulic M, Sazdanovic P, Alexopulos C (2002) Types of Neurons and Some Dendritic Patterns of Basolateral Amygdala in Humans--a Golgi Study. *Ann Anat* **184** (1): 93–103.

Truitt WA, Sajdyk TJ, Dietrich AD, Oberlin B, McDougle CJ, Shekhar A(2007) From Anxiety to Autism : Spectrum of Abnormal Social Behaviors Modeled by Progressive Disruption of Inhibitory Neuronal Function in the Basolateral Amygdala in Wistar Rats. *Psychopharmacology* (Berl) **191** (1): 107–118.

Tseng HA & Nadim F. (2010). The membrane potential waveform of bursting pacemaker neurons is a predictor of their preferred frequency and the network cycle frequency. *J Neurosci* **30,** 10809-10819.

Vacher H, Diochot S, Bougis PE, Martin-Eauclaire MF & Mourre C. (2006). Kv4 channels sensitive to BmTX3 in rat nervous system: autoradiographic analysis of their distribution during brain ontogenesis. *Eur J Neurosci* **24,** 1325-1340.

Van Bockstaele EJ, Garcia-Hernandez F, Fox K, Alvarez VA, Williams JT (2004). Expression of connexins during development and following manipulation of afferent input in the rat locus coeruleus. *Neurochem Int*. **45**(2-3):421-8.

Van Eden CG & Uylings HB. (1985). Postnatal volumetric development of the prefrontal cortex in the rat. *J Comp Neurol* **241,** 268-274.

Vargas G, Lucero MT (2002) Modulation by PKA of the Hyperpolarization-activated Current (Ih) in Cultured Rat Olfactory Receptor Neurons. *Journal of Membrane Biology* **188**: 115-125.

Vasilyev DV & Barish ME. (2002). Postnatal development of the hyperpolarization-activated excitatory current Ih in mouse hippocampal pyramidal neurons. *J Neurosci* **22,** 8992-9004.

Vidal L, Ruíz C, Villena A, Díaz F, Pérez de Vargas I(2004) Quantitative Age-related Changes in Dorsal Lateral Geniculate Nucleus Relay Neurons of the Rat. *Neurosci Res* **48** (4): 387–96.

Weiner RI, Ganong WF (1972). Norepinephrine concentration in the hypothalamus, amygdala, hippocampus, and cerebral cortex during postnatal development and vaginal opening. *Neuroendocrinology* **9**(2):65:71.

Wiedenmayer CP, Barr GA (2001) Developmental Changes in Responsivity to Threat Are Stimulus-specific in Rats. *Dev Psychobiol* **39** (1): 1–7.

Wills TJ, Cacucci F, Burgess N & O'Keefe J. (2010). Development of the hippocampal cognitive map in preweanling rats. *Science* **328,** 1573-1576.

Woodruff AR, Sah P (2007) Inhibition and synchronization of basal amygdala principal neuron spiking by parvalbumin-positive interneurons. *J Neurophysiol* **98**: 2956-2961.

Woodruff AR, Sah P (2007) Networks of parvalbumin-positive interneurons in the basolateral amygdala. *J Neurosci* **27**: 553-563.

Wu N, Hsiao CF & Chandler SH. (2001). Membrane resonance and subthreshold membrane oscillations in mesencephalic V neurons: participants in burst generation. *J Neurosci* **21,** 3729-3739.

Yajeya J, de la Fuente Juan A, Merchan MA, Riolobos AS, Heredia M, Criado JM(1997) Cholinergic Responses of Morphologically and Electrophysiologically Characterized Neurons of the Basolateral Complex in Rat Amygdala Slices. *Neuroscience* **78** (3): 731–43.

Young CK (2011) Behavioral significance of hippocampal theta oscillations: looking elsewhere to find the right answers. *J Neurophysiol* **106**: 497-499.

Zaccolo M, Pozzan T (2003) CAMP and Ca2+ interplay: a matter of oscillation patterns. *Trends Neurosci* **26**: 53-55.

Zhang JC, Lau PM, Bi GQ (2009) Gain in sensitivity and loss in temporal contrast of STDP by dopaminergic modulation at hippocampal synapses. *Proc Natl Acad Sci U S A* **106**: 13028-13033.

Zhang J, Muller JF, McDonald AJ (2013) Noradrenergic Innervation of Pyramidal Cells in the Rat Basolateral Amygdala*. Neuroscience* **228**: 395–408.

Zhang TY, Parent C, Weaver I & Meaney MJ. (2004). Maternal programming of individual differences in defensive responses in the rat. *Annals of the New York Academy of Sciences* **1032,** 85-103.

Zhang ZW (2004) Maturation of layer V pyramidal neurons in the rat prefrontal cortex: intrinsic properties and synaptic function. *J Neurophysiol* **91** (3): 1171-82.